

**ESTIMATING MECHANICAL PROPERTIES OF CELLULAR
SOLID MATERIALS FROM ADDITIVE MANUFACTURING
PROCESSES**

A Dissertation
Presented to
The Academic Faculty

by

Sang-in Park

In Partial Fulfillment of the Requirements for
the Degree of Doctor of Philosophy
in the Mechanical Engineering

Georgia Institute of Technology
December, 2016

COPYRIGHT 2016 BY SANG-IN PARK

**ESTIMATING MECHANICAL PROPERTIES OF CELLULAR
SOLID MATERIALS FROM ADDITIVE MANUFACTURING
PROCESSES**

Approved by:

Dr. David W. Rosen, Chair
School of Mechanical Engineering
Georgia Institute of Technology

Dr. Seung-Kyum Choi
School of Mechanical Engineering
Georgia Institute of Technology

Dr. Yan Wang
School of Mechanical Engineering
Georgia Institute of Technology

Dr. Massimo Ruzzene
School of Aerospace Engineering
Georgia Institute of Technology

Dr. Chad Duty
Department of Mechanical, Aerospace,
& Biomedical Engineering
University of Tennessee

Date Approved: August 26, 2016

Dedicated to my parents.

ACKNOWLEDGEMENTS

This work would not have been possible without great support and help. I am grateful to a number of people who have provide their support and help in my dissertation work.

Foremost, I would like to express deepest gratitude to my advisor, Dr. David W. Rosen, for advising and guiding me with brilliant insights, wise advices, and constructive suggestions. Without his understanding, patience and support, my dissertation would have been a frustrating and overwhelming pursuit.

I would like to thank my committee members, Dr. Seung-kyum Choi, Dr. Yan Wang, Dr. Massimo Ruzzene and Dr. Chad Duty for providing their insightful comments and great feedback. Their advice was very important and helpful for my research.

I also would like to thank my labmates, Chad Hume, Jane Kang, Namin Jung, Amit Jariwala, Wencho Zhou, Narumi Watanabe, Jonathan Holmes, Ying Zhang, Xiayun Zhao, Patric Chang, JT Hansen, and Jason Nguyen, for the stimulating discussions, for the sleepless nights we were working together before deadlines, and for all the fun we have had in the last five years.

I owe my family: my parents and sister immense gratitude for their unconditional love and support throughout my life. I would not have been able to complete this dissertation without their continuous love and encouragement.

Last but not the least, to my caring, loving, and supportive wife, Moonju Sung: my deepest gratitude. Your encouragement when the times got rough are much appreciated. It was a great comfort and relief to know that you were willing to provide management of our household activities while I completed my work. My heartfelt thanks.

Finally, I love you, Ethan.

TABLE OF CONTENTS

ACKNOWLEDGEMENTS	III
LIST OF TABLES	XI
LIST OF FIGURES	XII
LIST OF SYMBOLS AND ABBREVIATIONS	XVII
SUMMARY	XVIII
CHAPTER 1 INTRODUCTION.....	1
1.1 CELLULAR SOLID MATERIAL	1
1.1.1 Classification.....	2
1.1.2 Material Characteristics and Applications	4
1.2 FABRICATION OF CELLULAR SOLID MATERIAL.....	9
1.2.1 Conventional Manufacturing Techniques & Limitation.....	9
1.2.2 Additive Manufacturing Processes & Limitations.....	12
1.3 MECHANICAL PROPERTY ESTIMATION PROCEDURES FOR CELLULAR SOLID MATERIALS AND LIMITATION	15
1.4 RESEARCH OBJECTIVE	16
1.5 SCOPE OF THE RESEARCH.....	17
1.6 ORGANIZATION OF THESIS	18
CHAPTER 2 LITERATURE REVIEW & RESEARCH GAP	20
2.1 PROCESS PARAMETER CONTROL AND PROCESS MODELING.....	20
2.1.1 Material Extrusion Process	20

2.1.2	Powder Bed Fusion Process.....	23
2.2	EFFECTS OF FABRICATED GEOMETRIES IN CELLULAR MATERIAL	24
2.2.1	Geometrical Degradation	24
2.2.2	Integration of Geometrical Degradation	25
2.2.3	Effect of Joint Region	26
2.3	ESTIMATING MECHANICAL PROPERTIES OF CELLULAR MATERIAL.....	27
2.3.1	Analytic Approach	28
2.3.2	Numerical Approach.....	30
2.4	IDENTIFICATION OF RESEARCH GAPS.....	31
2.5	CHAPTER SUMMARY	32
CHAPTER 3 FORMULATION OF RESEARCH FRAMEWORK.....		33
3.1	PROPOSED RESEARCH FRAMEWORK	33
3.2	PARAMETER CLASSIFICATION.....	34
3.2.1	Design & Manufacturing Process Parameters	35
3.2.2	Layer Deposition Parameters	37
3.2.3	Structural Element Parameters.....	38
3.2.4	Cellular Material Properties	38
3.3	TRANSFORMATIONS	39
3.3.1	Transformation 1: DMP to LDP	40
3.3.2	Transformation 2: LDP to SEP	40
3.3.3	Transformation 3: SEP to CMP	41
3.4	RESEARCH QUESTIONS	41
3.5	CHAPTER SUMMARY	46

CHAPTER 4	DEPOSITION SHAPE MODELING	47
4.1	MATERIAL EXTRUSION PROCESS EQUATION CHAPTER 4 SECTION 1.....	47
4.1.1	Deposition Shape Image Generation Procedure	48
4.1.2	Calculating Deposition Path	49
4.1.3	Considering Manufacturing Instabilities.....	52
4.1.4	Generation of Deposition Shape Images.....	53
4.2	POWDER BED FUSION PROCESS	56
4.2.1	Powder Bed Modeling	57
4.2.2	Heat Transfer Analysis in Powder Bed.....	59
4.2.3	Considering Manufacturing Uncertainties	64
4.2.4	Generating Deposited Shape Image.....	64
4.3	IMPLEMENTATION	66
4.3.1	Area of Deposited Geometries.....	66
4.3.2	Dimensions of Deposition Geometries	68
4.3.3	Effects of Resolution.....	70
4.4	CHAPTER SUMMARY	72
CHAPTER 5	AS-FABRICATED VOXEL MODEL	73
5.1	VOXEL-BASED MODELING OF DEPOSITED SHAPE	73
5.1.1	Material Extrusion	74
5.1.2	Powder Bed Fusion Process.....	78
5.2	EFFECT OF VOXEL RESOLUTION	80
5.3	VALIDATION OF THE AS-FABRICATED VOXEL MODEL.....	82
5.3.1	Implementation of As-fabricated Voxel Modeling Approach.....	82

5.3.2	Numerical Analysis using As-fabricated Voxel Models	85
5.3.3	Experimental Result.....	86
5.3.4	Quantification of AM Process Effect.....	89
5.4	CHAPTER SUMMARY	96
CHAPTER 6 DETERMINATION OF STRUCTURAL ELEMENT		
PARAMETERS..... 98		
6.1	STRUCTURAL ELEMENT PARAMETERS	98
6.2	DERIVATION OF SEMI-RIGID JOINT FRAME ELEMENT	100
6.3	EFFECTIVE STRUCTURAL ELEMENT PARAMETERS	108
6.3.1	Fabricated Density	110
6.3.2	Effective Strut Diameter, Eccentricity and Fixity.....	110
6.4	AM PROCESS EFFECTS ON STRUCTURAL ELEMENT PARAMETERS	115
6.4.1	Material Extrusion	116
6.4.2	Powder Bed Fusion Process.....	127
6.5	CHAPTER SUMMARY	131
CHAPTER 7 PROPERTY ESTIMATION PROCEDURE FOR CELLULAR		
MATERIAL 132		
7.1	DISCRETE HOMOGENIZATION APPROACH	132
7.2	DERIVATION OF HOMOGENIZED MECHANICAL PROPERTIES	137
7.2.1	Homogenized Elastic Modulus and Poisson's Ratio	137
7.2.2	Homogenized Yield Strength.....	145
7.3	EFFECTS OF STRUCTURAL ELEMENT PARAMETERS ON HOMOGENIZED	
	PROPERTIES	149

7.3.1	Elastic modulus	149
7.3.2	Yield Strength	152
7.4	VALIDATION OF HOMOGENIZED PROPERTIES.....	154
7.4.1	Material Extrusion Process	154
7.4.2	Powder Bed Fusion process	164
7.5	CHAPTER SUMMARY	167
CHAPTER 8 CLOSURE AND CONTRIBUTION.....		170
8.1	SUMMARY OF DISSERTATION.....	170
8.2	REVISITING RESEARCH QUESTIONS	172
8.2.1	Research Question 1	172
8.2.2	Research Question 2	173
8.2.3	Research Question 3	175
8.3	CONTRIBUTIONS	176
8.4	RECOMMENDATION FOR FUTURE WORK.....	178
8.5	LESSONS LEARNED	179
APPENDIX A THREE-DIMENSIONAL SHEAR DEFORMABLE SEMI-RIGID JOINT BEAM		187
A.1	SHAPE FUNCTIONS	187
A.2	STIFFNESS MATRIX	189
APPENDIX B BLOCK MATRICES FOR SELECTED UNIT CELLS		190
B.1	CUBIC UNIT CELL.....	190
B.2	DIAMOND UNIT CELL.....	191

B.3 DODECAHEDRON UNIT CELL.....	192
B.4 BODY CENTER CUBIC UNIT CELL.....	193
B.5 OCTET-TRUSS UNIT CELL	194
REFERENCES.....	195
VITA.....	202

LIST OF TABLES

Table 1-1 Material characteristics of cellular materials.....	5
Table 1-2 Classification of AM processes [10]	13
Table 2-1 FDM FDC and FDMet process variables [11]	21
Table 3-1 Selected manufacturing process parameters.....	36
Table 5-1 Mechanical properties from reference models	86
Table 5-2 Property degradation from test	88
Table 5-3 Volume difference between Models 1 and 2 for Designs 2 and 3.....	91
Table 6-1 Structural element parameters	99
Table 6-2 Effective structural element parameters of the joint models	117
Table 6-3 Comparison of fabricated density.....	125
Table 7-1 Selected structural parameters	149
Table 7-2 Specification of cubic type unit cell specimens	155
Table 7-3 Specification of diamond type unit cell specimens	159
Table 7-4 Mean value of obtained mechanical properties from tensile test	159
Table 7-5 Comparison between test result and estimates	167

LIST OF FIGURES

Figure 1-1 Stochastic cellular materials [4, 5]	3
Figure 1-2 Periodic cellular materials	4
Figure 1-3 Material property chart: Structural properties	6
Figure 1-4 Typical compressive stress-strain curve of foams	7
Figure 1-5 Concept for structural application of cellular materials [7]	7
Figure 1-6 Material property chart: Thermal properties	8
Figure 1-7 Application of cellular material according to porosity [7]	9
Figure 1-8 Schematic illustration of manufacturing process for a foam [5]	10
Figure 1-9 Conventional manufacturing methods for periodic cellular materials	11
Figure 1-10 Additively manufactured periodic cellular material	13
Figure 1-11 Source of geometric degradation	14
Figure 1-12 Internal defects in additive manufacturing process	15
Figure 3-1 Overall Problem Formulation	34
Figure 3-2 Classification of parameters	35
Figure 3-3 Deposition shape images	37
Figure 3-4 Propagation of manufacturing instability through transformations	39
Figure 4-1 Schematic illustration of material extrusion process	48
Figure 4-2 Deposition shape generation procedure	48
Figure 4-3 Slicing procedure	50
Figure 4-4 Toolpath and deposition image generation	51
Figure 4-5 Validation of deposition path generation procedure	52
Figure 4-6 Deposition shape image generation	54

Figure 4-7 Comparison between greyscale and binary image	55
Figure 4-8 Shape comparison for ME process.....	55
Figure 4-9 Powder morphology and particle size distribution [12].....	58
Figure 4-10 Particle packing procedure using the rain model	58
Figure 4-11 Powder bed model.....	59
Figure 4-12 Physical phenomena during power bed fusion process [35].....	60
Figure 4-13 Powder bed model.....	61
Figure 4-14 Beam energy profile	61
Figure 4-15 Result for heat transfer analysis	63
Figure 4-16 Scanning path analysis for small feature size with 0.1 mm beam spot [85] .	65
Figure 4-17 Shape comparison for PBF process.....	66
Figure 4-18 Distribution of the area for the ME process	67
Figure 4-19 Distribution of the area for the PBF process.....	68
Figure 4-20 Calculation of Dimension	68
Figure 4-21 Distribution of geometrical dimension for the ME process	69
Figure 4-22 Distribution of geometrical dimension for the PBF process.....	69
Figure 4-23 Deposition shape images for material extrusion process	70
Figure 4-24 Deposition shape images for EBM process	71
Figure 4-25 Effect of resolution on area.....	71
Figure 4-26 Effect of resolution on strut diameter.....	71
Figure 4-27 Effect of resolution on positional error of center location	72
Figure 5-1 As-fabricated voxel model generation procedure	74
Figure 5-2 Voxel model generation for material extrusion process	74

Figure 5-3 Cross sections in the literature	75
Figure 5-4 Cross section of deposited filaments.....	75
Figure 5-5 Assumption for filament cross section.....	76
Figure 5-6 Deposition shape image for voxel layers	76
Figure 5-7 Comparison of a fabricated strut and its as-fabricated voxel model using ME	78
Figure 5-8 Layer deposition images at each layer	79
Figure 5-9 As-fabricated voxel model of three deposition layers using PBF process.....	79
Figure 5-10 Comparison of a fabricated strut and its as-fabricated voxel model using SLM	80
Figure 5-11 Change in the number of DOFs according to voxel resolution.....	81
Figure 5-12 Change in volume and estimated stiffness according to voxel resolution	82
Figure 5-13 Specimen designs	83
Figure 5-14 Build angles.....	83
Figure 5-15 Resulting as-fabricated voxel models for specimens	84
Figure 5-16 Modified as-fabricated model	84
Figure 5-17 Reference models for calculating mechanical properties.....	86
Figure 5-18 Fabricated specimens on the build plate	87
Figure 5-19 Comparison of normalized mechanical properties from tensile tests	88
Figure 5-20 Comparison: Elastic modulus	90
Figure 5-21 Change of stair steps according to build angle.....	92
Figure 5-22 Comparison: Ultimate tensile strength.....	94
Figure 5-23 Fracture section of Design 1 specimens at each build angle.....	95

Figure 5-24 Deposition path for lattice region in Design 2 specimen at 75° build angle .	95
Figure 6-1 Two regions of a strut in a lattice structure.....	99
Figure 6-2 Semi-rigid joint frame element	101
Figure 6-3 Conceptual deformed configuration of semi-rigid joint frame	102
Figure 6-4 Structural element parameter determination procedure	109
Figure 6-5 Boundary conditions	112
Figure 6-6 Typical resulting displacement fields.....	112
Figure 6-7 Joint models	116
Figure 6-8 Pattern of deposition paths	117
Figure 6-9 Inclined angle and raster direction angle	119
Figure 6-10 Change in fabricated density.....	119
Figure 6-11 Structural element parameters as varying the build angle	121
Figure 6-12 Structural element parameters as varying the raster angle.....	122
Figure 6-13 Deposition path near joint	123
Figure 6-14 Degradation of structural parameters due to manufacturing uncertainty....	126
Figure 6-15 As-fabricated voxel models based on each distribution.....	127
Figure 6-16 Histogram for effective strut diameter	128
Figure 6-17 Probabilistic density functions of effective strut diameters	128
Figure 6-18 Effective strut diameter with varying build angle.....	129
Figure 6-19 Change in radius due to AM process	129
Figure 6-20 Structural element parameters with varying build angles	130
Figure 7-1 Homogenization approach[92].....	133
Figure 7-2 Definition of representative unit cell.....	135

Figure 7-3 Example of unit cell definition.....	136
Figure 7-4 Overview of discrete homogenization method for elastic constitutive matrix	136
Figure 7-5 Overall procedure for homogenized yield strength.....	145
Figure 7-6 Elemental coordinates in a strut	147
Figure 7-7 Elastic moduli of cubic unit cell.....	151
Figure 7-8 Elastic moduli of diamond unit cell	151
Figure 7-9 Change in elastic modulus for octet-truss lattice	151
Figure 7-10 Yield strength of cubic unit cell	153
Figure 7-11 Yield strength of diamond unit cell.....	153
Figure 7-12 Yield strength of the octet-truss unit cell	153
Figure 7-13 Maximum von Mises stress in struts.....	154
Figure 7-14 Design of specimens	155
Figure 7-15 Comparison of elastic moduli in cubic unit cell.....	157
Figure 7-16 Comparison of yield strength in cubic unit cell	157
Figure 7-17 Comparison of elastic moduli in diamond and dodecahedron unit cell	159
Figure 7-18 Comparison of yield strength in diamond and dodecahedron unit cell.....	160
Figure 7-19 Design of 1D lattice specimens.....	162
Figure 7-20 Normalized elastic modulus with varying build angle.....	163
Figure 7-21 Normalized yield strength with varying angle	164
Figure 7-22 specimens for PBF process	165
Figure 7-23 Result of compression test	165

LIST OF SYMBOLS AND ABBREVIATIONS

AM	Additive manufacturing
DMP	Design and Manufacturing Process parameter
LDP	Layer Deposition Parameter
SEP	Structural Element Parameter
CMP	Cellular Material Properties

SUMMARY

Cellular materials have been used for engineering applications due to their favorable mechanical characteristics. However, conventional subtractive manufacturing processes are not suitable for cellular materials because of their complex geometries. Recently, additive manufacturing (AM) processes have begun to offer new opportunities to produce cellular materials. Layer-by-layer stacking process allows users to fabricate complex geometries with no additional effort. Although the AM technique can be a good solution for manufacturing issues, the mechanical properties of additively fabricated cellular materials cannot be guaranteed due to the inherent limitations of the AM process. This research aims to develop a mechanical property-estimation procedure for additively manufactured cellular materials by considering the effects of AM processes. In order to clearly understand the AM process, related parameters are categorized into four groups: (a) Design and Manufacturing process parameters (DMP), (b) Layer deposition parameters (LDP), (c) Structural element parameters (SEP), and (d) Cellular material properties (CMP). Three transformations are defined among these groups. Firstly, the functional relationship between DMPs and LDPs is established based on process-modeling simulation. The variation in LDPs due to manufacturing instabilities is quantified in the form of a stochastic distribution. Next, an as-fabricated voxel modeling approach is developed for describing the propagation of geometrical degradation from LDPs to SEPs. The effective values of SEPs are determined based on semi-rigid joint frame element formulation. Finally, a discrete homogenization approach is implemented with the semi-rigid elements to integrate the effects of AM processes into the mechanical

property estimation procedure. The estimation framework developed in this research can be applied to analyze the performance of additively manufactured cellular materials and help to design of cellular materials.

CHAPTER 1 INTRODUCTION

This research proposes and develops a method to quantify mechanical properties for additively manufactured cellular materials. The primary motivation for this research is to elaborate the property-estimation procedure by considering characteristics of the additive manufacturing processes. This chapter introduces cellular materials and additive manufacturing techniques and gives background towards developing the estimation procedure. A detailed explanation for the research objective is also presented.

1.1 Cellular Solid Material

Cellular solid materials are engineering materials that contain many cells dispersed throughout the material. Cellular materials originated in nature. Nature has been evolving her material efficiency to survive using limited resources over time. She harmonizes dense and light materials to maintain her functions and to support her structure. For example, natural cellular materials, such as wood and bone, have high elastic modulus and failure strength at relatively low density. The basic concept of implementing cellular material is that material is placed where it is needed.

Humans have adopted and imitated cellular materials for the same reason as nature does to meet the needs of civilization. Cellular solid materials have been applied to various engineering applications, such as large building structures like bridges and towers, automotive and aerospace parts, and bio-medical implants. Cellular materials are classified into two groups: stochastic (irregular) and periodic (regular) cellular materials. Natural cellular solid materials are typically irregular, and man-made cellular material in the early stages, such as foam, was also irregular. Compared to regular solid materials, irregular cellular solids have an advantage in that the manufacturing procedure is

relatively uncomplicated. However, recent research shows that periodic cellular materials, such as lattice structures, can achieve better mechanical properties than stochastic cellular materials, since the material distribution can be controlled and optimized under given constraints [1-3]. This section presents a detailed explanation of the classification and characteristics of cellular materials and their applications.

1.1.1 Classification

Cellular solid materials are typically made up of a network of geometrical features such as struts and plates. They are classified into two groups based on the arrangement of their geometrical features: stochastic and periodic cellular solid materials.

1.1.1.1 Stochastic Cellular Materials

Geometric structures in stochastic cellular materials are randomly arranged. This kind of material typically has a representative unit cell that is a fundamental shape to construct their structure. The geometrical dimensions of each cell are not the same through a whole structure, but their topology remains similar. Most natural cellular materials, such as bone, cork and plant stalks, are categorized to this class. For man-made artificial stochastic cellular materials, a foam material is representative. Figure 1-1 (a) and (b) show stochastic cellular materials found in nature, and Figure 1-1 (c), (d) and (e) present artificial materials.

As seen in Figure 1-1, geometrical details, such as the sizes of cells and struts, are not explicitly defined. Thus, the characteristics of stochastic cellular materials are defined statistically or experimentally. The most important parameter for describing material characteristics is the relative density, presented in the following:

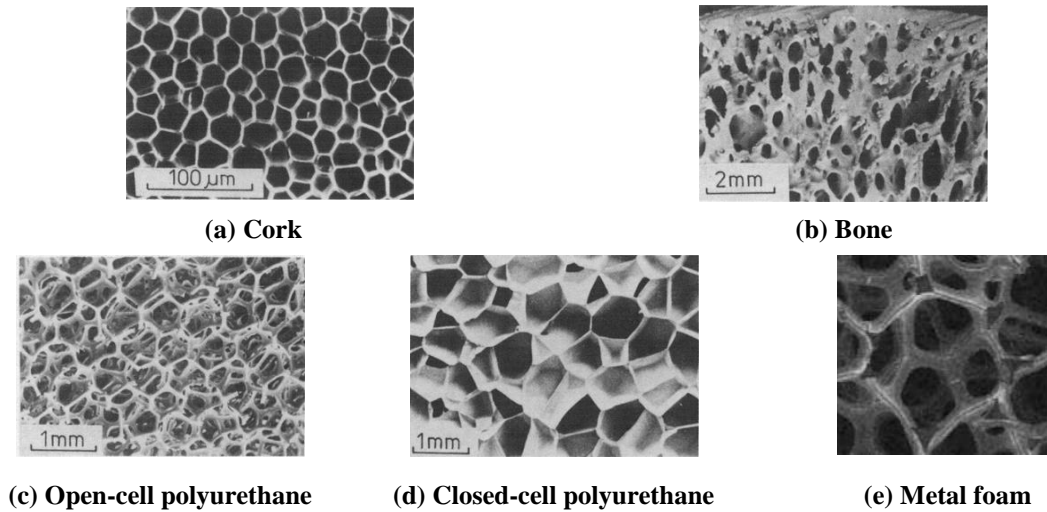


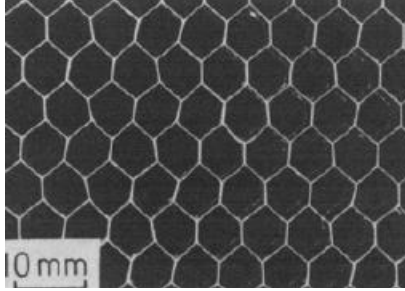
Figure 1-1 Stochastic cellular materials [4, 5]

$$\rho = \frac{\rho^*}{\rho_0} \tag{1.1}$$

where, ρ^* and ρ_0 are foam density and solid material density, respectively. Mechanical characteristics, such as elastic modulus and strength, are defined based on relative density, due to indefinite geometrical information.

1.1.1.2 Periodic Cellular Materials

Periodic cellular materials are obtained by repeatedly arranging a representative unit cell. Figure 1-2 shows periodic cellular materials. A honeycomb is a natural-oriented periodic cellular material, which has a hexagonal representative unit cell.



(a) Honeycomb structure



(b) Lattice structure

Figure 1-2 Periodic cellular materials

Periodic cellular materials have advantages over the stochastic cellular materials. Firstly, the properties of periodic cellular materials can be reproduced, while stochastic cellular materials cannot be replicated due to geometrical randomness. Secondly, since periodic cellular materials are constructed based on a definite representative unit cell, their mechanical and geometrical characteristics mainly depend on their representative unit cells. Therefore, the properties can be estimated by analyzing the representative unit cell, and they can be designed based on the representative unit cell. Generally, periodic cellular materials have better mechanical properties, since the shape and dimension of their representative unit cells can be designed and optimized for target applications.

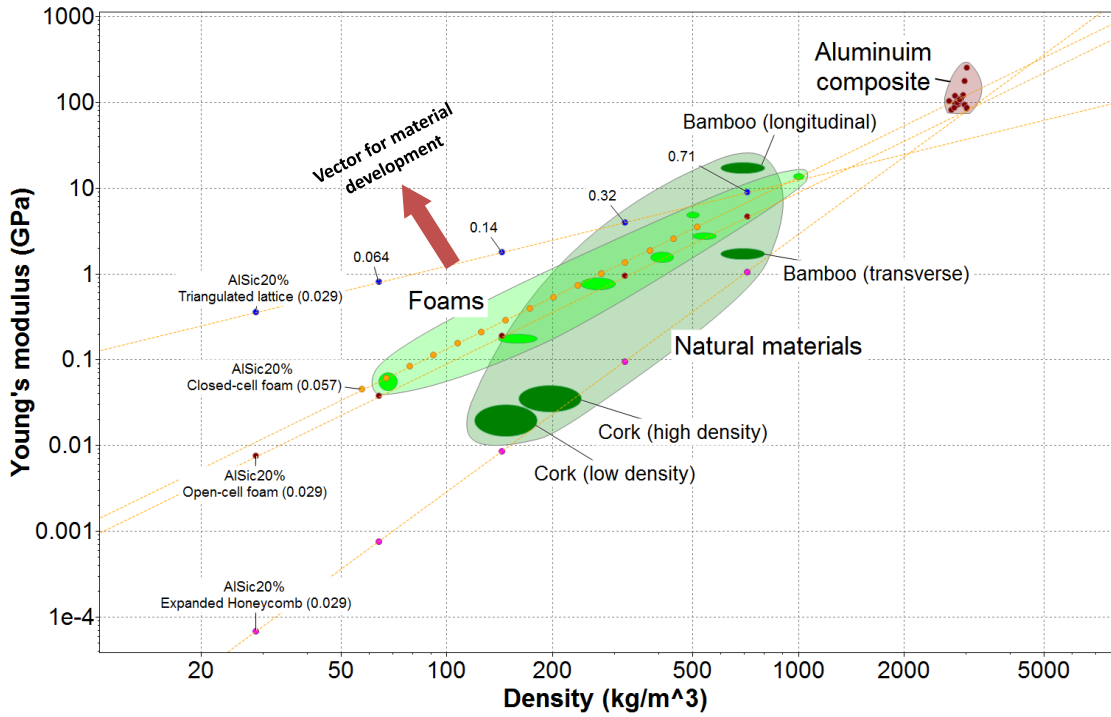
1.1.2 Material Characteristics and Applications

Cellular solid materials have favorable characteristics over bulk materials. Their unique characteristics increase structural, thermal, and morphological applications. The representative material characteristics are summarized in Table 1-1.

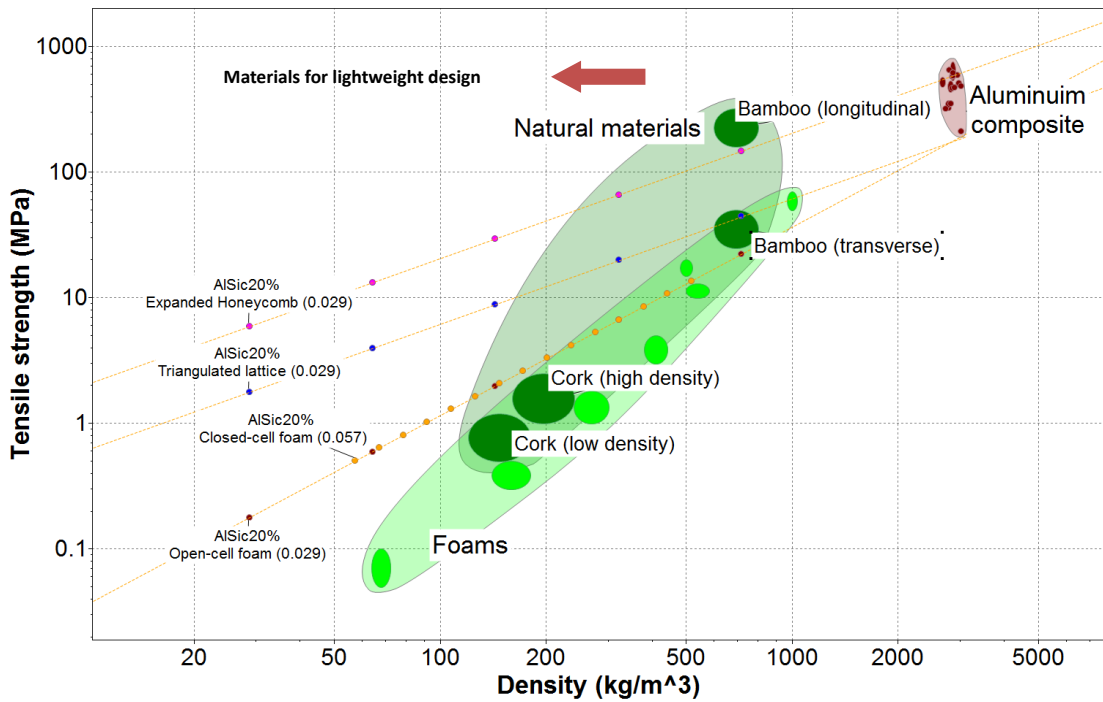
Table 1-1 Material characteristics of cellular materials

Structure	<ul style="list-style-type: none">• High strength to weight ratio• High energy absorption• Sound and vibration absorption
Thermal	<ul style="list-style-type: none">• Tailorable thermal coefficients
Morphology	<ul style="list-style-type: none">• Flexibility in porosity design

Cellular materials can increase material utilization [6]. The materials can fill regions where current bulk materials cannot, as shown in Figure 1-3. Their high strength to weight ratio enables a lightweight design that has significant impact in the automotive and aerospace industries. In addition, cellular materials can absorb high energy during their collapse, as shown in Figure 1-4, since the complex geometry in cellular materials leads to localized failure that prevents sudden fracture and densification. Furthermore, their high stiffness and low weight yield high natural frequencies, and this makes them hard to excite.



(a) Young's modulus vs. Density



(b) Strength vs. Density

Figure 1-3 Material property chart: Structural properties

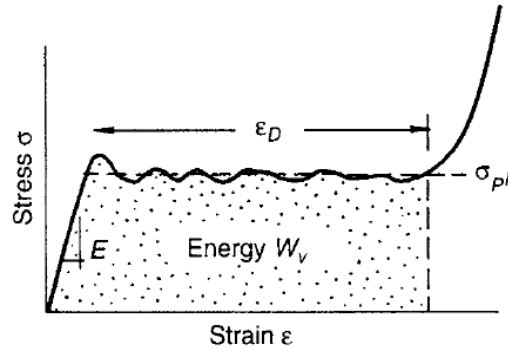


Figure 1-4 Typical compressive stress-strain curve of foams

Their structural applications are found in various engineering fields, such as automotive, aerospace, railway, building and biomedical industries. The main applications are lightweight construction, energy absorption and damping insulation as shown in Figure 1-5.

Next, cellular materials have a larger range of thermal properties, as shown in Figure 1-6. This increases their feasible design range for thermal applications. Thermal conductivity can be improved using periodic cellular materials, such as honeycombs, and low thermal conductivity can be achieved using foams.

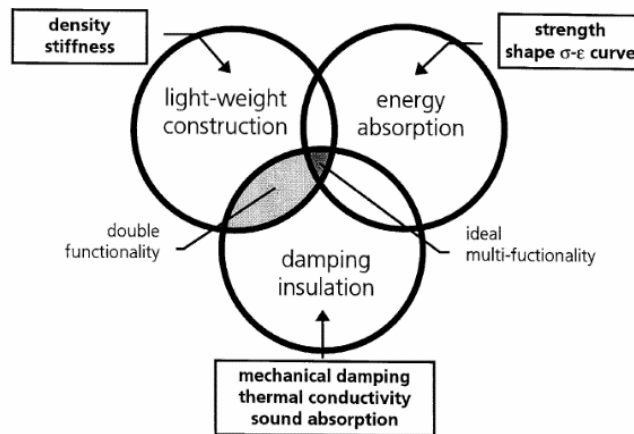


Figure 1-5 Concept for structural application of cellular materials [7]

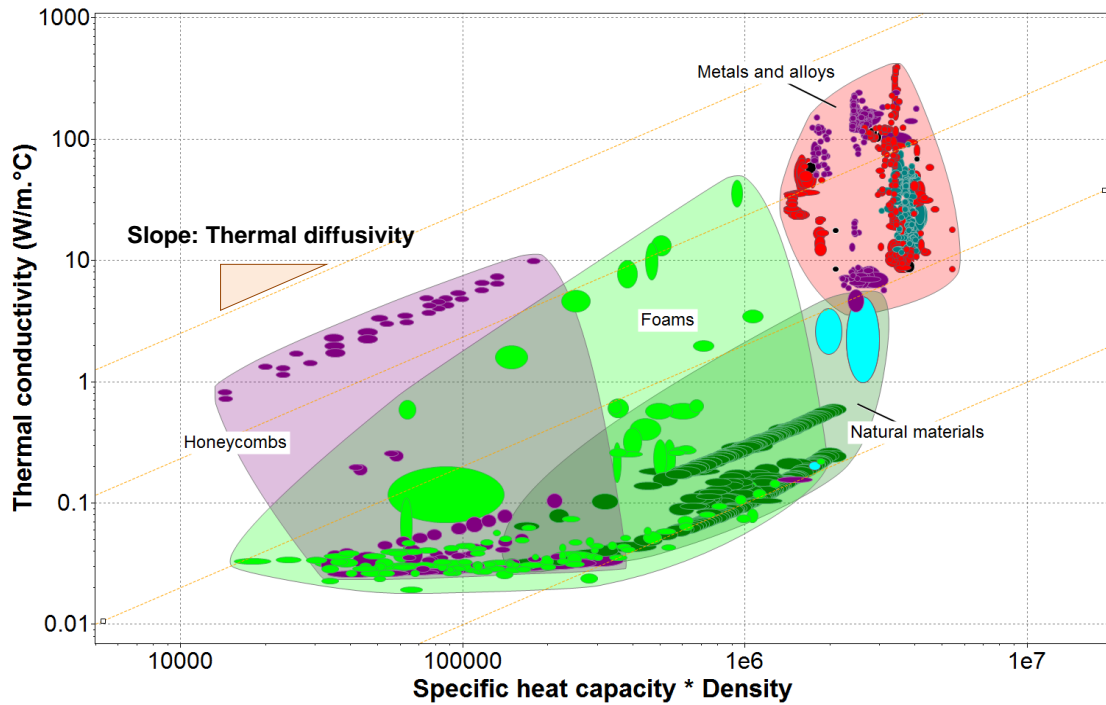


Figure 1-6 Material property chart: Thermal properties

Lastly, cellular materials, especially periodic cellular materials, can provide flexibility in designing porosity in the design. This characteristic allows cellular materials to implement functional applications where their functions, rather than mechanical characteristics, are emphasized, such as heat exchangers, filters, catalyst supports. Figure 1-7 shows various applications of cellular materials based on their porosity.

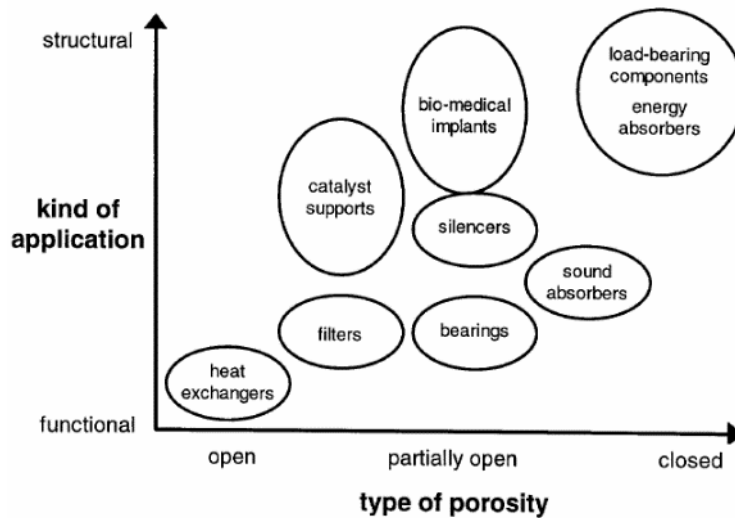


Figure 1-7 Application of cellular material according to porosity [7]

1.2 Fabrication of Cellular Solid Material

Fabricating cellular materials is a cost-intensive task due to their geometric complexity. Complex geometries impede implementation of currently well-developed manufacturing techniques, which are based on subtraction and deformation of a raw material. Recently, additive manufacturing (AM) technology has emerged as an alternative process for producing cellular materials, since it can be used to fabricate complex parts without additional manufacturing cost and time. This section explains fabrication methods for cellular materials, as well as their limitations.

1.2.1 Conventional Manufacturing Techniques & Limitation

For the past three decades diverse manufacturing techniques for cellular solid materials have been developed, based on conventional manufacturing processes. For stochastic cellular material, the manufacturing methods mainly utilize gas injection or investment casting techniques as shown in Figure 1-8 [5]. Gas injection is mainly used to

fabricate closed-cell foams, and investment casting is used to produce open-cell foams. Since these fabrication methods are uncontrollable, the geometries of stochastic cellular materials totally depend not an engineer's design but on manufacturing process parameters. Thus, mechanical properties cannot be defined accurately.

Fabricating periodic cellular materials requires a complex combination of conventional manufacturing processes, such as extruding, pressing, wiring, and welding, since geometrical features in the material are explicitly defined in their design. Figure 1-9 shows conventional manufacturing methods for periodic cellular materials.

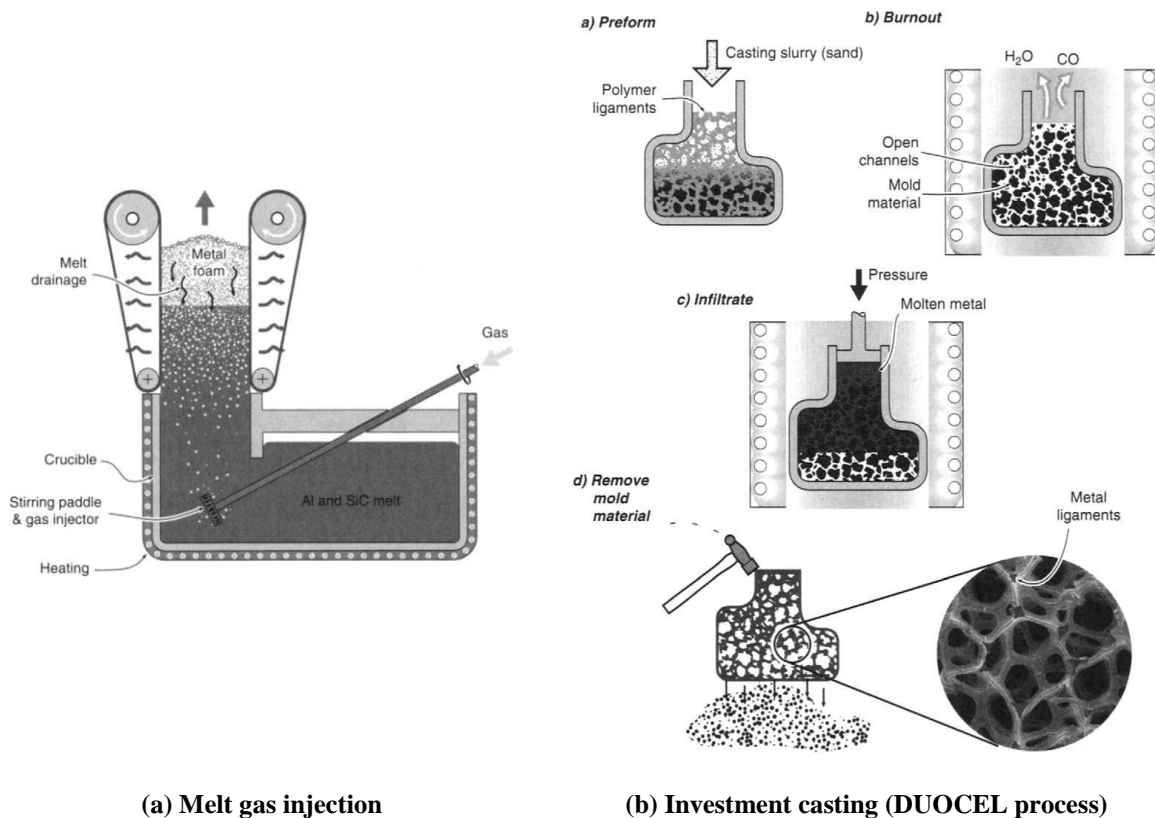
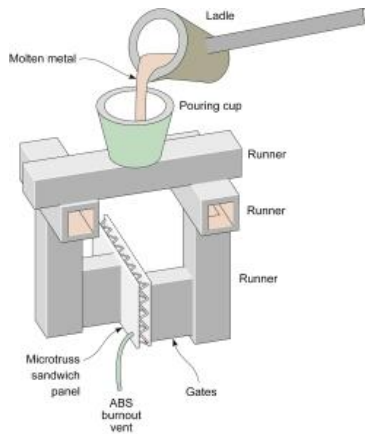
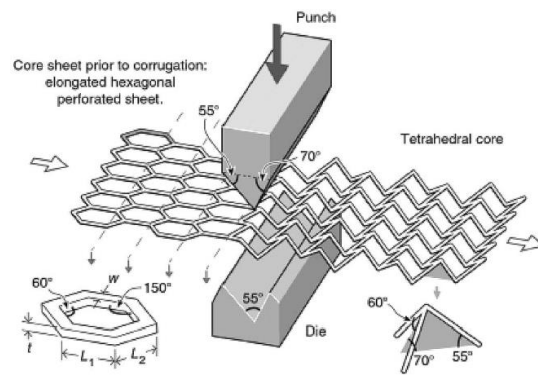


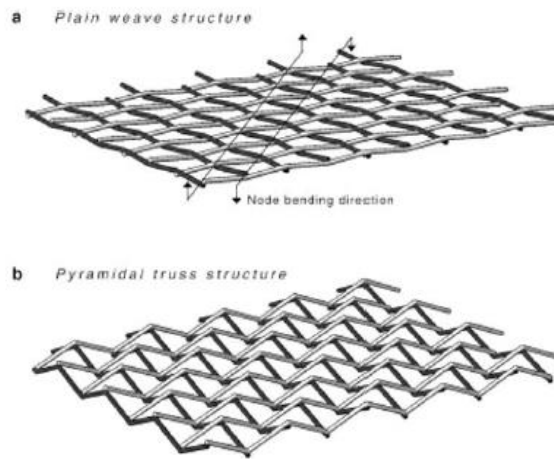
Figure 1-8 Schematic illustration of manufacturing process for a foam [5]



(a) Investment casting process [8]



(b) Deformation forming process [9]



(c) Metal wiring [9]

Figure 1-9 Conventional manufacturing methods for periodic cellular materials

Creating complex geometries from repeated patterns increases the possibility that manufacturing toolpaths will cause collisions between the tool and workpiece. Moreover, thin features, such as thin struts and walls, lead to manufacturing difficulties. Furthermore, complex procedures increase manufacturing cost and time. For complex cellular materials, it is impossible to implement conventional manufacturing procedures due to lack of tool top space.

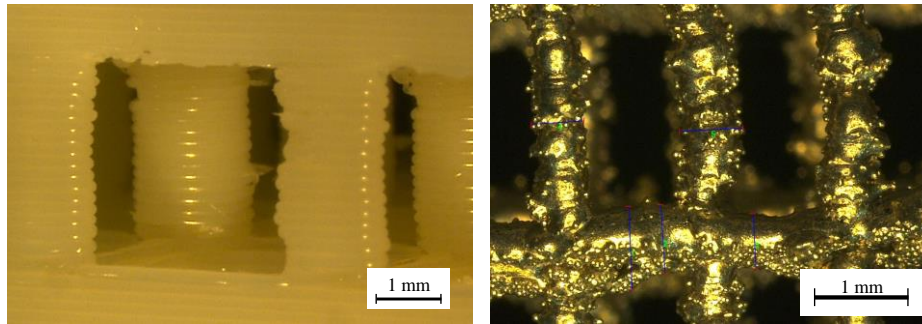
1.2.2 Additive Manufacturing Processes & Limitations

An additive manufacturing technique is a manufacturing method to construct a three-dimensional part based on its two-dimensional information. The fundamental concept of an AM process is to repeatedly deposit layers, which are cut, placed or melted along desired material boundaries. This process requires no space for tools, and it can produce parts without special preparation and without long setup time. This reduces complexities, such as wiring, pressing and welding, found in conventional manufacturing processes. Thus, the AM process simplifies a manufacturing procedure regardless of the geometrical complexity of a part. Seven types of AM processes based on deposition methods are listed in Table 1-2.

AM processes have been implemented for fabricating periodic cellular materials by virtue of their geometric complexity free procedure. Figure 1-10 shows polymer and metal lattice structure using a material extrusion and powder bed fusion processes. Although AM processes make it possible to fabricate cellular materials, two dimensional approximation during a slicing process incurs geometrical inaccuracy in fabricated cellular materials, as shown in Figure 1-10, and inaccurate geometries lead to property degradation.

Table 1-2 Classification of AM processes [10]

CATEGORIES	TECHNOLOGIES	PRINTED "INK"	POWER SOURCE	STRENGTHS / DOWNSIDES
Material Extrusion	Fused Deposition Modeling (FDM)	Thermoplastics, Ceramic slurries, Metal pastes	Thermal Energy	<ul style="list-style-type: none"> • Inexpensive extrusion machine • Multi-material printing • Limited part resolution • Poor surface finish
	Contour Crafting			
Powder Bed Fusion	Selective Laser Sintering (SLS)	Polyamides /Polymer	High-powered Laser Beam	<ul style="list-style-type: none"> • High Accuracy and Details • Fully dense parts • High specific strength & stiffness • Powder handling & recycling • Support and anchor structure • Fully dense parts • High specific strength and stiffness
	Direct Metal Laser Sintering (DMLS)	Atomized metal powder (17-4 PH stainless steel, cobalt chromium, titanium Ti6Al-4V), ceramic powder		
	Selective Laser Melting (SLM)			
	Electron Beam Melting (EBM)		Electron Beam	
Vat Photopolymerization	Stereolithography (SLA)	Photopolymer, Ceramics (alumina, zirconia, PZT)	Ultraviolet Laser	<ul style="list-style-type: none"> • High building speed • Good part resolution • Overcuring, scanned line shape • High cost for supplies and materials
Material Jetting	Polyjet / Inkjet Printing	Photopolymer, Wax	Thermal Energy / Photocuring	<ul style="list-style-type: none"> • Multi-material printing • High surface finish • Low-strength material
Binder Jetting	Indirect Inkjet Printing (Binder 3DP)	Polymer Powder (Plaster, Resin), Ceramic powder, Metal powder	Thermal Energy	<ul style="list-style-type: none"> • Full-color objects printing • Require infiltration during post-processing • Wide material selection • High porosities on finished parts
Sheet Lamination	Laminated Object Manufacturing (LOM)	Plastic Film, Metallic Sheet, Ceramic Tape	Laser Beam	<ul style="list-style-type: none"> • High surface finish • Low material, machine, process cost • Decubing issues
Directed Energy Deposition	Laser Engineered Net Shaping (LENS) Electronic Beam Welding (EBW)	Molten metal powder	Laser Beam	<ul style="list-style-type: none"> • Repair of damaged / worn parts • Functionally graded material printing • Require post-processing machine



(a) FDM process

(b) EBM process

Figure 1-10 Additively manufactured periodic cellular material

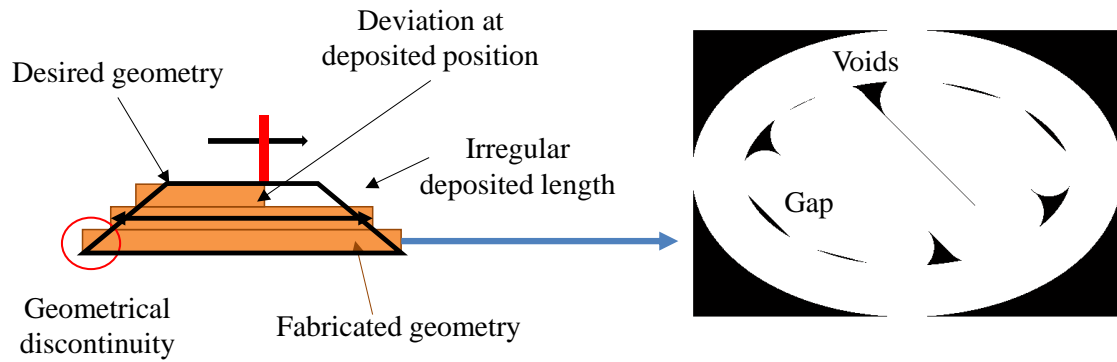
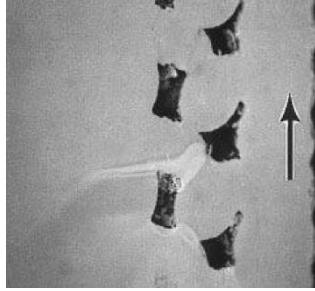
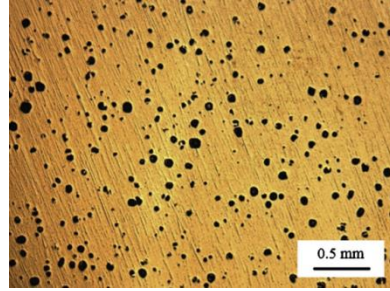


Figure 1-11 Source of geometric degradation

There are two main sources of geometric degradation. First, geometrical discontinuity, called a stair step, occurs among layers due to slicing that approximates three-dimensional part geometries using two-dimensional layers as shown in Figure 1-11. This is an inherent defect in all types of AM processes. Since the number of stair steps is not negligible compared to the dimensions of the cellular materials, they have large impacts on the mechanical properties of these materials. Second, internal defects such as voids and gaps are generated while fabricating cellular material using an AM process. Figure 1-12 shows internal voids and gaps in material extrusion and powder bed fusion processes. Generally, the dimensions of the structural elements in cellular materials such as struts and walls are not large enough to neglect internal defects. Thus, manufacturing process parameters related to the defects influence the mechanical properties of cellular materials.



(a) Voids in material extrusion [11]



(b) Voids in powder bed fusion process [12]

Figure 1-12 Internal defects in additive manufacturing process

1.3 Mechanical Property Estimation Procedures for Cellular Solid Materials and Limitation

A homogenization technique is a mathematical approach to estimate the macroscale effective mechanical properties of a heterogeneous media that consists of repeatedly arranged representative unit cells. The main assumptions in the homogenization approach are that a dimension of the representative unit is sufficiently small to neglect local deviation of physical quantities and that the unit cell is repeated infinitely. This approach has been implemented in various engineering problems such as determining the mechanical properties of composite materials and investigating the effects of microstructures on material characteristics.

The homogenization technique is a popular mechanical property estimation method for cellular materials, since cellular materials consist of periodically or stochastically arranged representative unit cells. Various homogenization approaches have been developed for cellular material applications. However, most research has focused on investigating a mathematical relationship between the geometrical topology of the representative unit cell in periodic cellular materials and the resulting mechanical

properties. Since there is no consideration for manufacturing effects in conventional homogenization approaches, estimates for additively manufactured cellular materials are overestimated or underestimated depending on manufacturing conditions. Thus, the approaches need to be modified or reformulated in order for additively manufactured cellular materials to be implemented.

1.4 Research Objective

This research focuses on the effects of the AM process on fundamental structural elements that constitute a cellular material and on the way the effects are propagated to the mechanical properties of a lattice structure. The research objective is abstracted as follows:

To develop an estimation method for mechanical properties of a lattice structure, in which the effects of the AM process are integrated

To achieve the goal, all related manufacturing, material, and geometrical parameters were identified and classified into four sets based on their characteristic length scale. Next, three transformations among the parameter sets were defined. Three research questions were made and answered to establish qualitative and quantitative relationships among the groups of parameters. The relationships were formulated as mathematical transformations.

1.5 Scope of the Research

This research focuses on additively manufactured periodic cellular materials, especially, lattice structures, which can substitute for current materials in various engineering applications where weight reduction and mechanical property customization are required.

Although the AM process enables fabrication of these cellular materials, designers and engineers encounter difficulties in applying cellular materials for two reasons: the scale of the design problem and inaccuracy. Conventional analysis methods, such as finite element analysis (FEA), are not suitable for cellular materials that include a huge number of repeated unit cells, since the required computing resource rapidly increases as the number of unit cells increases. Moreover, mechanical properties, such as elastic modulus and yield strength, obtained from existing property evaluation procedures are not accurate. The procedures assume that the fabricated geometries are perfect. However, this is not a realistic assumption, since AM processes inherently induce geometrical and material degradation. Thus, this research seeks to relieve the scaling problem and improve the accuracy of the estimation procedure for additively manufactured periodic cellular materials in order to help to design lightweight and property customized applications.

This work addresses two issues. The first is how to assess and quantify the AM process effects, and the second is how to integrate them with the estimation procedure for periodically arranged cellular materials. To investigate the first issue, we defined groups of parameters based on observation of the AM processes, we fabricated cellular materials, and we inspected the interactions among these groups. In more detail, this study includes

capturing uncertainties that occur in the parameter groups during the steps of the AM processes and describing how the AM processes propagate these uncertainties among the groups in order to evaluate the AM process effects.

To examine the second issue, this research employed the discrete homogenization approach, which finds mechanical properties, such as elastic modulus and yield strength, used for substituting the periodic cellular materials with solid materials. The homogenization approach relieved difficulties from geometrical complexity and provided structural parameters for degraded geometries. The assessed AM process effects were incorporated into the discrete homogenization approach in order to develop the estimation procedure.

Two types of the AM processes, material extrusion and powder bed fusion, were the focus of this research. Testing specimens were fabricated using these two processes and then were used for validation purposes.

1.6 Organization of Thesis

This dissertation consists of three parts. The first introduces background and problem formulation. A brief introduction to the cellular material and property estimation procedure is presented in Chapter 1. The research objective is introduced in Chapter 1.4. Chapter 2 provides detailed review of related previous research in order to identify the research gap. In Chapter 3, the proposed research framework is presented. Various parameters involved in this research are introduced and classified, and three transformations are explained among parameter groups to formulate the framework. Research questions are presented in Chapter 3.4.

The second part presents the proposed research framework and validation. Chapter 4 describes deposition shape modeling schemes for material extrusion and powder bed fusion processes. In Chapter 5, an as-fabricated voxel modeling approach is presented, and parametric studies are performed in order to investigate the effect of manufacturing parameters on the fabricated geometry. Chapter 6 introduces a semi-rigid element to model additively manufactured cellular materials. Chapter 7 presents a modified homogenization approach that integrates manufacturing effects during the AM process with the property estimation procedure.

Lastly, Chapter 8 concludes by providing an evaluation of this research and suggestions for future work.

CHAPTER 2 Literature Review & Research Gap

This chapter presents an extensive review of related subjects for understanding the state of the art and the limitations of relevant research. To achieve the objective of the research mentioned in Chapter I, it is imperative to identify research gaps between the current development and the goal. In order to provide sufficient background of relative subject, three subjects are reviewed, including process parameter control and process modeling, geometrical degradation, and mechanical property estimation methods. From the review, research gaps were identified and the research direction was established.

2.1 Process Parameter Control and Process Modeling

Since diverse phenomena are involved in AM processes, it is required to control various process parameters to improve fabrication quality and efficiency. From the early stage of AM process development, much research that investigates process parameters to improve the fabrication quality and efficiency of parts been performed [13-15]. In addition, a modeling scheme for AM processes also has been developed to increase understanding of the processes and to assess resulting mechanical and geometrical characteristics [16, 17]. This section presents previous research into improving part quality and fabrication quality for two AM processes: material extrusion and powder bed fusion processes.

2.1.1 Material Extrusion Process

Material extrusion is one of the most well-developed additive manufacturing process. Since there are many parameters involved in the process, optimizing the parameters is an

important task for improving the process. Agarwala et al. investigated the origin of defects that arose in the FDM process [11]. The authors categorized relevant process parameters into four groups as listed in Table 2-1 and explained how the parameters play a role in defect creation. Ahn et al. studied the effects of process parameters, such as deposition path, tip thickness and gaps in the FDM process, on the mechanical properties of the fabricated part [18]. They suggested several modeling rules based on their experimental studies. Sood et al. studied the effects of the process parameters on tensile, flexural and impact strength using the design of experiment (DOE) scheme [19]. They selected five process parameters: thickness, orientation, raster angle, raster width and air gap. They performed optimization for improved strength using the resulting surrogate model. Wang et al. implemented the Taguchi method to establish relationships between manufacturing process parameters and mechanical and geometrical characteristics such as strength, surface roughness and dimensional accuracy [20]. They presented two findings: tensile strength and dimensional accuracy depend on the build direction, and surface roughness is affected by layer thickness. Jin et al. developed a toolpath generation method that optimizes raster angles [21]. The obtained toolpath minimized unfilled area and reduced the build time required.

Table 2-1 FDM FDC and FDMet process variables [11]

Operation specific	Machine specific	Materials specific	Geometry specific
Slice thickness	Nozzle diameter	Powder characteristics	Fill vector length
Road width	Filament feed rate	Binder characteristics	Support structure
Head speed	Roller speed	Viscosity	
Extrusion temperature	Flow rate	Stiffness (column strength)	
Envelope temperature	Filament diameter	Flexibility	
Fill pattern		Thermal conductivity	

Next, process models that provide distribution of physical quantities such as temperature have been proposed to predict the mechanical and geometrical characteristics of fabricated parts. Yardimci and Güçeri developed a cooling process model to predict bonding potential that determines diffusive bonding [22]. Bellini constructed numerical models for simulating thermal-fluid behavior in FDM process [23]. The author examined the deposited filament shape and the distribution of related physical quantities such as temperature and flow velocity. The proposed modeling scheme was implemented for optimizing the nozzle shape. In addition, Bellini and Güçeri estimated mechanical properties based on the mechanical properties of a single filament and a deposition path pattern [24]. They assumed a fabricated material to be orthotropic. Sun et al. focused on the bonding formulation mechanism among deposited filaments [25]. The authors developed analytical models to obtain temperature profiles in deposited filaments and to predict bonding neck diameters based on the temperature profiles. Huang and Singamneni studied the consolidation mechanism in the FDM process for an adaptive slicing scheme [26]. They utilized an analytical model describing the rate of coalescence between two filaments in order to predict the geometrical parameters of deposited filaments, such as the area of a single layer and the second moment of area. Their research shows that the mechanical properties based on predicted filament geometrical parameters match with experimental results. Rodriguez et al. quantified the effect of deposition pattern on mechanical properties based on the constitutive model of a mono-filament [27], and the authors expanded their research to describe defect characterization and predict bonding strength [28].

2.1.2 Powder Bed Fusion Process

Selective laser sintering/melting (SLS/SLM) and electron beam melting (EBM) are mainly implemented as metal AM processes. In both processes, metal powder is melted in a powder bed, but the energy sources are different. Das summarized the important physical mechanisms of the SLS process, such as oxidation, wetting, solidification, vaporization and purification [29]. There are various numerical approaches to investigate the fundamental phenomena of the metal processes. Bugada et al. used thermal FEA to describe the SLS process [30]. Shiomi et al. modeled the melting and solidifying processes based on the balling effect in laser based processes, using two dimensional thermal FEA [31]. They estimated the solidified weight according to various power absorptivity values and compared the evaluations with experimental results. Kolossov et al. implemented nonlinear three dimensional thermal FEA to find a temperature profile during a laser sintering process [32]. The result well followed experimental observation. Zäh and Lutzmann developed a process parameter window from thermal FEA, which guides an appropriate combination of process parameters for an EBM process [33]. Zeng et al. proposed a dynamic meshing method for 3D thermal FEA to speed up the high fidelity FEA of the SLM process [34]. Körner et al. [35] and Markl et al. [36] applied the two and three dimensional lattice Boltzmann methods in order to model the whole EBM process, including stochastic powder distribution, wetting and phase transition. Their implementation resulted in more realistic shapes for deposited geometries.

2.2 Effects of Fabricated Geometries in Cellular material

An additively manufactured part exhibits geometrical errors due to inherent process characteristics. The representative example is the stair stepping phenomenon [37-39]. Since the level of geometrical error is dependent on not the dimensions of the parts but on the process parameters, the relative error is amplified when fabricating small features, whose dimensions are only a few times the dimensions of a deposition tool. Thus, the geometrical degradation is critical in fabrication of cellular materials, which consist of small and thin features such as struts and walls. This section presents diverse previous research into geometrical degradation in cellular materials.

2.2.1 Geometrical Degradation

Much research has reported that cellular materials using AM processes exhibit geometrical inaccuracy and material degradation. Gajdos and Slota measured the volume of internal air gaps and voids in FDM specimens using computer tomography [40]. The result indicated that the material distribution is not uniform and the shape of the fabricated parts affects the number of voids and gaps. Ravari et al. reported the variations in the fabricated diameter of a FDM manufactured lattice structure in the form of a probabilistic distribution [41]. The authors developed numerical models with degraded geometries based on the distribution and performed a stress analysis. The result implied that the models with perfect geometries overestimated mechanical performance and implementation of degraded geometries relieved the estimation error.

Cansizoglu et al. used microscopic observation and reported a discrepancy between designed strut diameters and actual struts fabricated using electron beam melting (EBM) [42]. The authors explained that the differences are from slicing processes used during

the EBM process; these were reduced by optimizing process parameters. The authors concluded that use of the reduced strut diameters, rather than the designed diameters, leads to more accurate estimates of the mechanical properties, based on comparison of experimental results with the results obtained using Gibson and Ashby's approach. Harryson et al. found the same phenomenon in lattice structures fabricated for hip stem implants [43]. They conducted a numerical simulation to find the elastic modulus of a lattice structure by applying the designed strut diameter, and they compared the estimates with experimental results. The estimates were significantly stiffer than the experimental results. Yang et al. recognized that the size of struts is influenced by the stair step phenomenon and the amount of inclination with respect to the build plane, since the heat dissipation condition is changed [44]. Suard et al. [45] and Mandil et al. [46] reported that a considerable number of powder particles are stuck on EBM parts, and these particles degrade dimensional accuracy and surface roughness. Ravali et al. reported the same phenomenon in SLM parts [47]. The authors proposed a stochastic geometric modeling scheme for a strut degraded due to powder in order to consider the defects in their property estimation process.

2.2.2 Integration of Geometrical Degradation

Some researchers used a stochastic approach to mitigate the error between estimates and experimental results. Cahill et al. realized that estimated effective moduli are much higher than measured values [48]. To relieve the overestimation, they constructed a stochastic model of a strut as a varying cross sectional area along the strut axis. Their approach enabled them to reduce errors. Luxner et al. introduced defects as randomly removing struts or joints and made the joint locations deviate in order to study

their effects on the mechanical properties [49]. Babaei et al. implemented irregularity to an arrangement of a lattice structure and reported that the elastic modulus increased but yield strength decreased as irregularity increased [50]. Campoli et al. implemented irregularity caused by the AM process to cross sectional areas [51]. The authors modeled a strut with several connected beams whose area was determined based on the Gaussian distribution, and they implemented a micro mechanics theory to incorporate porosity. This study showed that manufacturing irregularities significantly influence mechanical properties.

2.2.3 Effect of Joint Region

The effects of overlapped areas in a lattice structure on the properties have been also considered. Yang et al. noticed that the amount of overlapped region among struts reduces effective strut length, and the reduction in the effective length affects the evaluation of these properties [44]. The effects were studied in large structures such as buildings, since the overlapped areas significantly affected the inelastic mechanical behavior of a large structure. The area was considered as a semi-rigid joint, while a joint in general frame structures is regarded as a rigid joint. Although research regarding semi-rigid joints has been conducted for large frame structures, the proposed methods could be implemented into the analysis of a lattice structure, since a lattice structure is a mathematical downsizing of a large frame structure. Monforton and Wu proposed a fixity factor in order to describe the rigidity of a joint [52]. The authors used the factor to formulate a stiffness matrix for a semi-rigid jointed frame structure. Simoes optimized the design of a steel framework using a semi-rigid jointed beam formulation [53]. Sekulovic and Salatic introduced an eccentricity to account for the length of an

overlapped region, and they formulated a semi-rigid joint as a combination of a torsional spring and a rigid bar [54].

2.3 Estimating Mechanical Properties of Cellular Material

Various methods have been proposed and implemented for estimating the mechanical properties of cellular materials. In most research, the representative unit cells at the micro-scale are analyzed to determine the macro-scale properties of cellular materials, such as the elastic modulus, the yield strength and the ultimate strength; these analyses are based on the concept that the micro-scale characteristics of a heterogeneous medium govern its macroscopic properties. The procedure to determine macro-scale properties from a representative micro-scale unit cell is called the homogenization process [55]. This is developed for analysis of composites with periodic micro-structures that have a large number of heterogeneities, since analysis of the composites demands high computation cost. The mechanical and material properties of target complex composites is replaced by an equivalent simple homogeneous material through the homogenization process [56]. This process can be used to find the mechanical properties of a periodic lattice structure, since a lattice structure can be considered as a heterogeneous mixture of solid material and void. The homogenization procedure has three steps. First, a structural model of a unit cell is constructed and analyzed to determine selected mechanical responses, such as displacements and forces or strain energy, in the micro-scale. This is accomplished by using analytic closed-form formulas or numerical simulations. Next, the formulas for the macro-scale responses are

developed. Finally, the property estimates are evaluated by equating the mechanical responses in two scales. This section presents a wide range of research on homogenization approaches, including analytic and numerical approaches to clarify the advantage and disadvantage of each approach.

2.3.1 Analytic Approach

Gibson and Ashby are pioneers in this research area. They established a systematic relationship between the relative density and the mechanical properties of a foamlike cellular material [57]. They selected a representative unit cell of the foam and calculated the relative density and mechanical properties such as elastic modulus, Poisson's ratio, plastic collapse strength and buckling strength. They proposed regression models in which the properties are proportional to the power of relative density. The estimates from their models well followed experimental results in comparison. Finally, Ashby expanded this approach to develop material-property charts that compare various cellular materials and hybrid materials and give guidelines for design [58].

Deshpande et al. focused on the lattice structure rather than the foam [59]. The authors classified lattice structures into two groups – stretching dominated and bending dominated lattice structures. They found that the stretching dominated lattice has much greater strength than the bending dominated lattice structure. Collapse and yield strength were compared based on the octet-truss analytic constitutive relationship [2]. Doyoyo and Hu studied a lattice structure composed of short and slender trusses [60]. Hu and Park considered multi-axial loading conditions in order to describe the plastic deformation of octet-truss structures and compared the estimates with numerical results based on finite element analysis [61].

Other types of analytic approaches also have been implemented for an estimation process based on a two-scale expansion and on analytic formulas. An asymptotic homogenization method was developed for finding the effective properties of periodic media beginning in the 1970's. This approach was applied to a lattice structure with discrete elements such as a beam and a truss. Tollenaere and Caillerie assumed that lattice structures are comprised of infinite periodic unit cells, so they utilized an asymptotic expansion on given geometries and forces in order to formulate the self-equilibrium equation [62]. Caillerie et al. implemented this approach to model the mechanical behavior of graphene sheets [63]. Reis and Ganghoffer modified the approach by using beams instead of trusses to model struts, and they calculated the elastic constants of a lattice structure [64]. Kalamkarov et al. and Hassan et al. proposed an analytical asymptotic homogenization method to estimate the elastic constitutive matrix of three-dimensional grid-reinforced composite structures that have lattice-like reinforcements [65, 66]. The authors used the asymptotic homogenization method to formulate a boundary value problem for periodically repeating structures. They solved the problem analytically and derived the constitutive relationship.

A Micropolar approach has also been used, whereby a lattice structure is assumed to be a micropolar continuum, having a micro-rotation at each material point. Kumar and McDowell determined the material constants of a homogenized micropolar continuum by comparing the strain energies in the macro-scale and the micro-scale [67]. The authors extended the method to a convective heat transfer problem to design a degraded lattice structure [68]. Reis and Ganghoffer also extended the discrete homogenization method to the micropolar continuum approach [69].

The analytic approach gives good estimates for selected representative unit cells. However, the formulation process for complex unit cells is time-consuming and complex. This makes it difficult to implement the analytic approach on arbitrary lattice structures. To mitigate the problem, numerical approaches for homogenization have been proposed and developed.

2.3.2 Numerical Approach

Firstly, an FEA model with continuum elements, such as tetrahedrons and hexahedrons, is used to analyze a representative unit cell with periodic boundary conditions. Kim and Al-Hassani discretized a representative unit cell to evaluate the effective elastic constants of two dimensional lattice structures [70]. They found a joint-stiffening effect that reduces bending deformation by comparing their numerical and analytical results. Hassan et al. used the same approach to validate analytic estimates [66]. Luxner et al. studied the localization effects due to irregularities in periodicity by numerically modeling a block of representative unit cells [71]. Arabnejad and Pasini numerically applied an asymptotic homogenization method to two and three dimensional lattice structures. Unit cells were discretized by continuum elements in order to fully describe geometries [72]. Some studies employed an FEA model of a whole lattice structure to compare analytically obtained mechanical properties with experimental results [48, 73]. An FEA model with continuum elements can express details of a lattice structure and provide a good estimate. However, the problem is relatively large, so significant computing resources are required.

Vigliotti and Pasini proposed a multi-scale discrete homogenization approach for a periodic lattice structure based on an FEA model with structural elements such as beams

and plates [74, 75]. The boundary conditions were integrated into a stiffness matrix of a unit cell by adopting the concept of independent and dependent nodes. This approach was successfully applied to two and three dimensional lattice structures and was extended to estimate a nonlinear constitutive relationship [76]. Since this approach yielded a much smaller system of equations to solve than the continuum element approach, the computing cost was reduced.

2.4 Identification of Research Gaps

Based on the literature review, the following three gaps are identified:

- Previous research has focused on modeling the AM process itself rather on the relationship between AM process parameters and the characteristics of the deposited geometries and material. A detailed description of the AM processes has considered parameters such as temperature profiles, phase change and solidification. However, the research into modeling the deposited geometries and material properties using given process parameters is limited.
- Although research has reported various types of geometrical and material degradation induced by the AM processes in various length scales, these effects are not treated systematically. There are limited studies regarding how the effects are propagated as the length scales of geometries are increased. The effect can be quantified by considering the characteristics of the AM process.

- Estimates from the homogenization procedure for mechanical properties significantly differ from the measured properties of a lattice structure. Previous studies of the homogenization procedure have focused on developing a method mathematically. They use perfect geometries and material properties, which cannot be achieved using the AM processes. This can be relieved by considering the effects of AM processes.

2.5 Chapter Summary

This chapter has reviewed a wide range of previous research relevant to the objective of this research. Firstly, process parameter control and process modeling schemes for material extrusion and powder bed fusion processes are presented. In the material extrusion process, the shape and pattern of deposited filaments affects the geometrical and mechanical properties. In the powder bed fusion process, thermal characteristics are important factors for fabrication quality. Secondly, research on accessing the effects of inaccuracy shown in fabricated geometries on mechanical properties is reviewed. Much research has proposed to consider dimensional inaccuracy in the additively fabricated parts, since the geometrical error is not negligible. Several schemes have been developed to account for joint regions in frame structures, which are mechanically similar to cellular materials. Finally, diverse homogenization approaches are reviewed. The methods are mathematically well developed but do not reflect manufacturing effects. Based on the literature review, three research gaps are identified. The research gaps will be addressed in formulation of the research framework in the next chapter.

CHAPTER 3 Formulation of Research Framework

This chapter proposes a research framework in order to develop a property estimation procedure for cellular materials. The proposed framework considers various kinds of parameters emerging in AM processes. The parameters are identified based on manufacturing process characteristics and their size scale, and are classified into four groups. The framework is composed of three transformations that map smaller scale parameters to larger scale parameters. Three research questions are derived based on parameter groups and transformations in this chapter.

3.1 Proposed Research Framework

Manufacturing processes affect part and material parameters at several different size scales. The manufacturing setting has an impact on deposition conditions, and this can alter the as-manufactured layer shape. In addition, deposition strategy is adjusted based on part design and, as a result, the part design influences on the as-fabricated layer shape. Therefore, the manufacturing setting and part design lead to variations in the as-deposited shape. The variations within a layer affect mechanical and geometrical characteristics at the level of structural elements, which are fabricated features such as struts in a cellular material. Moreover, since a cellular material consists of a large number of structural elements, their mechanical and geometrical characteristics change the mechanical properties of the entire part. In this context, a research framework is proposed based on a three-step homogenization approach as shown in Figure 3-1. In the proposed framework, all relative parameters are classified into four groups; Design and manufacturing process parameters, Layer deposition parameters, Structural element parameters, and cellular material properties. The estimation procedure is established by

defining transformations among the parameter groups. The transformations are defined based on consideration of the characteristics of the AM processes and part design.

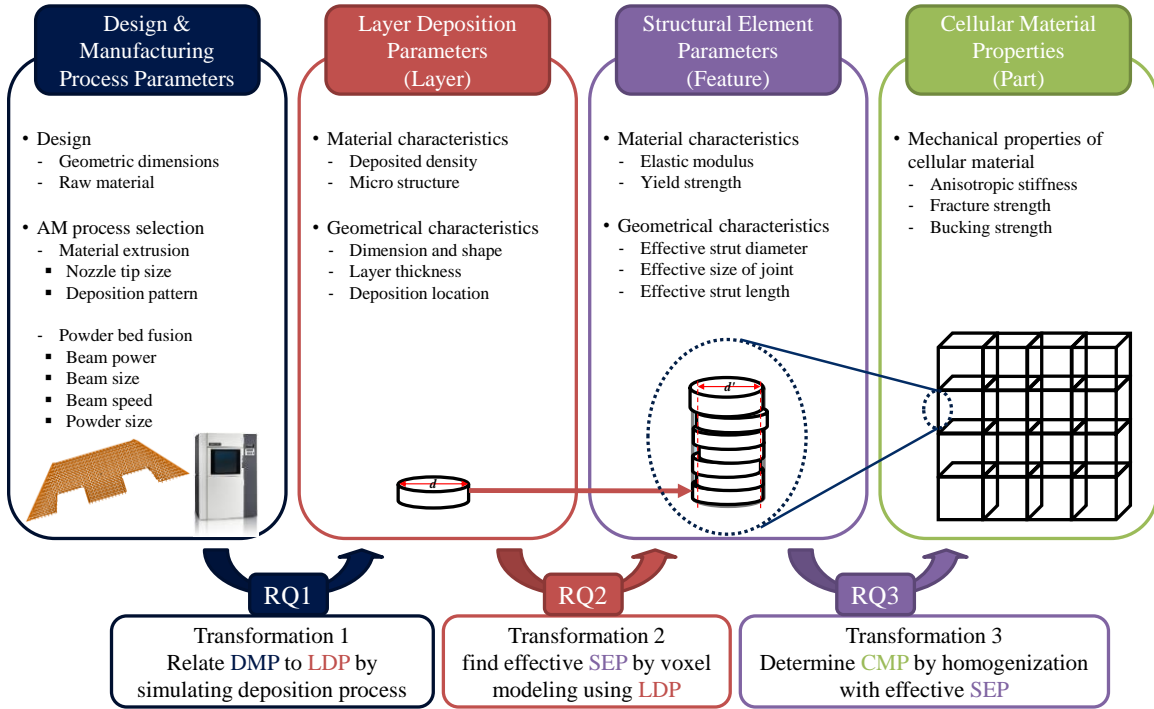


Figure 3-1 Overall Problem Formulation

3.2 Parameter Classification

In order to establish the property estimation procedure in a mathematical manner, diverse parameters need to be identified and defined, to include the manufacturing parameters for a selected AM process, the design parameters for the target cellular material, the geometrical and material parameters for the as-manufactured cellular material, and the resultant mechanical properties. These parameters appear in certain stages of an AM process and have different characteristic length scales. In order to consider these variables systematically in the estimation procedure, it is necessary to

classify these parameters into groups according to their length scales and the steps where they are introduced as shown in Figure 3-2. A detailed explanation is presented in the following sections.

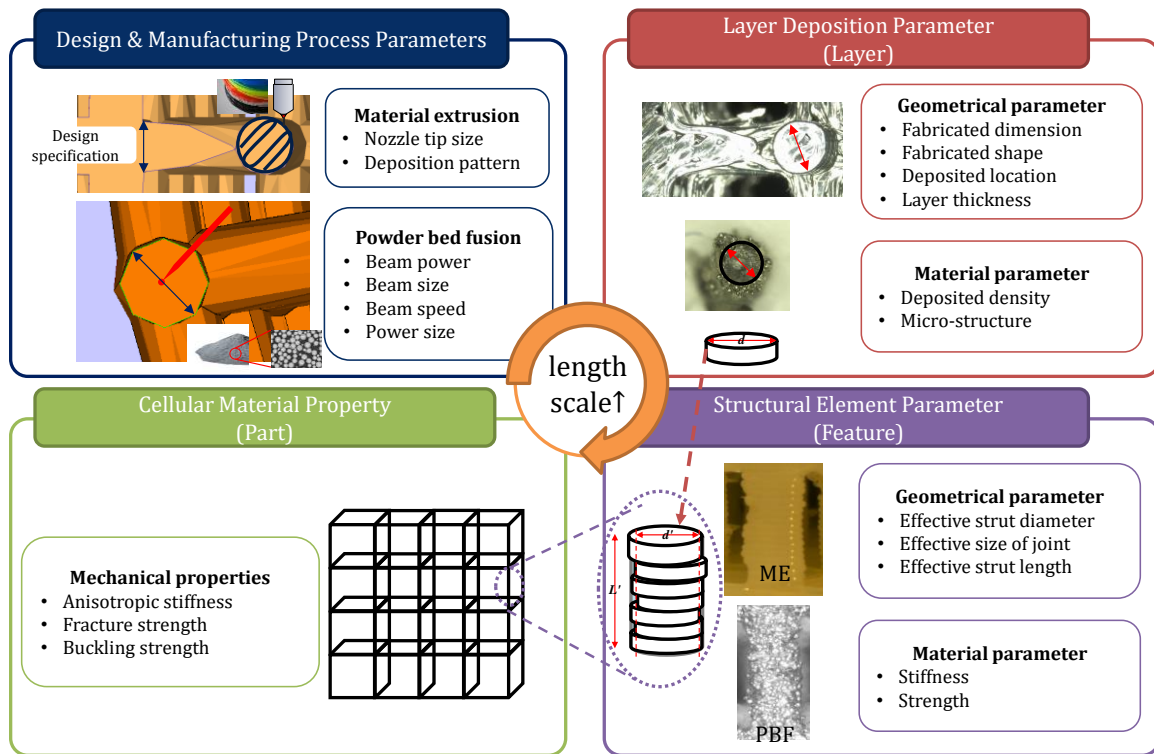


Figure 3-2 Classification of parameters

3.2.1 Design & Manufacturing Process Parameters

Design and manufacturing process parameters (DMP) define two sets of parameters, which are pre-determined before fabrication. The first set of parameters is the design parameters and the second is the manufacturing process parameters. The design parameters describe design specifications, including the geometrical dimensions and applied materials to features, such as the strut diameter and length, wall thickness, the

size of the unit cell and the material properties of the raw materials. Manufacturing process parameters represent the parameters required to operate the selected AM machine, *e.g.*, nozzle tip size and deposition pattern in material extrusion, and powder particle size and beam size, power and speed in powder bed fusion. The selected manufacturing parameters are listed in Table 3-1.

The DMP parameters play the role of a set of input parameters for fabricating a cellular material. In this research, the design parameters were supplied using a solid model in the form of a Stereolithography (STL) file, in which all design parameters are combined. The manufacturing parameters were obtained from the manufacturer’s specification sheets for a selected AM machine.

In order to capture process-induced uncertainty, the characteristics of each parameter are considered. Since the design specification is explicitly defined, it is assumed that the design parameters are deterministic. However, manufacturing process parameters are defined in a probabilistic manner due to the manufacturing tolerance of AM machines. The nominal values in the specification sheet are set to the mean value of distribution, and the deviations are determined by measuring fabricated parts.

Table 3-1 Selected manufacturing process parameters

AM process	Selected parameters	Description
Material extrusion	Nozzle tip size	Stochastic
	Deposited width	Stochastic
	Infill raster angle	Deterministic
	Location of deposition	Stochastic
Powder bed fusion	Powder particle size	Stochastic
	Beam power	Deterministic
	Beam size	Deterministic
All	Build angle	Deterministic
	Layer thickness	Deterministic

3.2.2 *Layer Deposition Parameters*

Layer deposition parameters (LDP) describe the geometrical and material characteristics of as-deposited geometries in a layer scale. The LDP parameters mainly depend on slicing and deposition path generation processes, since the geometries are shaped by placing material along the deposition path. These parameters contain cross sectional information at each layer during additive manufacturing. This group of parameters includes the dimensions, shape and location of the deposited layer, and the material properties such as density and microstructure.

In order to define the LDP parameters, a complex data structure is required, since LDP parameters are able to construct deposited geometries. In addition to this, the parameters are affected by the DMP parameters, which are defined in stochastic description. This leads to difficulties in managing information in the parameters. For this reason, a deposition shape image is used to express the deposition geometries, as shown in Figure 3-3. Each pixel in the image has 8 bits gray-scale intensity that is able to represent 256 different materials. From the image, the LDP parameters are calculated using image processing techniques.

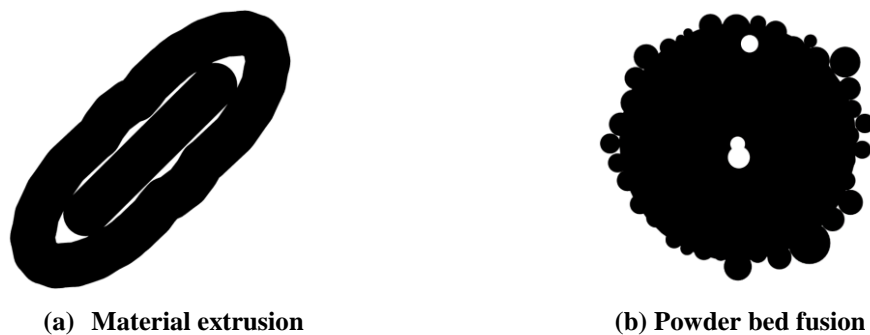


Figure 3-3 Deposition shape images

3.2.3 *Structural Element Parameters*

Structural element parameters (SEP) describe the overall dimensions and mechanical characteristics of features, such as struts and joints, of which a cellular material is comprised. Since the structural elements are built by stacking layers repeatedly along the build direction, deviations in the layer deposition parameters accumulate and geometrical irregularities occur in the elements. Thus, the parameters are expressed as the effective values that equate mechanical behaviors of the element to fabricated elements. For lattice structures, the parameters include effective dimensions and mechanical properties such as an effective size of struts and joints, and elastic moduli and yield strength of struts and joints.

The SEP parameters are represented stochastically due to uncertainties in layer deposition parameters. Thus, the effective structural element parameters are distributed in a certain range. To model the distribution, the stochastic moments, such as mean and deviation, are used.

3.2.4 *Cellular Material Properties*

Cellular material properties (CMPs) represent mechanical characteristics of additively fabricated cellular materials. The CMPs are defined in largest length scales in this research. These parameters are the output of the proposed estimation process. Of interest in this research are three mechanical properties of fabricated cellular materials: the anisotropic stiffness, the yield strength, and the buckling strength.

3.3 Transformations

Manufacturing instabilities in the design and manufacturing parameters, which originate from machine tolerance specification and AM process characteristics, are propagated through the layer stacking process. Manufacturing instabilities lead to geometric and material inaccuracy in the layer deposition parameters, and they affect accuracy in the structural element parameters. As a result, the fabricated cellular material incurs geometrical and mechanical degradation. Figure 3-4 presents a schematic diagram for uncertainties propagation and degradation.

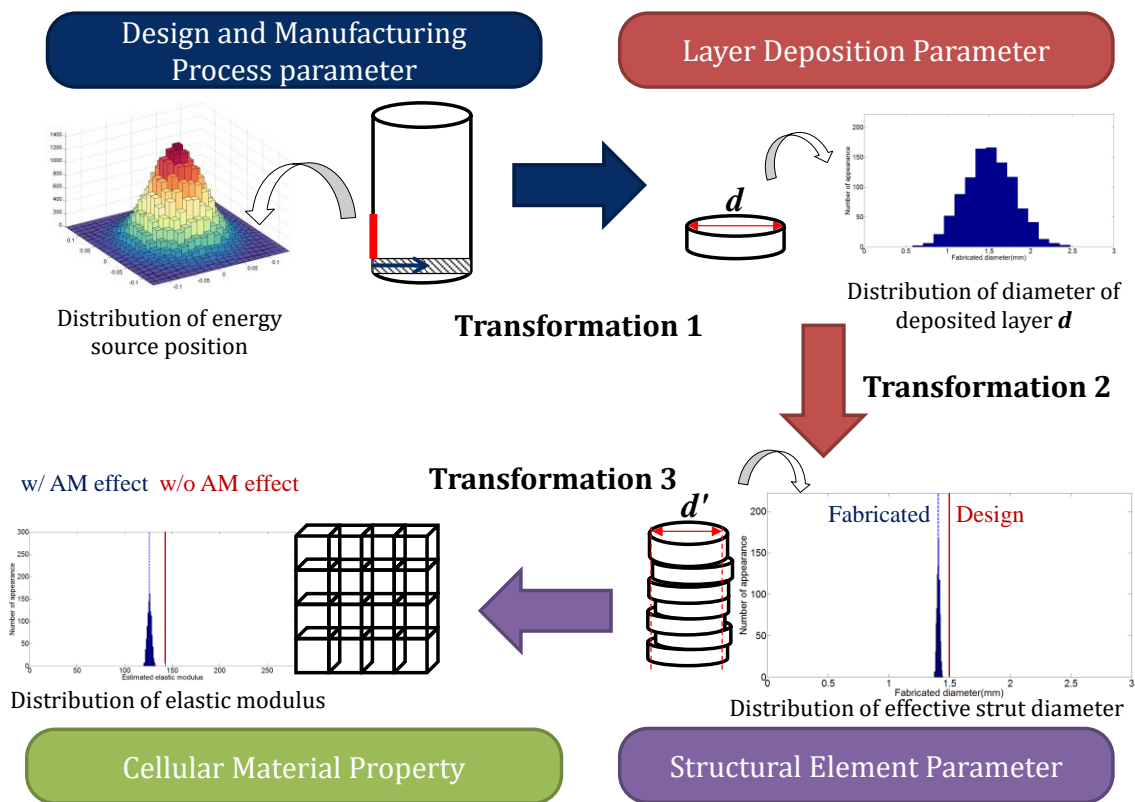


Figure 3-4 Propagation of manufacturing instability through transformations

This research divides the entire property estimation process into three steps, mimicking the AM process. For each step, a transformation is defined to describe how manufacturing instabilities in a certain parameter group affect those in a following parameter group, and to explain how the parameter groups are related. In total, three transformations are formulated among the four parameters groups.

3.3.1 Transformation 1: DMP to LDP

The first transformation explains the relationship between the first two groups. This relates design and manufacturing process parameters to layer deposition parameters. Since there are diverse mechanisms in the AM process machines by which geometrical errors may be generated and material properties may deteriorate, deposited geometries show deviations from target geometries and material characteristics. Thus, the first transformation would establish the relationship based on consideration of the characteristics of the selected AM process.

In this research, the first sub-problem is to define the transformation between the design and manufacturing process parameters and the layer deposition parameter. Specifically, the inputs of this transformation are a solid model of a cellular material and machine specifications. The output is a set of deposition shape images that represent deposited geometries at each layer.

3.3.2 Transformation 2: LDP to SEP

The second transformation describes how the effects of AM processes on layer deposition parameters are propagated into structural element parameters through the stacking process. Since the structural features are constructed by depositing successive

layers, the geometrical and material parameters of structural features will be influenced by fluctuations in layer deposition parameters.

In this context, the second sub-problem is formulated as developing the transformation that maps layer deposition parameters into structural element parameters. The input of the second transformation is a set of deposition shape images, and the outputs are the effective values of geometrical and material parameters that are required in the estimation process formulation.

3.3.3 Transformation 3: SEP to CMP

The last transformation establishes a relationship between structural element parameters and cellular material properties. This transformation homogenizes repeatedly arranged geometrical features in a cellular material and converts a cellular material into an equivalent media. This transformation determines the homogenized mechanical characteristics.

In this research, the third sub-problem is to estimate effective mechanical properties based on effective structural element parameters. The input of this transformation is the effective value of structural element parameters, and the outputs are three mechanical properties: the anisotropic stiffness, the yield strength, and the buckling strength.

3.4 Research Questions

In order to achieve the objective of this research, three research questions are investigated for each transformation. This section presents the detailed description of research questions and corresponding hypotheses.

The first research question focuses on functional relationships between the design and manufacturing process parameters and the layer deposition parameters. The geometrical dimensions and material properties of deposited layers deteriorate during the AM process. There are intrinsic uncertainties and inaccuracies in the design and manufacturing process parameters of the selected AM process. These yield mismatches between desired and fabricated layer deposition parameters because they are propagated into layer deposition parameters through the deposition process. Research question 1 is about how to assess quantitatively the effects of manufacturing process and design parameters on the layer deposition parameters as follows.

Research Question 1: How are functional relationships between the design and manufacturing process parameters and the layer deposition parameters quantitatively explained?

Hypothesis 1: The functional relationships can be explained by use of process-modeling simulation and the computation of stochastic distributions of LDPs using a Monte Carlo method. The LDPs can be evaluated based on deposition shape images, which are obtained from the process-modeling simulation.

Explanation: The uncertainties and inaccuracies in the selected AM process can be expressed as stochastic random variables. The manufacturing instabilities modeled as stochastic random variables can be incorporated into the process-modeling scheme for the selected AM deposition process by applying their probabilistic distributions to the

deposition shape image generation. The quantitative relation between the DMP parameters (inputs) and the LDP parameters (outputs) is constructed by Monte Carlo simulation with deposition shape images. Thus, we can define the functional relationship based on the process-modeling scheme in order to cover the entire range of various parameters with limited computing resources.

The second research question aims to investigate the effects of variation in the layer deposition parameters due to AM processes on the structural element parameters. A cellular material consists of structural elements such as struts and joints. The characteristics of the structural elements dominate the effective properties of a cellular material. The structural elements produced by AM processes are inherently degraded, because geometric and material variations occur in a layer deposition step, and they accumulate through the repeated stacking procedure. Thus, the structural elements will not perform as intended. Research question 2 is about quantification of propagated variation between layer deposition parameters and structural element parameters as follows.

Research Question 2: How is the propagation of geometrical and material variations from the layer deposition parameters to the structural element parameters quantitatively described through the repeated stacking procedure?

Hypothesis 2: The effective values of the structural element parameters, such as the sizes of joints and struts, may quantify the geometrical and material variations that accumulate

during the repeated stacking procedure. These effective values can be determined by equating the analytic formula for structural elements and the mechanical responses from numerical analysis using a voxel based model that mimics the layer stacking process.

Explanation: The use of effective values for structural parameters takes the effects of variation into account for measuring the mechanical performance of the structural elements. The effective values can be determined from voxel-based models of structural elements, since the stacking process in AM is similar to the voxel generation process. Each layer reflects degradation, and the degradation accumulates into voxel models of structural elements as the layers stack up. Therefore, the mechanical response of the voxel models implies the amount of the degradation and the effective values of structural elements, which means that equivalent geometrical dimensions and material properties can quantify the effect of the variations.

The third research question focuses on a homogenization approach that enables integration of manufacturing effects into the mechanical property estimation procedure. The discrete homogenization technique has been used to estimate the mechanical properties of a periodic medium by analyzing a representative unit cell. In this method, the unit cells are expressed by discrete structural elements such as trusses, beams and plates. The mechanical behavior of the unit cells is dominated according to the assumptions made about the structural elements and the characteristics of the structural elements used for constructing the numerical model of the unit cell. Thus, the effects of the AM process can be incorporated into the estimation process by selecting proper

structural elements that provide additional parameters for reflecting the variations during the AM process. Research question 2 is about reformulation of the discrete homogenization technique for additively manufactured cellular materials as follows.

Research Question 3: What numerical method can be implemented in order to formulate an estimation procedure for the mechanical properties of a periodic cellular material fabricated by the AM process?

Hypothesis 3: The discrete homogenization technique can be used to estimate the mechanical properties for the cellular material, and the parameters for integrating the effects of the AM process could be introduced by employing semi-rigid jointed frame elements to model the representative unit cell.

Explanation: The semi-rigid jointed frame element provides additional structural element parameters for describing jointed structures. The semi-rigid jointed frame element can describe more details about the behavior of a joint as well as a strut rather than beam or truss elements. Therefore, the discretized homogenization method with semi-rigid jointed frame elements will enable us to incorporate additional parameters for the effects of the AM process into the estimation of the mechanical properties of a cellular material. Implementing the AM process in the form of probabilistic distributed structural parameters will lead to probabilistically distributed estimation of the mechanical properties through the homogenization process. The resulting property distribution will show how the properties are degraded from the desired properties due to the AM process.

Research question 1 is answered in Chapter 4, research question 2 is answer in Chapter 5, and Research question 3 is answered in Chapters 6 and 7.

3.5 Chapter summary

In this chapter, the proposed research framework was explained. In order to consider a wide range of relevant parameters systematically, four groups of parameters was proposed and all involved parameters were classified into the groups. Based on parameter classification, three transformations were defined. To formulate the transformations, three research questions were made and corresponding hypotheses were explained.

CHAPTER 4 Deposition Shape Modeling

This chapter presents a method for modeling an as-deposited shape of a layer using AM processes. The goal of this chapter is to answer research question 1. The deposited geometries depend on the deposition mechanism as well as the type of raw material. In addition, the deposited shape is affected by the pattern of deposition paths. The presented method aims to determine as-deposited shapes in material extrusion and powder bed fusion processes. In order to construct deposition shape images, their deposition processes are modeled and analyzed. Based on process modeling, several assumptions for deposited geometries are made, and they are applied to the procedure for deposition shape image generation.

4.1 Material Extrusion Process

Material extrusion deposits a raw material in the form of a thin filament along pre-determined deposition paths. The conceptual process diagram is presented in Figure 4-1. The raw material is fed into the head, and it is melted in the liquefier. The melted material is extruded through a nozzle tip along pre-calculated deposition paths, which are determined based on the design. Consequently, the as-deposited shape depends on the deposition paths. In addition to this, the shape is also dependent on the manufacturing parameters, since the parameters disturb the dimensions and location of the extruded filaments. Therefore, in order to model the as-deposited shape, two schemes need to be addressed: a method to generate deposition paths from a given solid model and a strategy to integrate manufacturing instabilities arising in the deposition process. This section

explains a procedure to generate deposition shape images for material extrusion based on deposition path generation and manufacturing instabilities.

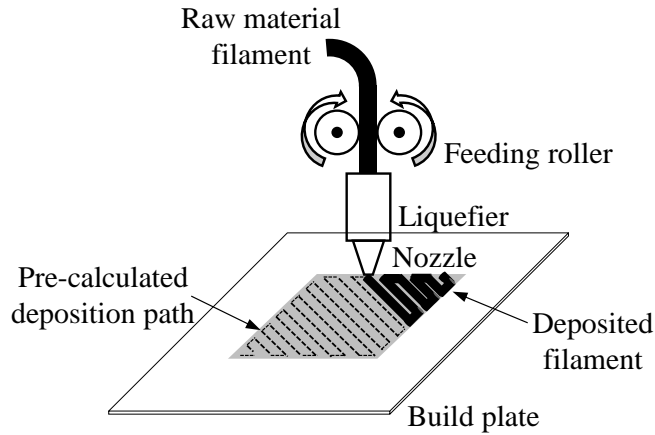


Figure 4-1 Schematic illustration of material extrusion process

4.1.1 Deposition Shape Image Generation Procedure

Since the AM process repeatedly deposits material in a two-dimensional plane in order to fabricate a three-dimensional part, the deposition shape can be described based on a set of two-dimensional images. The procedure to obtain the set of images consists of three steps. Figure 4-2 shows each step in the procedure.

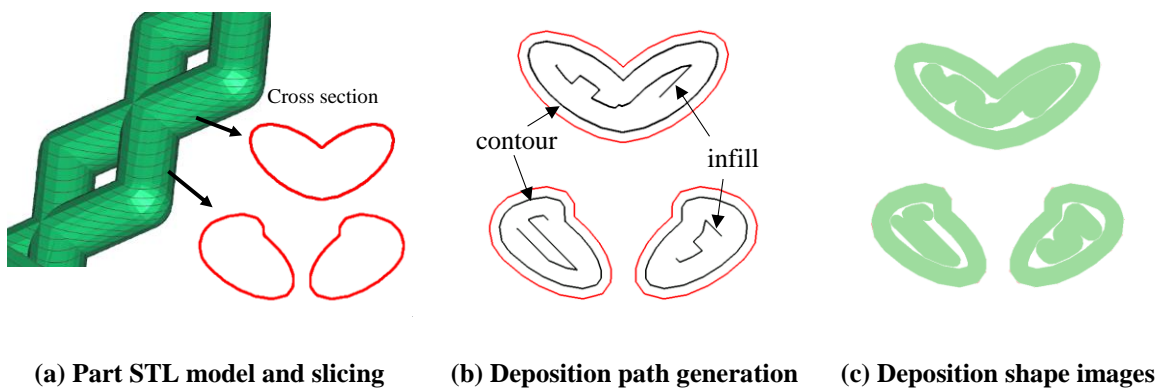


Figure 4-2 Deposition shape generation procedure

In the first step, information on cross sections is obtained by slicing a solid model of a part, which is supplied in the form of a stereolithography (STL) file. The file contains data on a set of triangles, such as the coordinates of vertices and outward normal vectors, which are required to define bounding surface of the solid model. In this step, points on the cross sectional boundaries and outward directions at the points are calculated. Figure 4-2 (a) shows cross sectional boundaries after slicing.

In the second step, deposition paths are generated based on the boundaries in the first step. There are two types of deposition paths in material extrusion: contour and infill deposition paths as shown in Figure 4-2 (b). The contour deposition paths are generated along the cross sectional boundaries. The infill deposition paths are created to fill areas inside the contour deposition paths. The pattern of infill deposition paths controls the density of the deposited geometries. In this research, the pattern is set for solid filling (fully packing).

In the third step, a deposition shape image is constructed by sweeping the nozzle tip geometry along the deposition path. Figure 4-2 (c) shows deposition shape images. The as-deposited model from this procedure can describe only the ideal deposition shape, which cannot be achieved in the as-deposited shape due to manufacturing instability. In order to integrate the instability, probabilistic distributions are assumed for manufacturing process parameters in this step, and they are incorporated into the sweeping process.

4.1.2 Calculating Deposition Path

In order to obtain deposition paths for material extrusion, two AM process parameters are required: a layer thickness and a deposited filament width. The layer

thickness is assumed to be deterministic, which is set in the selected machine. The deposited width is dependent on the layer thickness and is considered as a stochastic variable whose mean value is defined as multiples of the layer thickness. The multiplier is determined based on the selected machine. In this research, the multiplier is set from 1.75 to 2 by examining the slicing information of the machine. The deviation is determined based on measurement. However, the deposited width is fixed to the mean value in this step because the deposition path is calculated before fabrication.

The first step of deposition path generation is to obtain cross sectional boundaries by slicing the input STL. Slicing is performed at a set of levels along the building direction. Figure 4-3 shows the slicing procedure. Firstly, triangles intersecting with a build plane located at a certain height are collected. Next, two intersecting points on edges are calculated for each collected triangle by interpolating the coordinates of its vertices. Finally, the cross sectional boundaries are obtained by connecting the points in the counter clockwise direction.

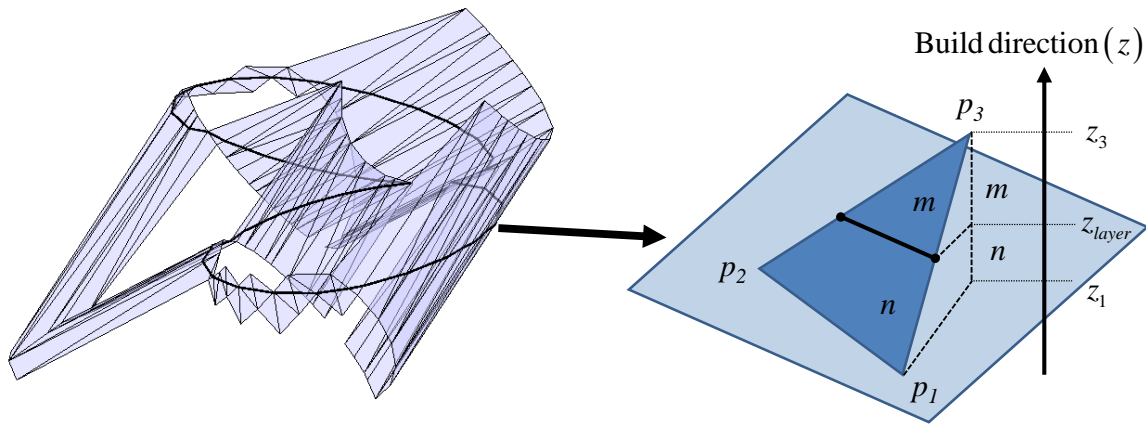


Figure 4-3 Slicing procedure

The second step is to generate contour deposition paths and their inner boundaries by offsetting the cross sectional boundaries in the opposite direction of outward normal vectors. The offset distances are half of the deposition width for the contour deposition paths and are full width for the inner boundaries, respectively. Figure 4-4 represents the obtained contour deposition paths and inner boundaries.

The final step is to calculate infill deposition paths. The paths are parallel to a certain direction, defined as a raster angle except for connections. An infill deposition path is determined by connecting two offset points from intersecting points between the path and the inner boundaries, as shown in Figure 4-4. This procedure is repeated until no more paths can be defined.

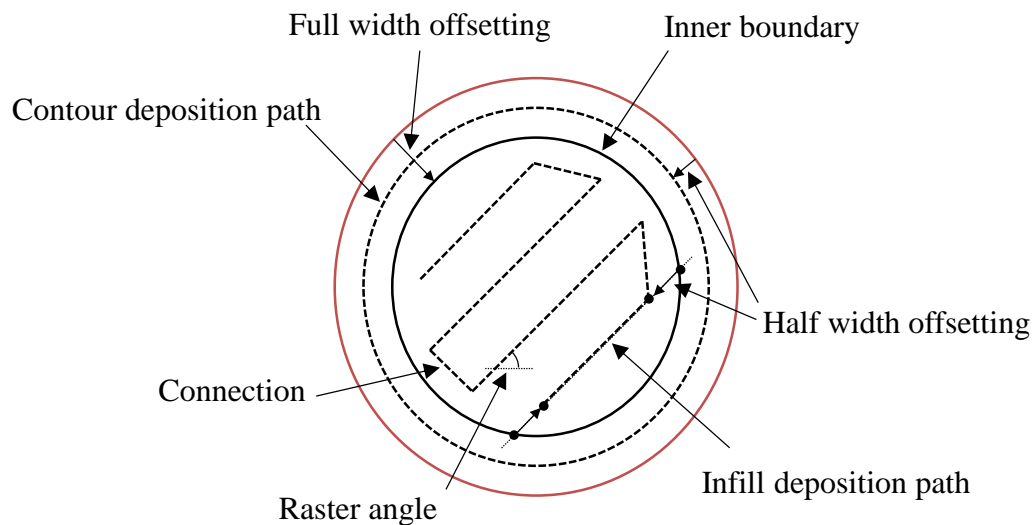


Figure 4-4 Toolpath and deposition image generation

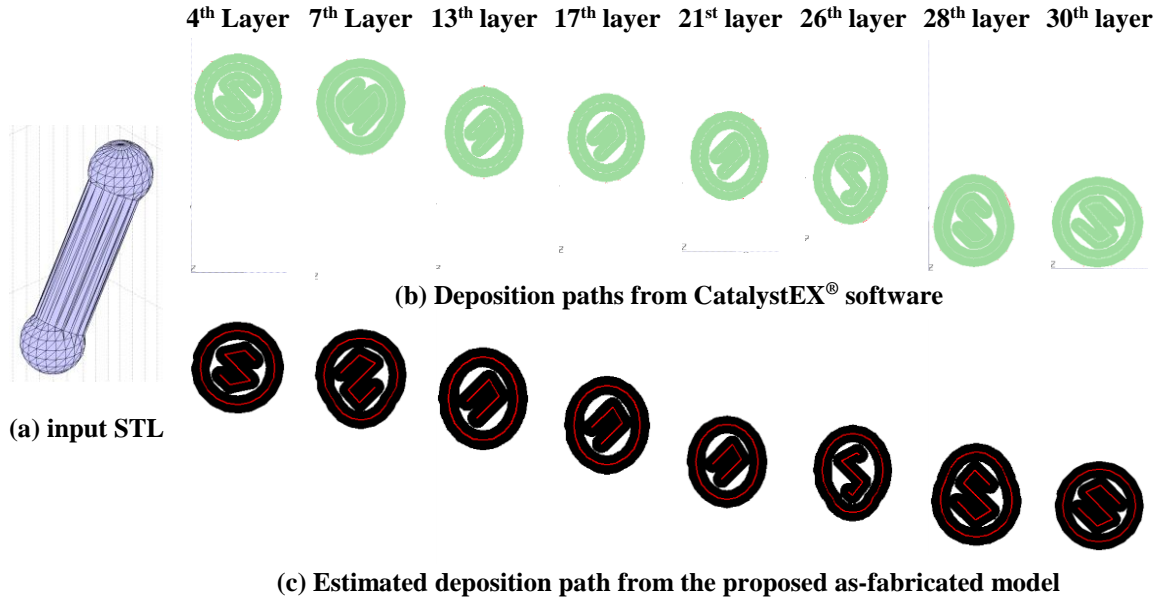


Figure 4-5 Validation of deposition path generation procedure

In order to validate the proposed procedure, the resulting deposition paths are compared with commercial AM supporting software, the Catalyst EX[®] from Stratasys[®]. The resulting paths yield similar infill deposition paths and void patterns, as shown in Figure 4-5. In the latter part of this research, both the proposed procedure and the software are utilized. The software is used for parts that are fabricated in Stratasys Dimension 1200es[®].

4.1.3 Considering Manufacturing Instabilities

In order to deposit material by extrusion, the extrusion head moves along a series of points on the deposition paths and extrudes filaments. Accordingly, two manufacturing instabilities can be considered in the deposition process. The first is uncertainty arising in head movement. Since the head movement has machine tolerances, the actual location of

deposition is not the same as the deposition paths determined in the previous chapter. To describe this uncertainty, the location of each point in the deposition paths is disturbed. In this research, the uncertainty is modeled based on the literature [77, 78]. Bochmann et al. reported that the range of translational error of the nozzle tip is 0.011-0.014 mm in the Stratasys® SST 1200es machine, which is used in this research [78]. To model the uncertainties, two one-dimensional uniform distributions are established for the two directions on build plane.

The second instability is shown in the extrusion process, and it affects the deposition width. Since the amount of deposition depends on manufacturing parameters, such as material feeding speed and head speed, the deposition width is not fixed to the value of deposition width in the previous section. To express this discrepancy, a scaling factor is introduced to adjust the width. The distribution of the scaling factor is modeled using a one-dimension normal distribution with the mean value of 1.094 and the standard deviation of 0.0653 based on measurement. For each connected deposition path, the same value of the scaling factor is applied.

4.1.4 Generation of Deposition Shape Images

The procedure for generating deposition shape images consists of two steps. The first step is to construct a geometric model of the deposition shape. The deposition shape of a segment in the deposition path can be modeled using two circles and a rectangle, as shown in Figure 4-6, which presents a general sweep operation. The circles and rectangles are modeled using wireframe primitives. The perimeter of the circles is divided into 36 points, and the rectangle is defined using four vertices. The dimensions

and location of the wireframe models are adjusted by means of scaling, translation and rotation operation.

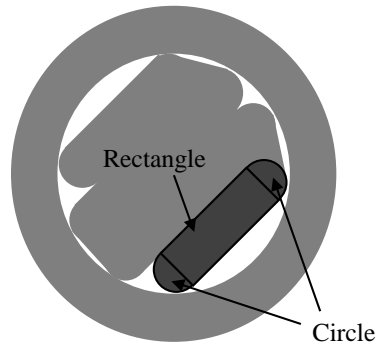


Figure 4-6 Deposition shape image generation

In the second step, the geometric model is converted into an image by drawing all generated circles and rectangles on a preset window where the image resolution and the number of pixels are specified. For example, the geometries are visualized using ‘fill’ or ‘patch’ commands in MATLAB[®]. Since the image is in greyscale, as shown in Figure 4-7 (a), it needs to be converted into a binary image as shown in Figure 4-7 (b). The process is performed by setting intensity to zero for pixels under a threshold value and to one for other pixels. In this research, the threshold value is set to 128, which is the median in the 8 bit image.

In this research, the as-deposited shape is described using an image. Since the resolution of the image affects the accuracy of deposition shape representation, selecting proper resolution is important. As higher resolution is used, the image becomes more accurate, but more computational resources and computing time are required. The resolution affects the accuracy of an analysis model in the later chapter. Therefore, the

resolution is selected based on parametric studies for modeling accuracy and computation time required as presented in Sections 4.3 and 5.2.

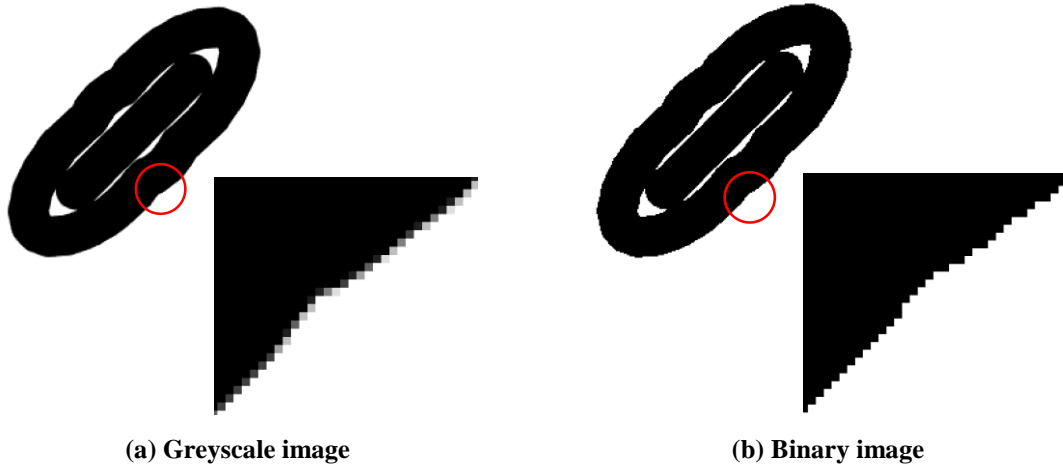


Figure 4-7 Comparison between greyscale and binary image

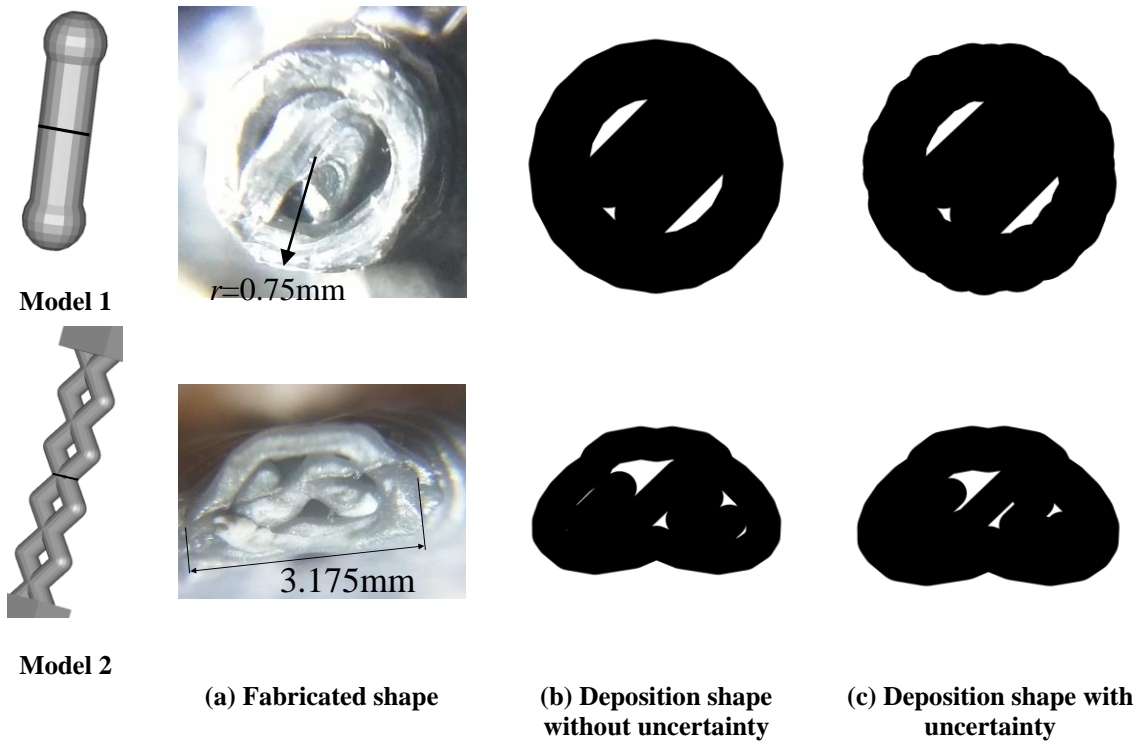


Figure 4-8 Shape comparison for ME process

The proposed method was applied to two strut models. Model 1 has 1.5 mm strut diameter, and it was built in the Stratasys[®] Fortus 400mc FDM machine with a T12 tip, which has 0.178 mm of the filament size. The model 2 has 2 mm of strut diameter, and the Stratasys[®] Dimension SST 1200es FDM machine was used for fabrication with a T16 tip that leads to 0.254 mm of the nozzle size. The resulting deposition images are presented in Figure 4-8. The result shows that the deposition shape images are similar to fabricated geometries.

4.2 Powder Bed Fusion Process

The PBF process uses a laser beam or an electron beam as a heat source to melt a powdered raw material. Powder particles are spread on the top surface in a vat and are preheated to a point below the melting temperature of the raw material. After preheating, a laser or electron beam is scanned along pre-calculated deposition paths in order to melt and fuse the powdered material. Therefore, the deposited shapes are affected by the size and thermal characteristics of the powders as well as by the characteristics of heat sources, such as the beam energy and the beam spot size.

This section explains a modeling procedure to generate deposition shape images for the PBF process. The procedure is developed based on two components. The first is to model a powder bed to consider the characteristics of powders. The second is the set of assumptions derived from heat transfer analysis using the powder bed model. Since this research focuses on fabrication of a cellular material, it is assumed that the proposed procedure is confined to generating deposition images of thin features, which dimensions are up to three times bigger than the beam size.

4.2.1 Powder Bed Modeling

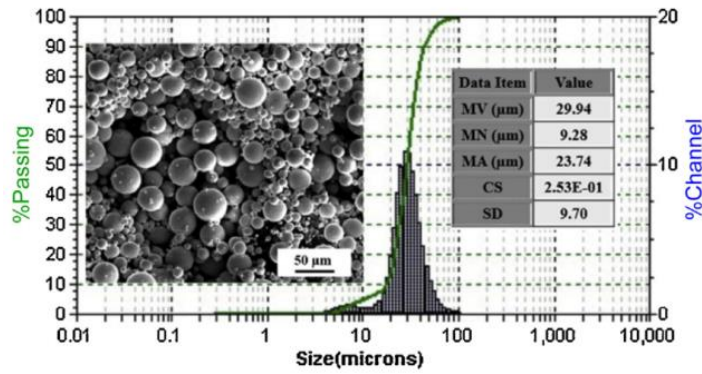
Since the dimensions of structural features in a cellular material are not typically large enough to neglect the powder size, the distribution of powder particles in the bed influences the deposition shape. Powder particles stuck on a small sized strut increase the apparent strut size and yield as-deposited shapes that are different from the design specification. In consequence, the characteristics of a powder bed are important components for constructing deposition shape images. In order to capture the characteristics, a powder bed modeling approach is developed based on powder morphology and a particle packing method.

This research considers two commercially available Ti-6Al-4V powders for the SLM and EBM processes [12]. Figure 4-9 shows powder morphology and particle size distributions. The Raymor[®] powder used in the SLM process has a smaller average particle diameter than the Arcam[®] powder used in the EBM process. The mean volume diameters are 29.94 μm for Raymor and 72.69 μm for Arcam, respectively, and the standard deviations are 9.7 μm for Raymor and 17.74 μm , respectively. These statistical quantities are utilized for a modeling procedure to generate powder particles randomly.

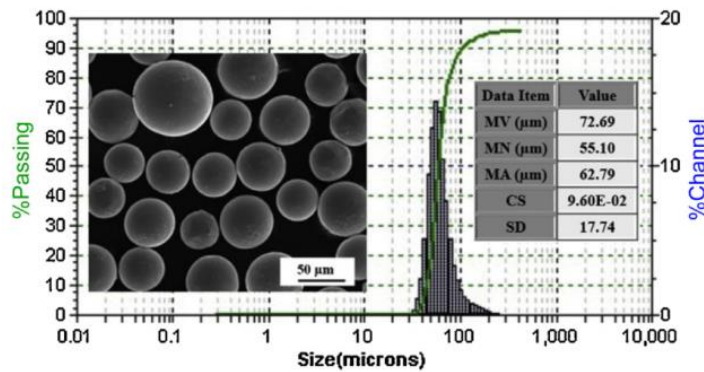
The obtained powder bed model shows higher packing density than the actual powder bed does. To adjust the packing density, some particles are randomly selected and are removed until the target packing density is achieved. The packing density is set to 65%.

Figure 4-11 shows powder bed models with two types of powder before and after the adjusting procedure. The Arcam[®] powder has larger particle size; the resulting

powder bed consists of a smaller number of powder particles. The powder bed model stores information on particle size and location.



(a) Raymor Ti-6Al-4V powder



(b) Arcam Ti-6Al-4V powder

Figure 4-9 Powder morphology and particle size distribution [12]

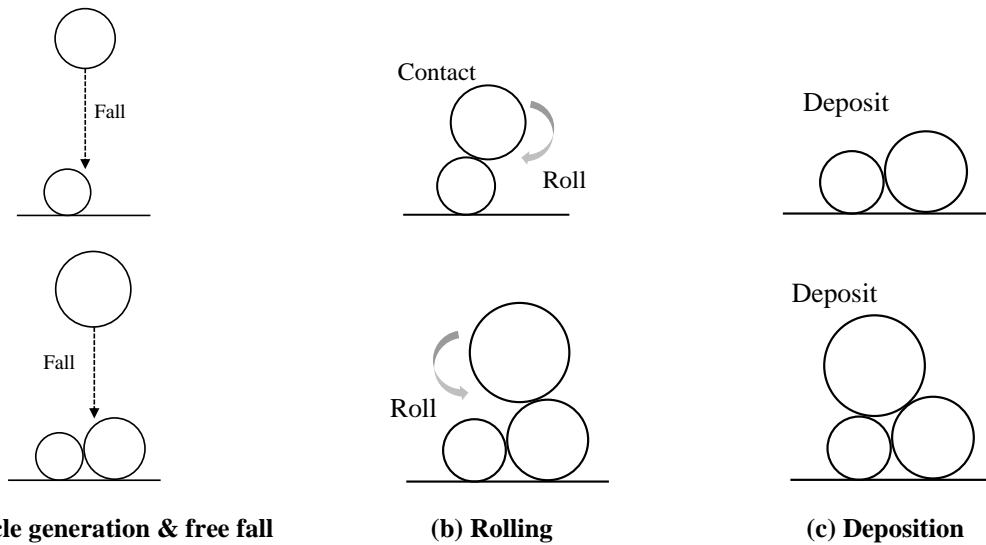


Figure 4-10 Particle packing procedure using the rain model

This research utilizes the two-dimensional rain model, which has been implemented in PBF process simulation [79, 80]. Figure 4-10 represents the particle generation procedure. Firstly, a randomly sized particle is generated and is dropped from the top, as in Figure 4-10 (a). Once the particle contacts one of the pre-located particles, the particle starts to roll in order to find a stable position as in Figure 4-10 (b); this means touching the bottom or being located between two particles. After finding a stable position, the particle is deposited as in Figure 4-10 (c). The deposition process is repeated until all available space is filled with powder particles.

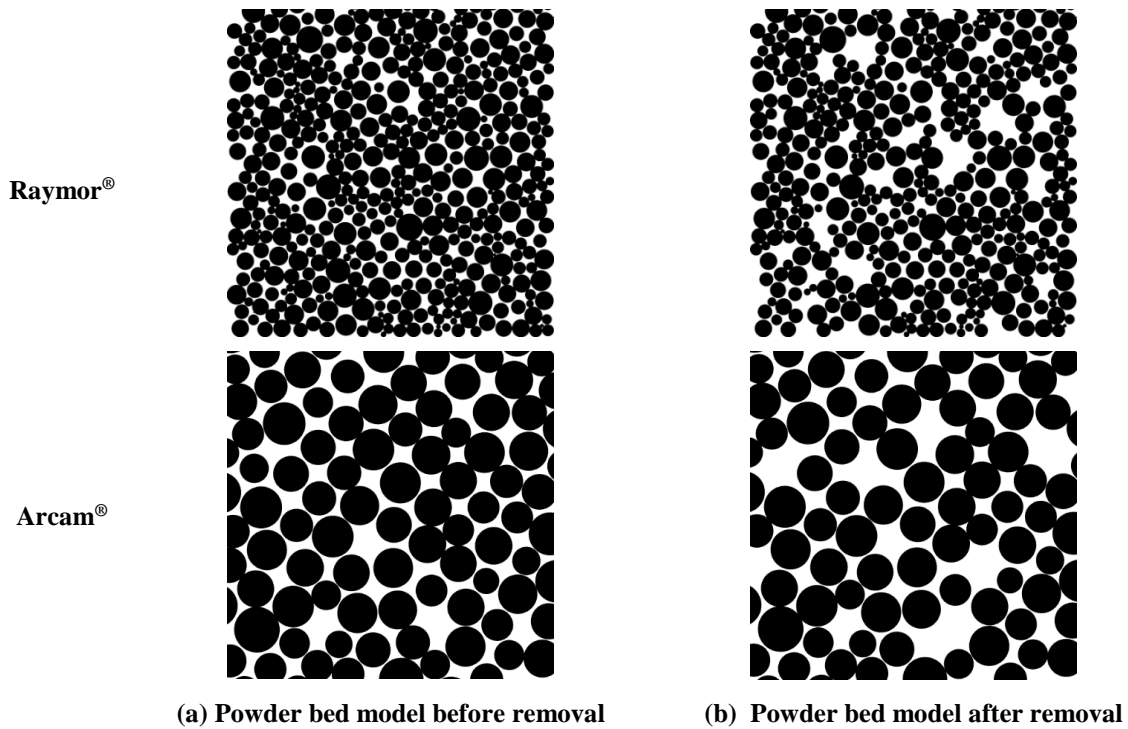


Figure 4-11 Powder bed model

4.2.2 Heat Transfer Analysis in Powder Bed

This section explains heat transfer analysis in a powder bed in order to derive assumptions for constructing deposition shape images. Diverse physical phenomena

govern the PBF processes [29, 35], as shown in Figure 4-12. Accordingly, formulating all the phenomena in a numerical simulation is computationally demanding and inaccessible. The process model has to be simplified based on dominant physical phenomena in order to make the simulation feasible. Since the thermal characteristics of powder bed are of interest in this research, only the heat transfer related phenomena are considered in the simulation model.

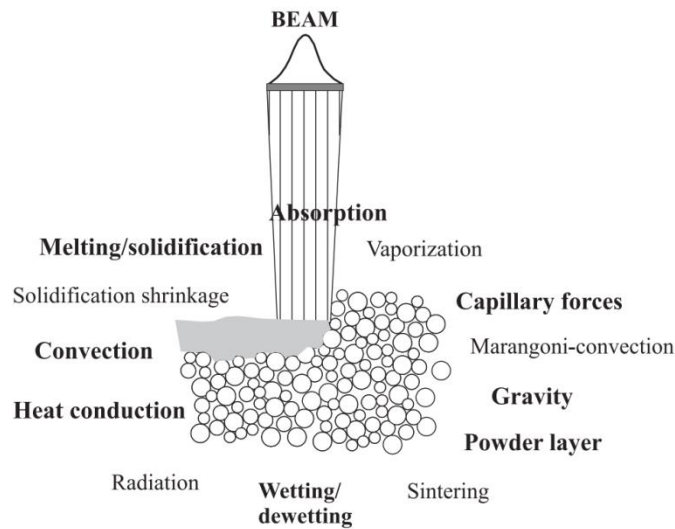
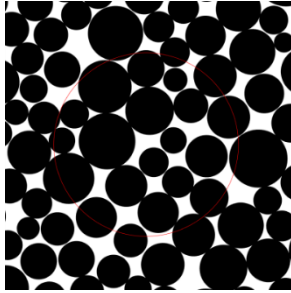


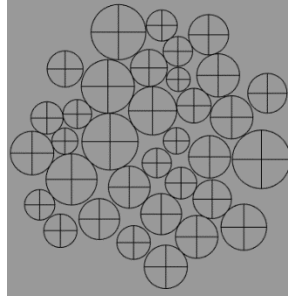
Figure 4-12 Physical phenomena during power bed fusion process [35]

The heat transfer model is developed based on heat conduction, energy absorption and the powder bed model obtained in the previous section. It is assumed that the convective heat transfer phenomenon is negligible, since a major portion of heat is transferred by conduction into the bed in the SLM process [81], and the EBM process is performed in a vacuum environment. In order to perform the analysis, a three-dimensional powder bed model is constructed by converting the two-dimensional powder bed model to spheres and placing the spheres on top of the previous layer. Figure 4-13

shows a two-dimensional powder bed model (a) and a corresponding three-dimensional powder bed model (b).



(a) 2D powder bed model



(b) 3D powder bed model

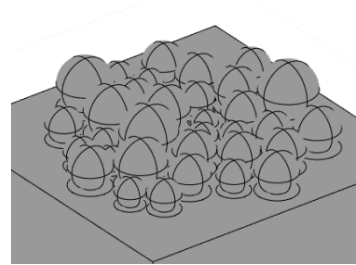


Figure 4-13 Powder bed model

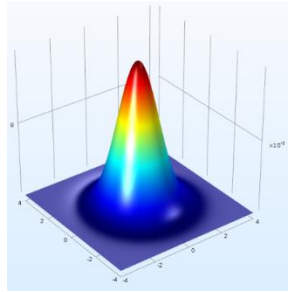


Figure 4-14 Beam energy profile

Next, the moving heat source that represents a laser or electron beam is modeled using a two-dimensional Gaussian distribution as following:

$$P(x, y, t) = \frac{P_0}{2\pi\sigma^2} e^{-\frac{1}{2\sigma^2}((x-x_c-v_x t)^2 + (y-y_c-v_y t)^2)} \quad (4.1)$$

where, P is the beam power density and P_0 is the total beam power. σ is the standard deviation, which affects the beam spot diameter. x_c and y_c are the current location of the

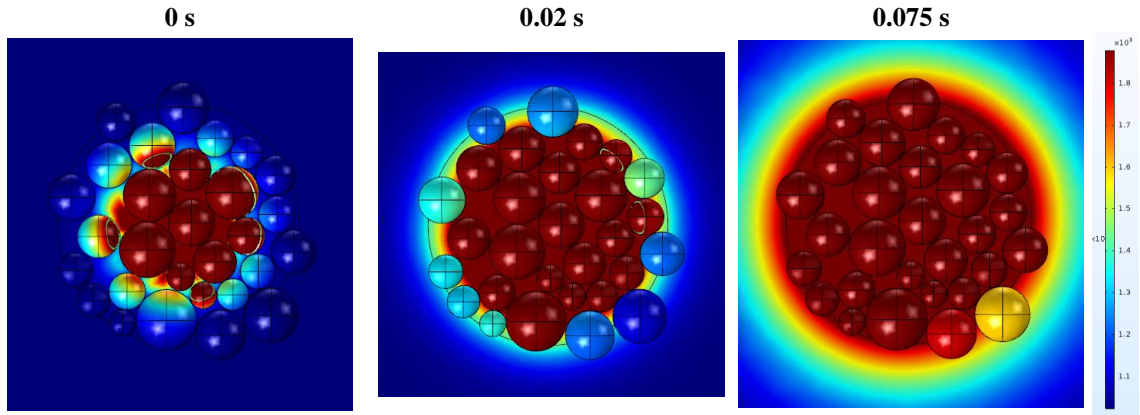
beam, respectively. v_x and v_y are the beam moving speed in the x and y directions, respectively. The distribution is represented in Figure 4-14. The power distribution is applied to the top surfaces of the powder particles and previous layers, where the beam directly exposes, as a heat flux boundary condition.

The previous layer below the particles is divided into two regions: an effective powder bed region and a solid region that was melted in the previous deposition process. The thermal conductivity of Ti-6Al-4V is applied to the powder particles and the melted region in the previous layer, while an effective thermal conductivity of Ti-6Al-4V powder is assigned to the effective powder bed region. The effective value is calculated using a scaling ratio, 0.602, which describes the reduction in thermal conductivity of powder due to voids among particles [82, 83].

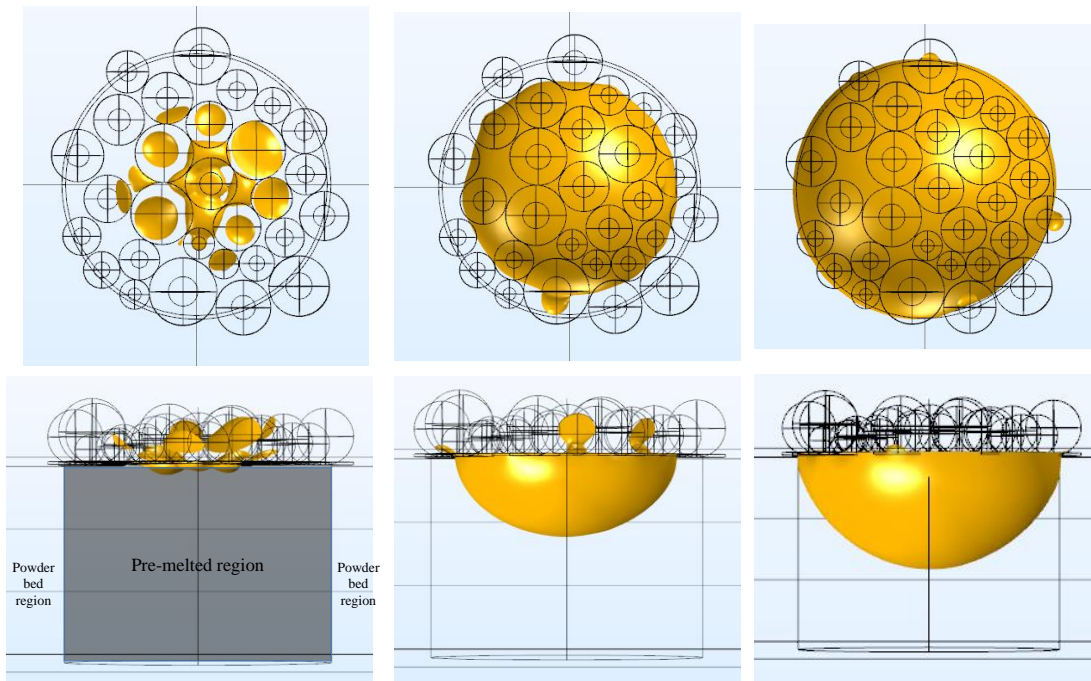
Based on the powder bed model, a time-transient heat transfer analysis is performed using commercial finite element software, COMSOL[®], in order to estimate the deposited shape around the area where a beam spot is exposed. The total beam power is set to 40W and the beam spot diameter is set to 0.3 mm. It is assumed that the beam is exposed for 0.002 seconds and the analysis is executed up to 0.001s.

The resulting temperature distribution and the isothermal surface of melting temperature are presented in Figure 4-15. From the result, two important points are observed. The first is that an isothermal surface is a circle-like shape on the top surface of a powder bed, as shown in Figure 4-15 (b). Thus, the melting pool shape around the beam spot can be assumed to be a circle, and the powders inside the circle are fully melted. The second is that the heat is mainly conducted through the pre-melted region, and the temperature outside the melting pool rapidly decreases. Based on this observation, it can

be assumed that the particles outside the melting pool keep their shape partially spherical below the melting temperature.



(a) Temperature distribution



(b) Isothermal surface at melting temperature

Figure 4-15 Result for heat transfer analysis

4.2.3 Considering Manufacturing Uncertainties

In the PBF process, two uncertainties are considered: the size of the powder particles and the amount of internal voids. The uncertainties in the size of particles are modeled using normal distributions as mentioned in Section 4.2.1. These uncertainties are integrated with the powder bed modeling procedure.

Next, the deposition image generation procedure takes variations in the amount of internal voids into account. It is reported that the typical percent porosity is in the range between 1% and 5% in SLM and EBM fabricated parts [12, 84]. In order to consider this variation, circles for the voids are added in a deposition shape image.

4.2.4 Generating Deposited Shape Image

Deposition shape images for the PBF process are generated based on several assumptions. Two assumptions can be made based on two observations in Section 4.2.2. The first assumption is that powder particles inside the melting pool are fully melted. The second assumption is that powder particles outside the melting pool keep their shape. These two assumptions are consistent with the fabricated shape as shown in Figure 4-17.

In addition, since the generated image is confined to small features, the deposition paths consist of only spots or they are tightly arranged as shown in Figure 4-16. Hence, it can be assumed that particles inside the cross sectional boundaries from slicing are fully melted with the first assumption. Moreover, it is expected that partially melted powder particles overlapping on the pool are stuck to the boundary, keeping their shape.

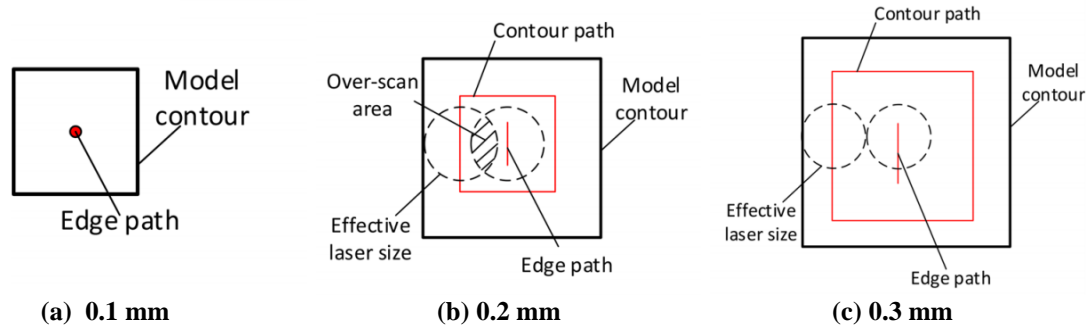


Figure 4-16 Scanning path analysis for small feature size with 0.1 mm beam spot [85]

Based on these assumptions, the deposited shape can be modeled using cross sectional boundaries and circles that present partially melted particles. The geometric model of cross sectional boundaries can be obtained from a slicing procedure in the same manner as mentioned in Section 4.1.2. Geometries of partially melted powder particles are modeled using circles in the powder bed, which have overlapping areas with the area inside cross sectional boundaries. The criterion to pick partially melted particles varies from process to process. In this research, 30% overlapping area is set, based on observation of fabricated cellular material.

Another geometrical model is required to include internal voids in a deposition shape image. The number of voids and their size is randomly selected based on the reported porosity variation, as mentioned in 4.2.3, and the location of voids is randomly determined inside the boundaries.

The geometrical model is converted into a pixel model using the same procedure presented in Section 4.1.4. The proposed method was applied to a strut model fabricated using the EBM process. The strut diameter was 0.35 mm and the Arcam[®] A2 EBM machine was used for fabricating the model with 0.3mm beam spot size. The resulting

image is compared with fabricated geometries in Figure 4-17. The method can describe particles stuck around strut boundaries.

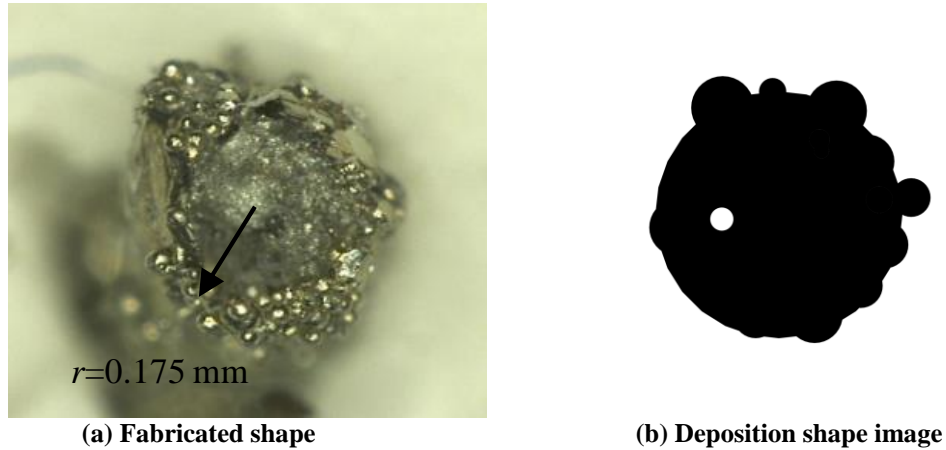


Figure 4-17 Shape comparison for PBF process

4.3 Implementation

This section presents several parametric studies to explain how to relate the DMP parameters to the LDP parameters. Two strut models, Model 1 in Figure 4-8 for the material extrusion process and the strut model in Figure 4-17 for the powder bed fusion process, are investigated. The selected LDP parameters are the area and dimensions of deposition geometries in this study.

4.3.1 Area of Deposited Geometries

The area of deposited geometries is calculated by multiplying the area of a pixel by the number of pixels identified as material in the images as following:

$$A = N_p \left(\frac{1}{R} \right)^2 \quad (4.2)$$

where, A is the area of deposited geometries. N_p and R are the number of pixels identified as material and the resolution of the image, respectively. In this study, the resolution is set to 440 pixels per centimeter (PPCM) for the ME process and 1000 PPCM for the PBF process based on the parametric study in Section 4.3.3.

Since manufacturing uncertainties are considered, the resulting area is a random variable. In order to obtain the distribution of the area, a hundred deposition shape images are generated for each model. For the material extrusion process, the mean value of area was 1.9027mm^2 , which is 11.2% larger than the area of design, and the standard deviation was 0.0586mm^2 . For the powder bed fusion process, the proposed process-modeling procedure gives 0.1072mm^2 for the mean area and 0.01175mm^2 for the standard deviation.

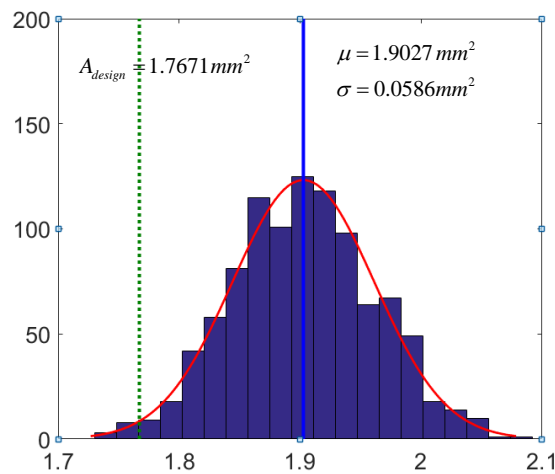


Figure 4-18 Distribution of the area for the ME process

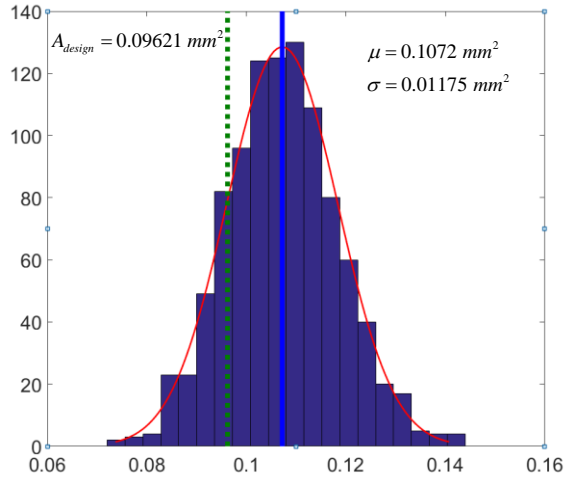


Figure 4-19 Distribution of the area for the PBF process

4.3.2 *Dimensions of Deposition Geometries*

Two geometrical parameters are studied for each process. The first is the diameter and the second is the positional error of the center location. The diameter was measured at 15 points along the perimeter of the deposition shape, and the coordinates of the center location were calculated as the average of the maximum and minimum coordinates in the x and y directions as shown in Figure 4-20. The resolution applied was the same as in the previous section.

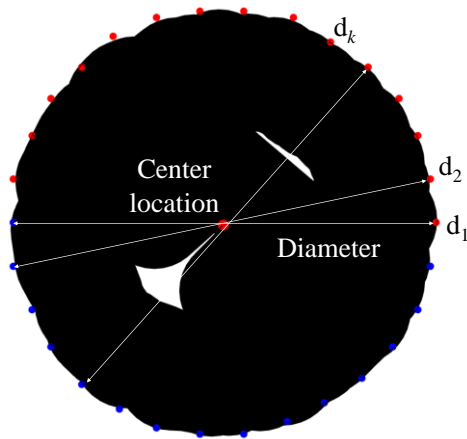
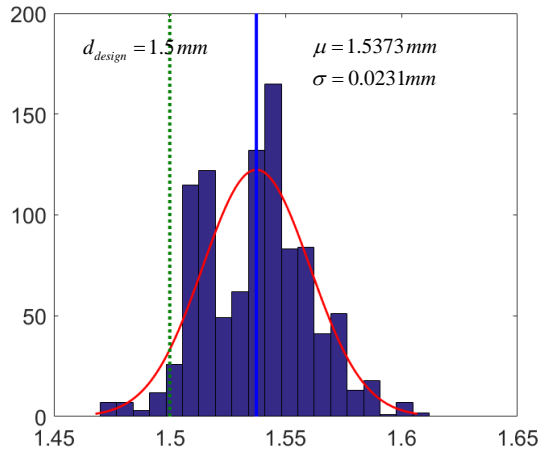
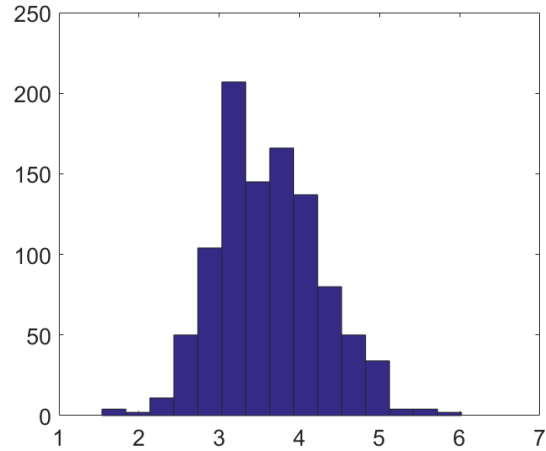


Figure 4-20 Calculation of Dimension

The results for the material extrusion process are shown in Figure 4-21, and the results for powder bed fusion process are represented in Figure 4-22.

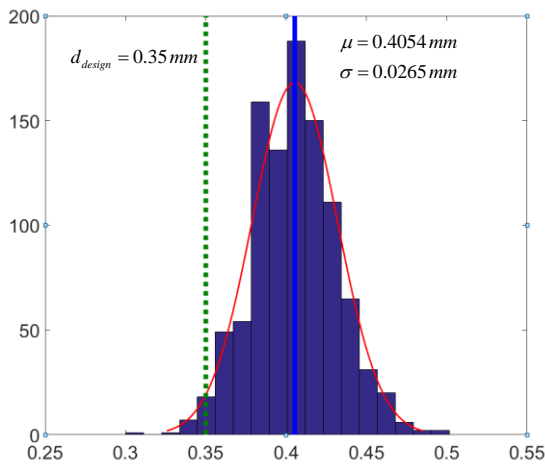


(a) Distribution of the diameter

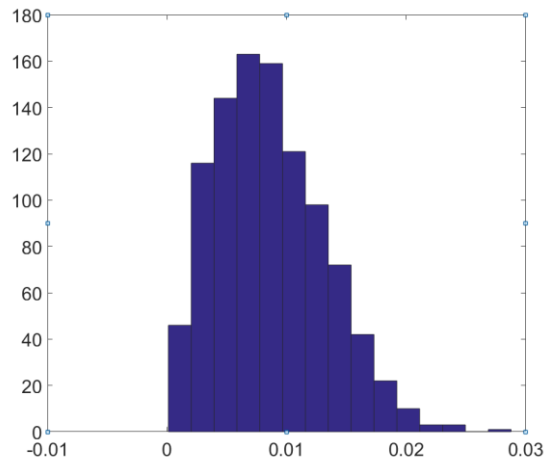


(c) Distribution of the center location

Figure 4-21 Distribution of geometrical dimension for the ME process



(a) Distribution of the diameter



(c) Distribution of the center location

Figure 4-22 Distribution of geometrical dimension for the PBF process

4.3.3 *Effects of Resolution*

In order to find the proper level of resolution, which leads to converged dimensional estimates of deposited geometries, the three parameters in the previous sections were calculated by varying the resolution from 40 PPCM to 400 PPCM for a material extrusion process and from 80 PPCM to 1600PPCM for an electron beam melting process.

Figure 4-23 and Figure 4-24 show the series of deposition shape images that have the same deposition paths and uncertainty distributions but that are generated using different resolution. Based on the deposition shape images, at least 320 PPCM for the material extrusion process and 1000 PPCM for the powder bed fusion process are required to express all geometrical features, including voids and gaps. The reason for the much finer resolution of the PBF process is that the strut diameter is typically smaller, and this research is confined to small struts as mentioned in Section 4.2.

In the convergence plots of Figure 4-25Figure 4-26Figure 4-27, the mean values of the geometrical parameters are converged at the level that is higher than 360 PPCM for the ME process and higher than 1000 CCPM for the PBF process. Thus, the values are implemented for measuring geometrical parameters in the previous sections.

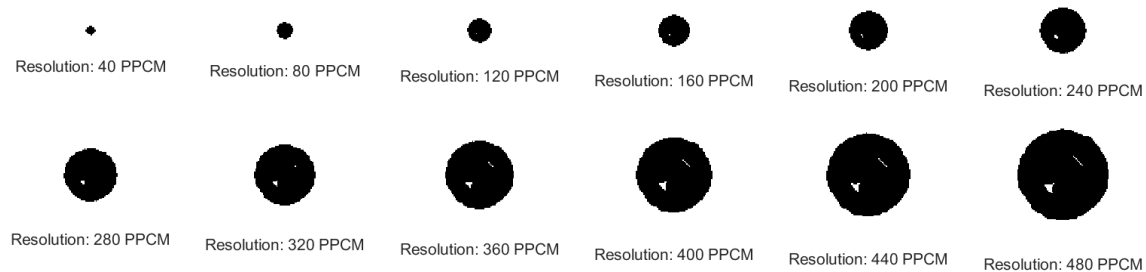


Figure 4-23 Deposition shape images for material extrusion process

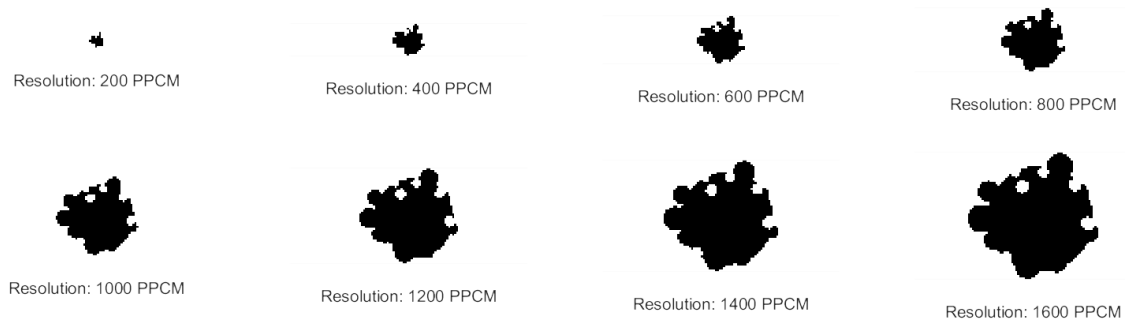
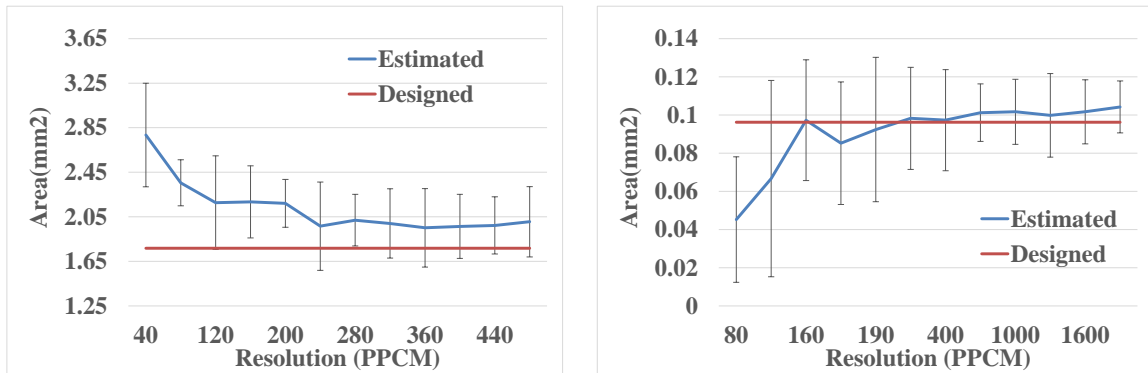


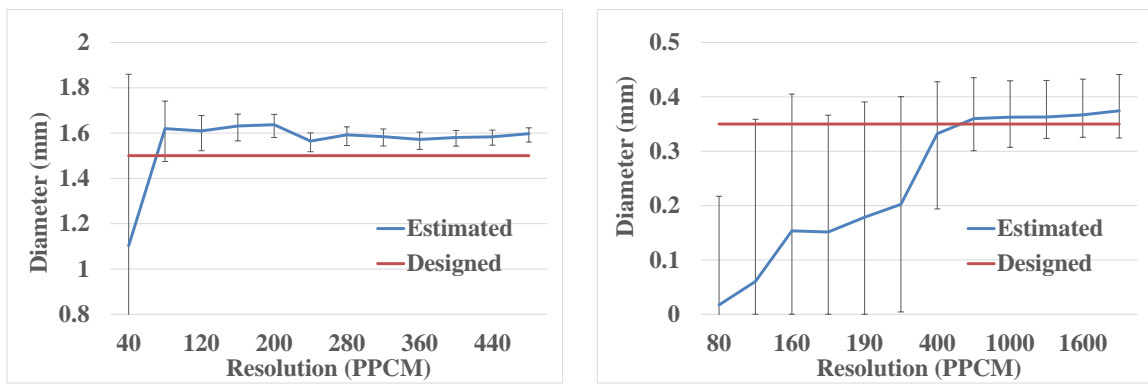
Figure 4-24 Deposition shape images for EBM process



(a) Material extrusion

(b) Electron beam melting

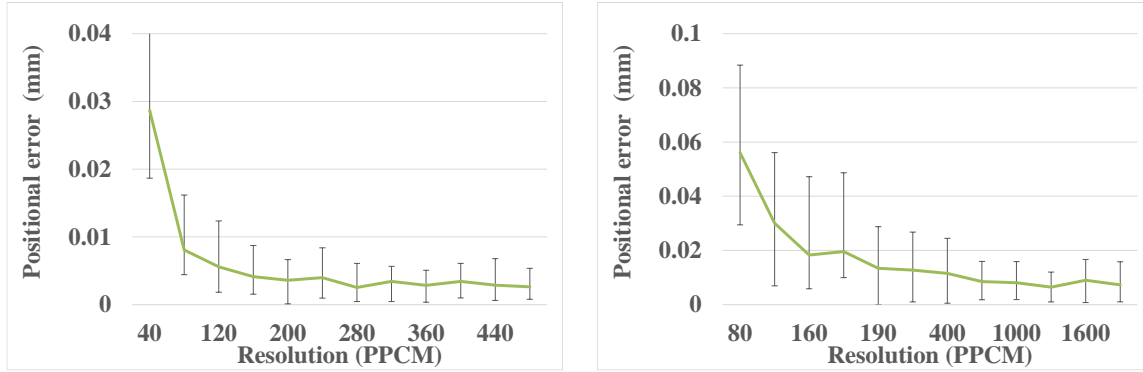
Figure 4-25 Effect of resolution on area



(a) Material extrusion

(b) Electron beam melting

Figure 4-26 Effect of resolution on strut diameter



(a) Material extrusion **(b) Electron beam melting**
Figure 4-27 Effect of resolution on positional error of center location

4.4 Chapter Summary

In this chapter, a procedure for deposition shape images is developed and is implemented to struts in cellular material. The proposed procedure incorporates the manufacturing instabilities arising in the AM process into the deposition shape image using the process-modeling scheme.

The results of implementation shows that the proposed process modeling method based on the deposition shape images can relate the DMP parameters and LDP parameters by providing probabilistic distribution of LDP parameters. Thus, the hypothesis of Research question 1 is validated. The deposition shape image will be utilized to develop an as-fabricated voxel model in Chapter 5.

CHAPTER 5 As-Fabricated Voxel Model

This chapter presents an as-fabricated voxel modeling procedure that constructs a voxel based geometry model based on the deposition shape images presented in the previous chapter. The goal of this chapter is to address a part of Research question 2. The as-fabricated voxel modeling approach aims to generate a numerical model whereby structural elements in a cellular material can assess geometric degradation quantitatively due to stair steps and internal defects, such as internal voids and gaps. Geometrical discontinuity, shown in voxel models, enables the proposed procedure to express the stair step phenomenon in additively fabricated parts.

The proposed approach was validated by comparing the numerical analysis results, obtained using the as-fabricated voxel models, with test results that were obtained using tensile specimens fabricated by the material extrusion process. The specimens were fabricated with varying build angles and corresponding as-fabricated voxel models were generated. Deterioration in mechanical properties, such as elastic modulus and yield strength, were assessed based on tensile tests and numerical studies of as-fabricated voxel models.

5.1 Voxel-based Modeling of Deposited Shape

An as-fabricated voxel model is constructed by mimicking the additive manufacturing procedure that deposits a raw material layer-by-layer. Fundamentally, the three dimensional shape of a deposited layer can be generated by extruding the deposited shape image along the building direction. However, details of the shape depend on the process characteristics. The voxel-based modeling procedure is shown in Figure 5-1. This

section explains the basic assumptions and a procedure for generating the three dimensional shape of a deposition layer in two AM processes.

5.1.1 Material Extrusion

This section explains the voxel modeling procedure for material extrusion. The procedure is represented in Figure 5-2. Fundamentally, a three-dimensional voxel model is constructed by extruding pixels in the building direction. In order to increase the geometrical accuracy of the model, the characteristics of the material extrusion are integrated into the procedure. Since the material extrusion uses thin filaments of a raw material, it is important to approximate a cross section of deposited filaments.

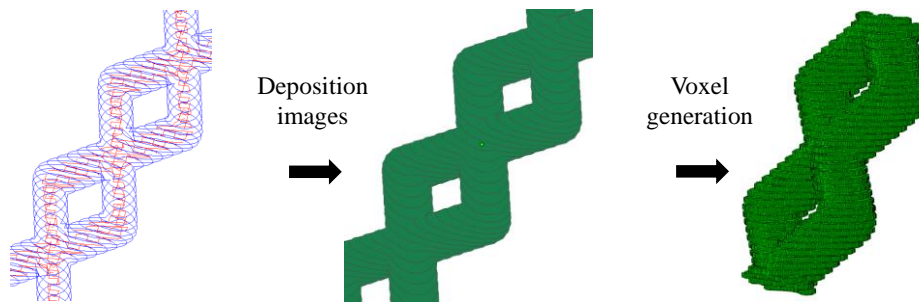


Figure 5-1 As-fabricated voxel model generation procedure

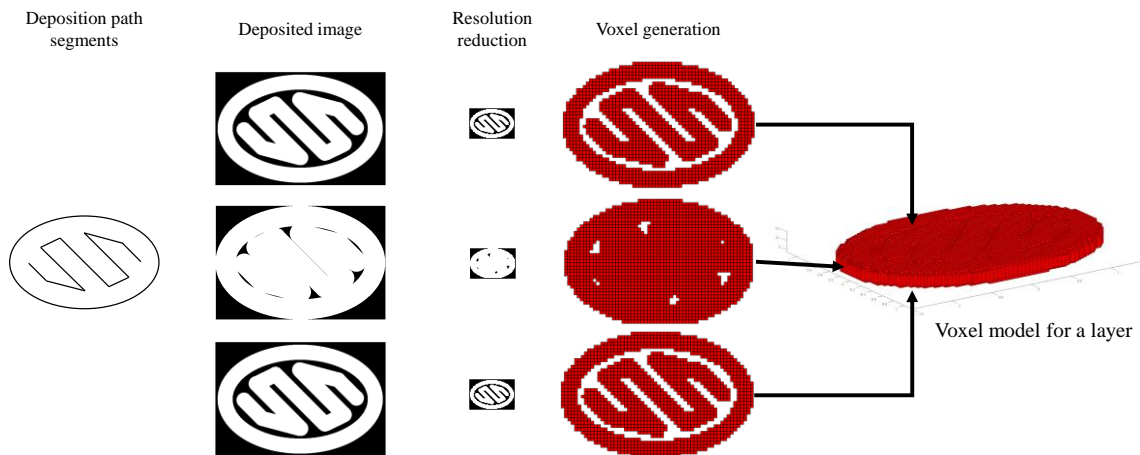


Figure 5-2 Voxel model generation for material extrusion process

The voxel model of the filament depends on its cross sectional shape. Three shapes have been proposed in previous research; (a) an ellipse [39, 86], (b) a rectangle [87], and (c) a mixed rectangle with ellipse corners [26] as shown in Figure 5-3. This research implements the mixed shape assumption, represented in Figure 5-3 (c), based on microscopic observation presented in Figure 5-4. The aspect ratio of the filament cross section is set to range from 1.75 to 2, as mentioned in the previous chapter. The size of the ellipse corners depends on the inter-filament coalescence phenomenon, which describes size reduction at the bounding surface of a deposited filament. The dimensions of the ellipse region are assumed to be a multiple of the layer thickness. In this research, size reduction ratios, b and c , are set to $1/6$ based on the literature [26].

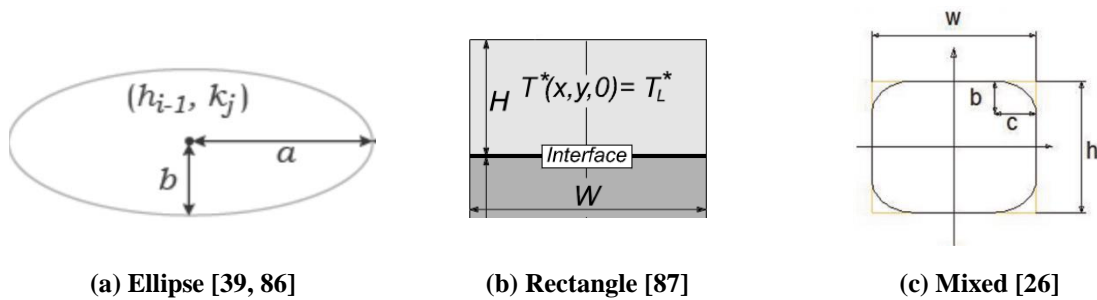
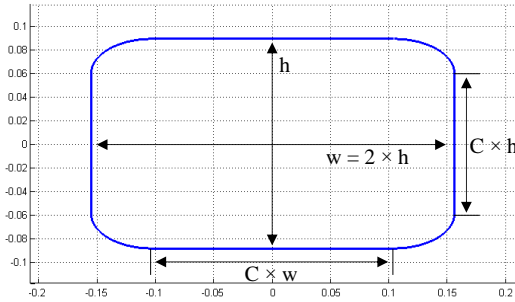


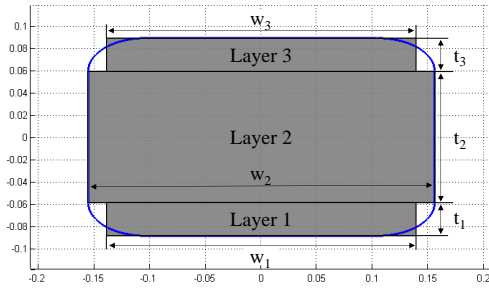
Figure 5-3 Cross sections in the literature



Figure 5-4 Cross section of deposited filaments



(a) Assumed cross-section of a filament



(b) Rectangle approximation

Figure 5-5 Assumption for filament cross section

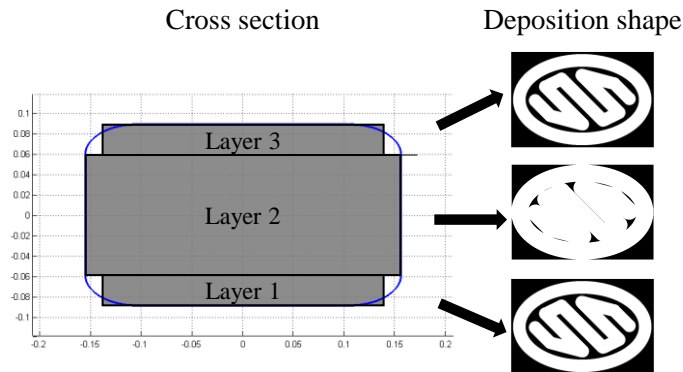


Figure 5-6 Deposition shape image for voxel layers

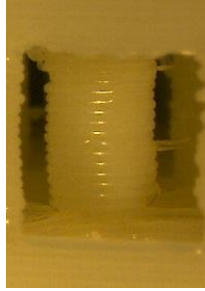
To model a filament using three-dimensional voxels, a cross section is approximated using three layers of rectangles in order to describe the edge regions in the cross section, as shown in Figure 5-5. The width and height at each rectangle are determined based on area equivalence so that the three rectangles yield the same area as the cross section. A voxel model of a filament consists of three voxel layers that represent three rectangles, as shown in Figure 5-5 (b). Since the deposition shape image in the previous chapter corresponds to the middle rectangle, two more deposition images are required at the top and bottom rectangles, as shown in Figure 5-6. The deposition shape

images can be generated by scaling the shape of the middle deposition image with the size reduction ratio. In detail, the widths of the rectangles and the diameters of the circles at each image are set to w_1 , w_2 and w_3 in Figure 5-5 (b), respectively.

Next, the resolution of the deposition shape images is reduced down to a target voxel resolution sufficient for representing filament geometries. As resolution increases, more details about the geometries can be captured, but more processing time and computational resources are required. Thus, the target resolution is compromised to maintain representation and reduce computational time. In this research, the target resolution for as-fabricated voxel models is set to 220 PPCM based on parametric studies concerning the computing time required to obtain a given resolution; these are presented in Section 5.2.1.

Finally, each pixel in the reduced resolution images is converted to a voxel by extruding the pixel along the build direction. The amount of sweep length at each voxel layer is set to the height of the rectangles, *i.e.* t_1 , t_2 and t_3 in Figure 5-5 (b). The resulting three layers of voxels are combined into one voxel model. After this step, a voxel model is obtained for one layer of the deposition path. This procedure is repeated for every deposition layer in order to construct a complete as-fabricated voxel model for a specimen.

The proposed method is applied to a strut in a cubic lattice structure. Figure 5-7 compares a fabricated strut with its as-fabricated voxel model. The comparison indicates that the voxel model can capture manufacturing instability on the surfaces of the fabricated strut.



(a) Fabricated strut



(b) As-fabricated voxel model

Figure 5-7 Comparison of a fabricated strut and its as-fabricated voxel model using ME

5.1.2 Powder Bed Fusion Process

This section presents the as-fabricated voxel modeling process for the powder bed fusion process. The fundamental modeling procedure to extrude pixels along the build direction is the same as the procedure proposed for the material extrusion process except for cross sectional approximation. Three assumptions made in the previous section can be represented using the approximation: (1) the melting pool is created inside the cross sectional boundaries, (2) the unmelted particles keep their spherical shape, and (3) internal voids are spherical.

To approximate the deposited shape in the powder bed, first unmelted particles and internal voids are randomly located along the build direction within the layer thickness. Particles larger than twice the layer thickness are removed in this step because they are crushed by the recoating blade. In order to describe the spherical shape of the unmelted particles and voids accurately, each layer is modeled using four cross sectional deposition shape images as shown in Figure 5-8. The heights of each of the layers are assumed to be the same. In all four deposition shape images, the cross sectional boundaries are identical, but the diameters of the circles for the particles and voids are varied depending on their locations along the build direction. The deposition shape image at each layer is generated

by scaling the circles for particles and voids in the deposition images, which are obtained in the previous chapter. After generating deposition shape images, the resolution of the images is reduced down to target voxel resolution. The target resolution is set to 850 PPCM based on the parametric study presented in the next section. Based on the deposition shape images, voxels are generated by extruding pixels at each layer by one fourth of the layer thickness, and the resulting voxels are combined into one voxel model of the deposition shape. This procedure is repeated for every deposition layer in order to construct a complete as-fabricated voxel model for a specimen. Figure 5-9 shows an as-fabricated voxel model for three layers, and Figure 5-10 compares a fabricated strut and the corresponding as-fabricated voxel model.

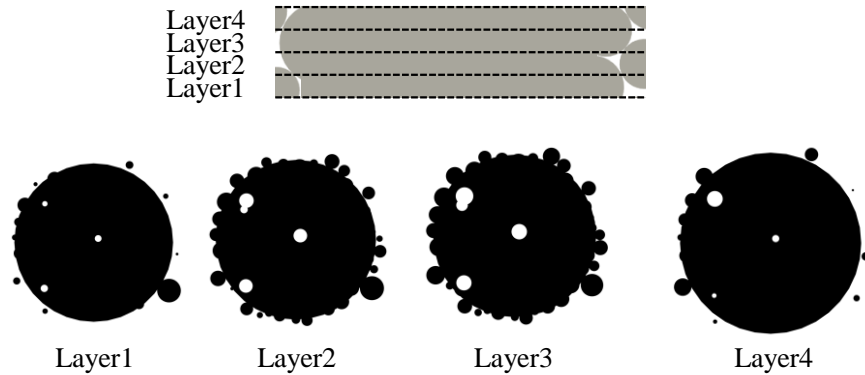


Figure 5-8 Layer deposition images at each layer

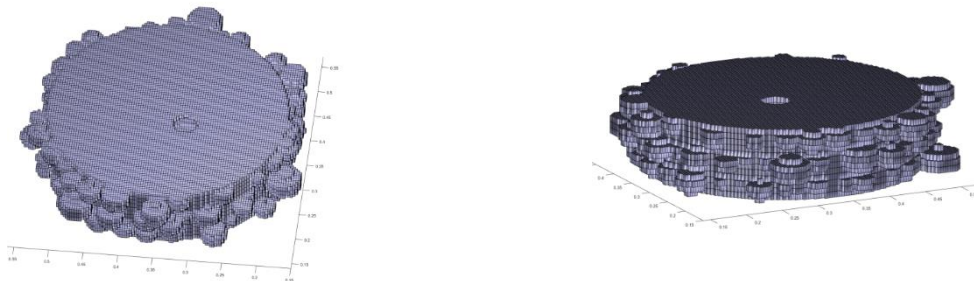


Figure 5-9 As-fabricated voxel model of three deposition layers using PBF process



(a) Fabricated struts using SLM



(b) As-fabricated voxel model

Figure 5-10 Comparison of a fabricated strut and its as-fabricated voxel model using SLM

5.2 Effect of Voxel Resolution

In the proposed voxel generation procedure, the resolution of the voxel models is an important parameter because it is related to the accuracy and efficiency of the procedure. This section presents a parametric study using three parameters to vary the resolution in order to select a resolution that requires fewer computing resources but maintains accuracy. The three parameters were selected for their utility in checking the required computational resources, for their effect on a geometrical parameter, and for their effect on a mechanical property, as follows: the number of degrees of freedom (DOFs) for required computational resources, the volume of an as-fabricated voxel model for a geometrical parameter, and the estimated stiffness for a mechanical property.

The model for this parametric study is a strut, with a 45° build angle, manufactured using the material extrusion process. Ten as-fabricated voxel models of the strut were generated, changing their resolution from 40 PPCM to 355 PPCM. The as-fabricated voxel models were exported to the commercial finite element software, ABAQUS[®], and

tensile tests were simulated using the models. Figure 5-11 shows the DOFs in the voxel models, volume, and estimated stiffness of the strut. The generated number of DOFs rapidly increases as the resolution is increased, as shown in Figure 5-11. This means that a higher resolution model demands more computing resources. A low resolution yields a coarse mesh in the resulting voxel model. In a coarse mesh, it is impossible to represent the details of an as-fabricated filament, but a coarse mesh requires fewer computing resources during the voxel generation step and numerical analysis. In contrast, a high-resolution enables a resulting voxel model to describe more details, but the required computing resources increase rapidly as resolution is increased.

In order to check the convergence of the geometrical and mechanical parameters, volume and estimated stiffness were calculated at each level of resolution. Figure 5-12 presents their convergence plots. The volume and estimated stiffness converged as resolution was increased, since the resulting geometry becomes more accurate at high resolution. In this research, the target resolution is set to 220 PPCM based the parametric study.

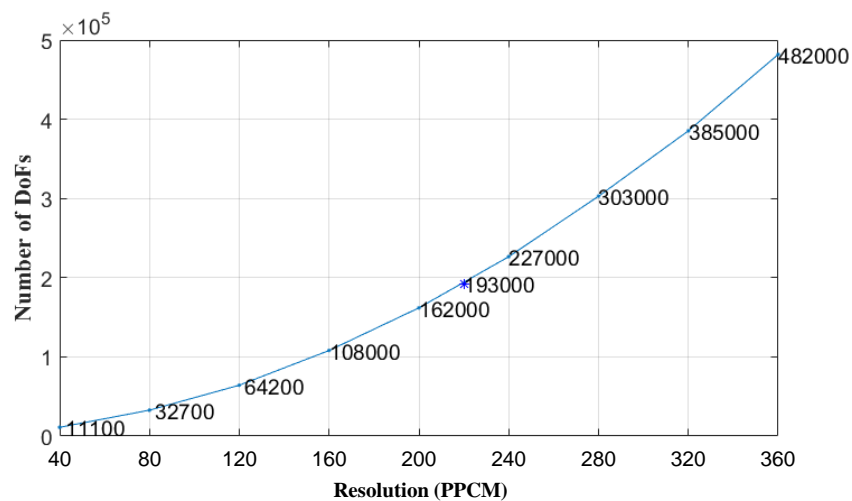


Figure 5-11 Change in the number of DOFs according to voxel resolution

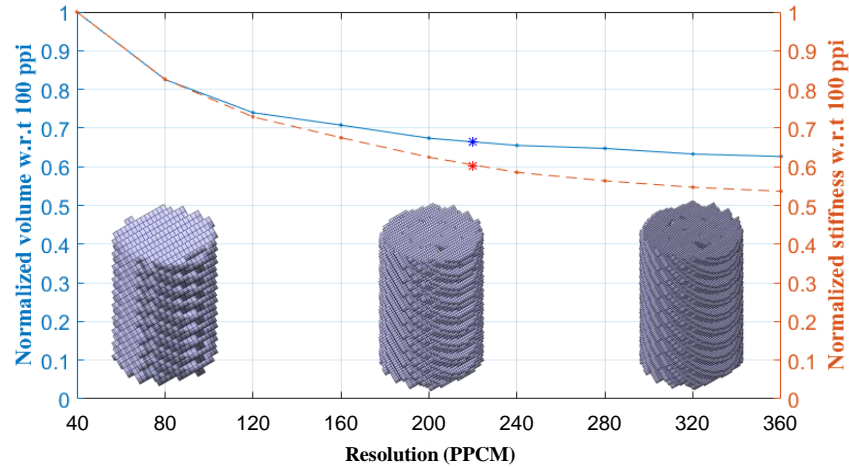


Figure 5-12 Change in volume and estimated stiffness according to voxel resolution

5.3 Validation of the As-fabricated Voxel Model

This section presents the validation of the as-fabricated voxel models. For validation, two mechanical properties of lattice specimens are estimated based on the finite element analysis using the as-fabricated model: elastic modulus and yield strength. The estimates are compared with test results of fabricated specimens using the material extrusion process. Based on the comparison, the AM process affects on the mechanical properties are explained using the as-fabricated voxel model.

5.3.1 Implementation of As-fabricated Voxel Modeling Approach

In order to validate the proposed as-fabricated voxel modeling procedure, the approach is applied to three types of tensile test specimens. The three designs are represented in Figure 5-13: (a) ASTM D638 type 4 standard specimens (Design 1), (b) specimens substituted by two bars with 2 mm diameter (Design 2), and (c) specimens substituted by diamond shaped lattice structures with 2 mm diameter (Design 3). Design

1 is intended for studying mechanical property degradation in bulky parts due to geometrical degradation, and Designs 2 and 3 are intended for investigating degradation in lattice structures. As-fabricated models of the specimens are generated at seven building angles: 0°, 15°, 30°, 45°, 60°, 75°, and 90° as shown in Figure 5-14. Since the resulting as-fabricated voxel models consist of a huge number of voxels, extensive computing time and resources are required. To relieve this, only the gage regions in the specimens are modeled. The resulting as-fabricated voxel models are shown in Figure 5-15. The cross sections of the fabricated specimens are shown for comparison purposes along with cross sections of the as-fabricated models.

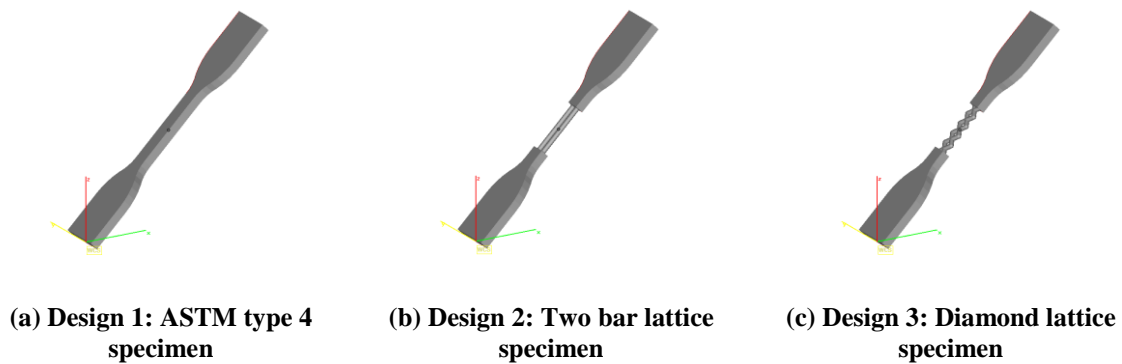


Figure 5-13 Specimen designs

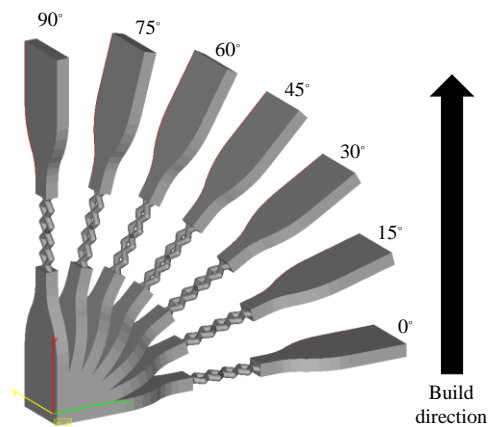


Figure 5-14 Build angles

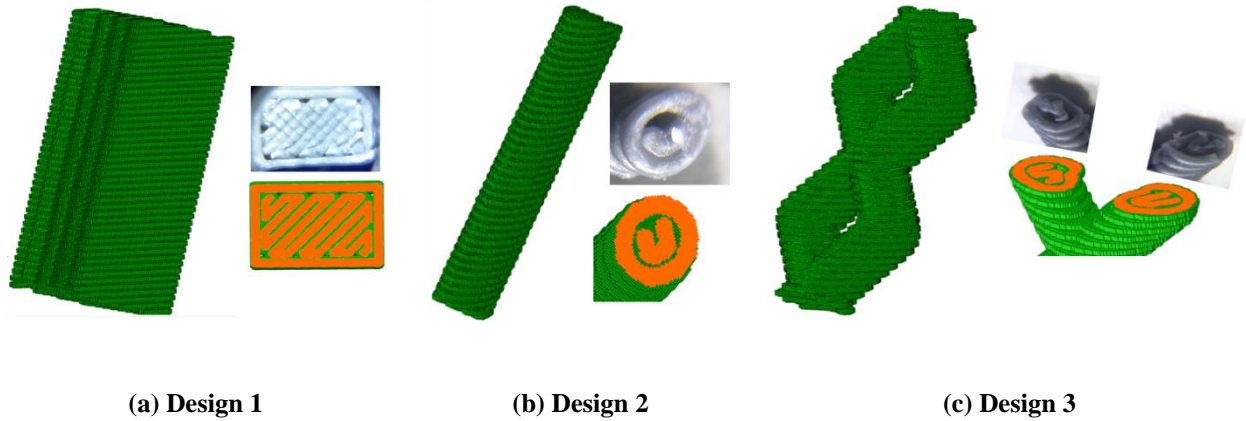


Figure 5-15 Resulting as-fabricated voxel models for specimens

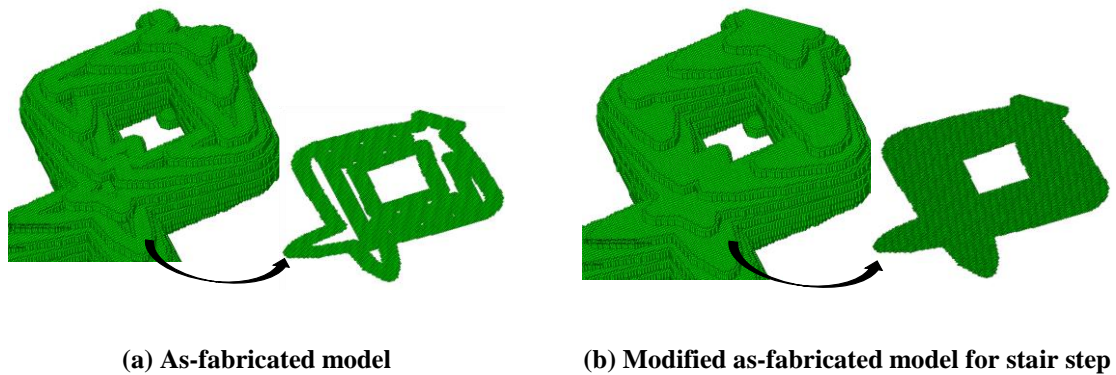


Figure 5-16 Modified as-fabricated model

In addition to the as-fabricated models with stair steps and deposition path, a set of modified as-fabricated models are generated with the assumption of perfectly dense infill in order to consider only the stair step effect. In the modified models, it is assumed that the regions inside the contour paths are fully filled with material, with no air gaps or voids. The modified models do not include any information about deposition paths, except for contours; therefore, there are no internal voids and air gaps. To build a modified voxel model, the step to compute the deposited images in Figure 5-2 is modified by substituting the void color (black) into the material color (white) inside the contours. Figure 5-16 compares two as-fabricated voxel models, where the modified

model, with solid cross-section layers, is easy to distinguish in Figure 5-16 (b) from the as-fabricated model in Figure 5-16 (a).

5.3.2 Numerical Analysis using As-fabricated Voxel Models

Obtained as-fabricated voxel models were exported to the commercial finite element analysis software, ABAQUS[®], with displacement boundary conditions that mimic a tensile test. The fixed boundary condition was applied to one end, and a forced displacement boundary condition was exerted on the other end. A nonlinear material model was applied based on an elastic-perfectly plastic material model. The elastic modulus and yield strength were set for ABS-P400, following guidelines from Stratasys, as 1627 MPa and 22 MPa, respectively. The elastic modulus and ultimate tensile strength (UTS) of the specimens were estimated based on the resulting displacement-reaction force relation from the analysis.

Reference mechanical properties are required for the study of property degradation. The reference properties of the specimens were obtained analytically by applying structural mechanics theories for specimens of Designs 1 and 2. However, this was impossible for Design 3 specimens, as the struts were short but the joints were relatively large compared to strut length, both of which made it difficult to apply structural mechanics theories. Thus, the reference mechanical properties were calculated based on finite element analysis using the three models that do not have any geometrical defects, as shown in Figure 5-17, with symmetric boundary conditions. The reference mechanical properties are listed in Table 5-1.

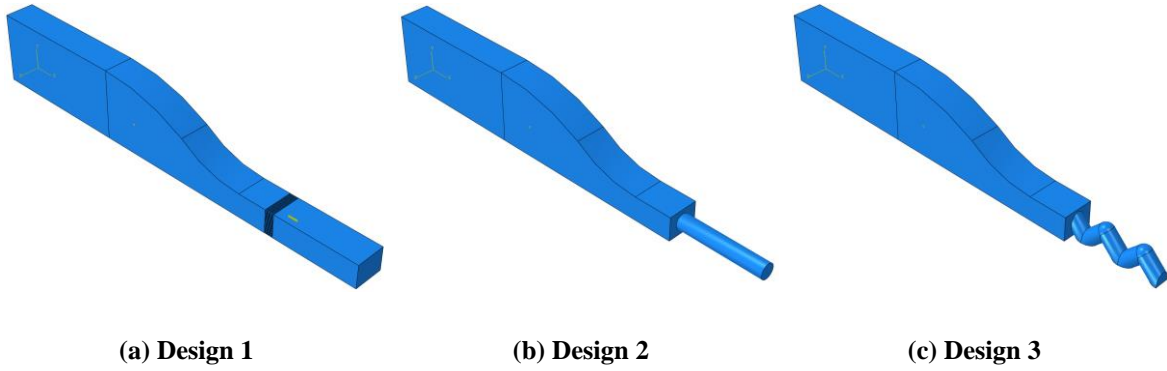


Figure 5-17 Reference models for calculating mechanical properties

Table 5-1 Mechanical properties from reference models

	Elastic modulus (MPa)	Ultimate tensile strength (MPa)
Design 1	1627	22
Design 2	396.18	5.36
Design 3	236.73	2.39

5.3.3 Experimental Result

The specimens were fabricated using a Stratasys Dimension 1200es machine for tensile tests to evaluate mechanical properties. A T16 nozzle tip, which yields a 0.254mm layer thickness, was used, and the extrusion temperature and speed were set to 300°C and 8.89 cm/s, respectively. For each design and building angle, at least three specimens were built. Figure 5-18 shows the fabricated specimens on a build plate. It is noteworthy that those lattice structure regions built at over 60° build angles were surrounded by the support material. The material was later dissolved in the acid solution bath per standard post-processing procedures. Three fabricated specimens at each build angle were tested using an Instron testing machine, following the ASTM D638 standard. The test speed was 5 mm/min.

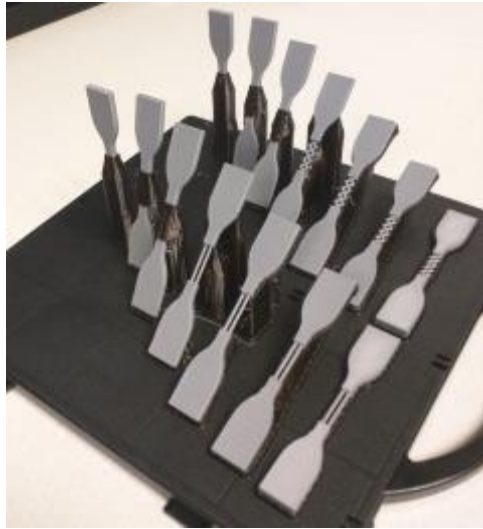
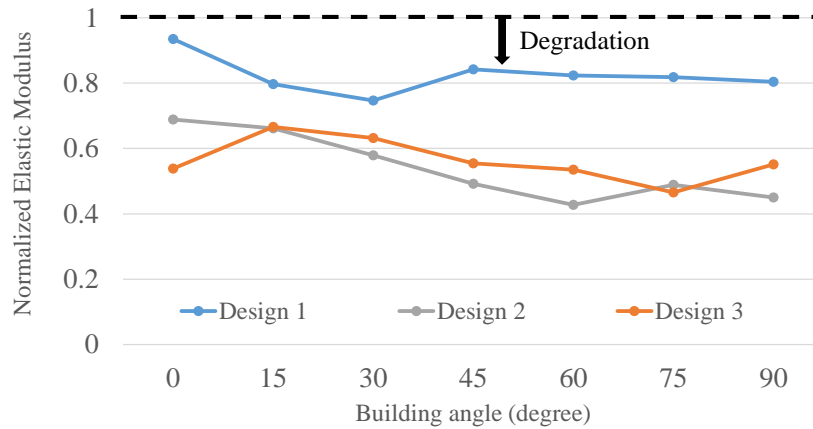
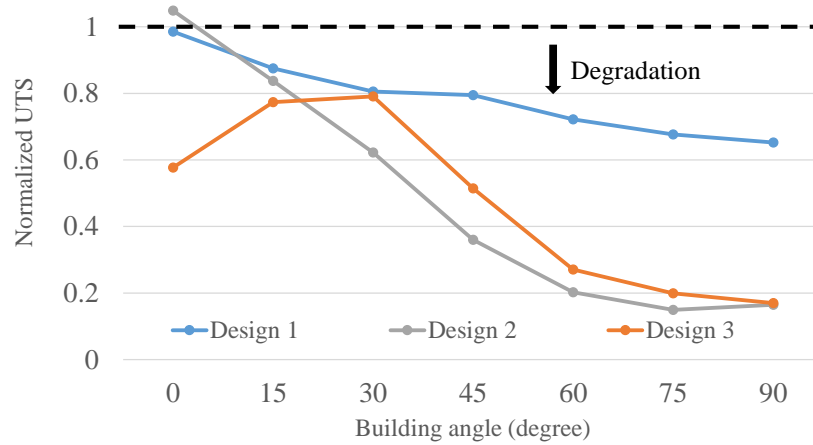


Figure 5-18 Fabricated specimens on the build plate

The mean values of the normalized mechanical properties with respect to reference values are shown in Figure 5-19. Table 5-2 lists the percent degradation compared to the reference properties. In all specimens, the resulting mechanical properties were lower than the reference values. The results show that the AM process lowers mechanical properties up to 55.0% for elastic modulus and 85.1% for ultimate tensile strength. The process affects the mechanical properties of the lattice structure specimens (Designs 2 and 3) more than standard specimens (Design 1). The results mentioned above demonstrate that a material extrusion AM process has impacts that are more critical on a lattice structure than on a bulky part.



(a) Normalized elastic modulus



(b) Normalized ultimate tensile strength

Figure 5-19 Comparison of normalized mechanical properties from tensile tests

Table 5-2 Property degradation from test

Build angle	0°	15°	30°	45°	60°	75°	90°	Average	
Design 1	Elastic modulus	-6.5%	-20.3%	-25.3%	-15.8%	-17.7%	-18.2%	-19.6%	-17.6%
	UTS	-1.5%	-12.5%	-19.5%	-20.5%	-27.8%	-32.4%	-34.7%	-21.3%
Design 2	Elastic modulus	-31.2%	-33.9%	-42.1%	-50.8%	-57.2%	-51.2%	-55.0%	-45.9%
	UTS	-0.3%	-21.4%	-22.7%	-60.0%	-78.0%	-85.1%	-83.6%	-50.2%
Design 3	Elastic modulus	-46.2%	-33.4%	-36.8%	-44.5%	-46.5%	-53.4%	-44.9%	-43.7%
	UTS	-42.3%	-22.6%	-20.9%	-48.6%	-73.0%	-80.1%	-83.0%	-52.9%

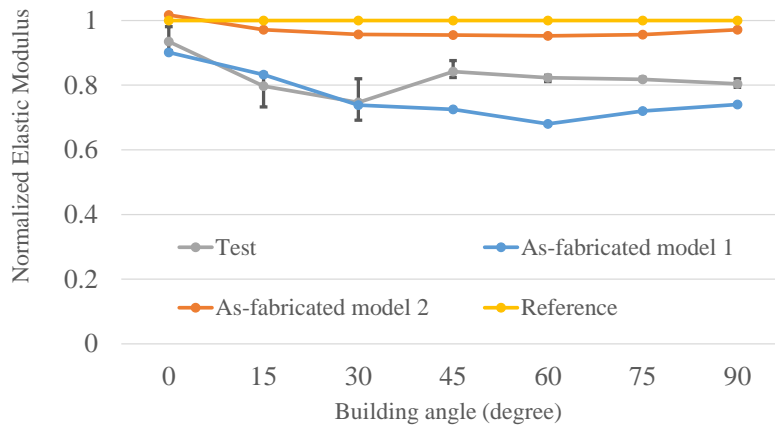
Furthermore, the AM process effect becomes more significant as the build angle is increased. Based on observation of specimens, the building direction is perpendicular to the direction of force induced in tensile tests at the 0° build angle, but the direction is aligned to the force direction at the 90° build angle. This means that the interfaces between layers are more exposed to force as the build angle increases. Thus, it can be inferred that lower bonding force between layers in the material extrusion AM process affects mechanical properties, and this is more obvious in lattice structures.

5.3.4 Quantification of AM Process Effect

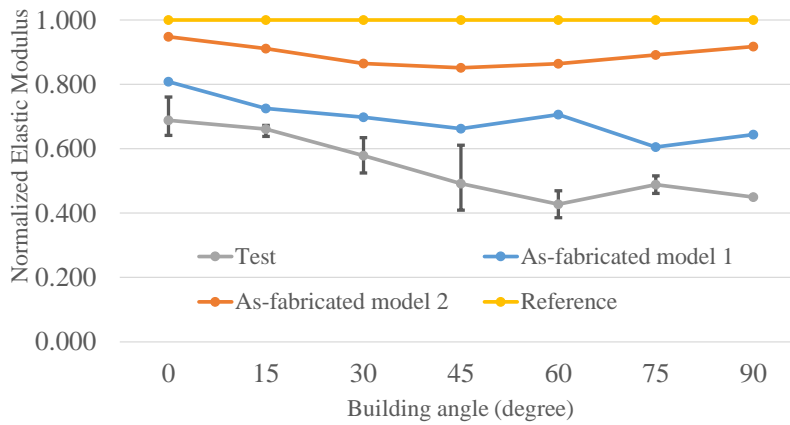
This section compares the test results with the simulation results in order to validate the as-fabricated voxel model. To investigate the utility of the as-fabricated voxel model, three simulation results are compared with the test result: (1) reference models without considering AM effects, (2) as-fabricated voxel models with stair step and deposition path effects (denoted by as-fabricated models 1), and as-fabricated voxel models with only the stair step effect (denoted by as-fabricated models 2). In addition, this section explains how the AM process effects on mechanical properties are quantified based on the as-fabricated voxel model.

5.3.4.1 Elastic Modulus

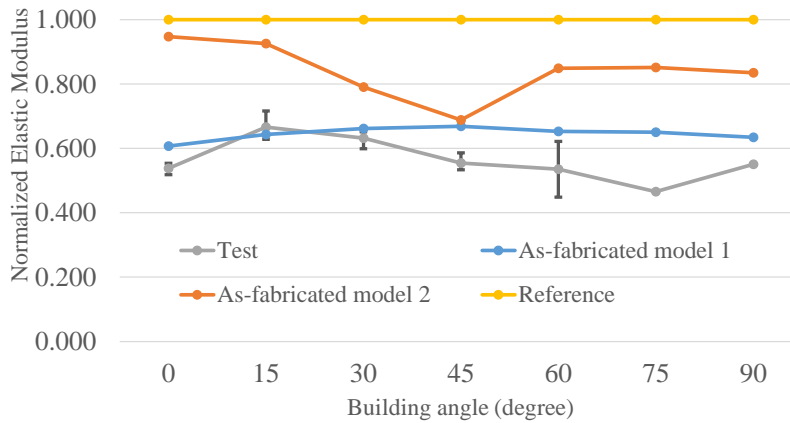
The normalized elastic modulus results with respect to reference values are shown in Figure 5-20. The test results are represented with minimum and maximum values of the specimens. The blue lines are obtained using as-fabricated voxel models 1. The orange lines are generated using as-fabricated voxel models 2.



(a) Design 1



(b) Design 2



(c) Design 3

Figure 5-20 Comparison: Elastic modulus

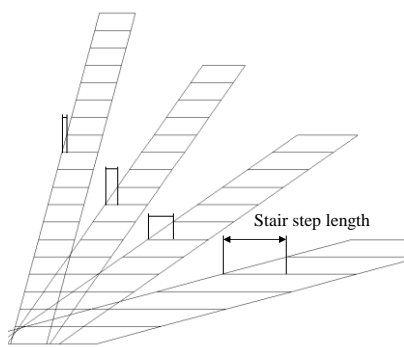
Table 5-3 Volume difference between Models 1 and 2 for Designs 2 and 3

Build angle	0°	15°	30°	45°	60°	75°	90°
Design 2	9.45%	4.80%	0.64%	0.66%	2.31%	19.88%	19.53%
Design 3	16.53%	7.67%	3.60%	1.06%	0.48%	0.46%	0.85%

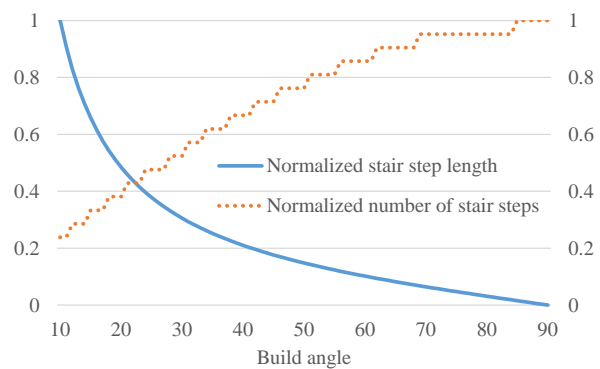
In all three designs, the as-fabricated voxel models 1 predict elastic modulus more accurately than other estimates. This is because the internal airgaps and voids, as well as the stair steps, are modeled in the approach. It is noteworthy that the as-fabricated voxel models 2 can consider only a small portion of the degradation in elastic modulus, since they do not allow for internal defects. In addition, the property degradation depends on not only the amount of material used but also the deposition pattern, which affects the amount of bonding area between layers. Since deposition paths alter the bonding area between layers, the pattern has additional impacts on mechanical properties in addition to impacts from volume reduction. Table 5-3 presents volume reduction between as-fabricated models 1 and 2 for designs 2 and 3. The volume reduction does not show the same trend as the amount of property reduction. The convergence plots shown in Figure 5-12 also support the effect of deposition paths on the property degradation. If mechanical properties were affected by only the amount of missing material, the volume and stiffness convergence plots would be similar, but the plots show that more property degradation occurred as resolution increased. This means that more information on

deposition paths at higher resolution enables to consider more degradation sources, and as a result, more property reduction occurs.

There are two points to investigate based on the results. Firstly, it is concluded that the stair step effect becomes more important in lattice structures than in bulky parts. In Design 1, the moduli evaluated using the modified as-fabricated voxel models were 6% lower than those obtained using the reference models. However, the degradation in lattice structure specimens (Designs 2 and 3) was larger; property reduction was up to 35% less than the reference, depending upon the build angle. Secondly, stair steps had the greatest impact on property degradation at the 45° build angle, based on the results from as-fabricated model 2, where estimates of elastic moduli were at a minimum. These results matched well with the fabricated geometries. The process-induced stair steps vanished at the 0° and 90° build angles in the fabricated specimens and therefore, the impact of stair steps is minimized. In between these two angles, as the build angle increased, the number of stair steps, which is the same as the number of the layers, also increased, but the length of the stair steps became shorter, as illustrated in Figure 5-21 (a) and (b).



(a) Stair step length

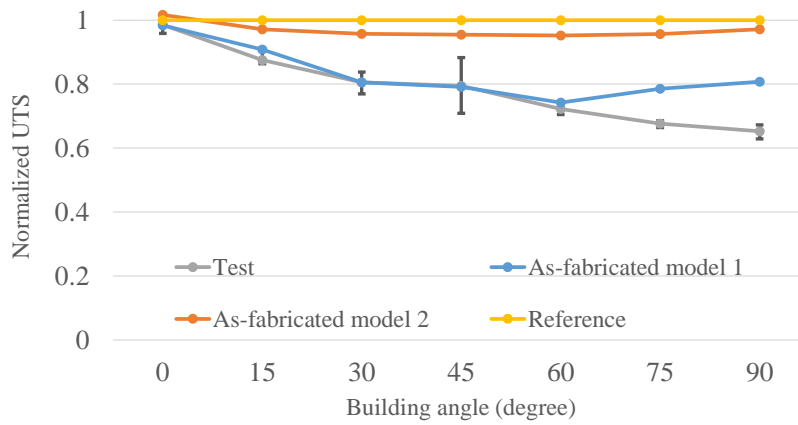


(b) Normalized stair step length and number

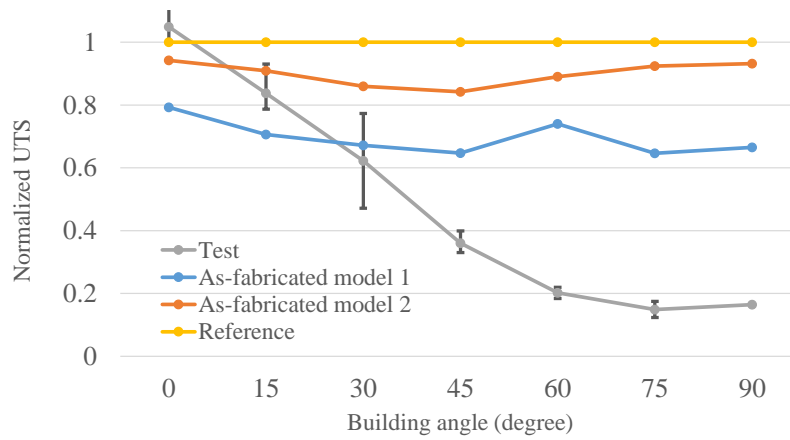
Figure 5-21 Change of stair steps according to build angle

5.3.4.2 Yield Strength

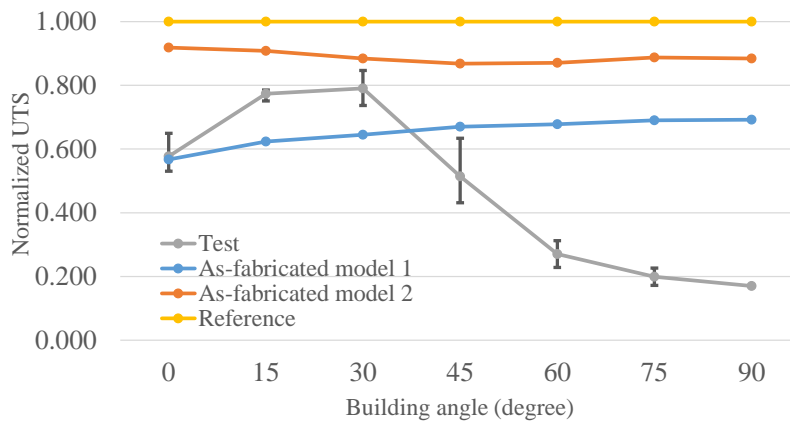
The estimated ultimate tensile strength results from the as-fabricated voxel models are shown along with test results in Figure 5-22, as a function of build angle. For Design 1, the estimates using the as-fabricated voxel modeling approach follow test results up to the 60° build angle but show errors at greater than 60° build angles. Although the proposed approach can represent geometrical degradation, the results show large error. This is because non-geometrical defects affect the yield strength of specimens. One possible reason for this is the lower bonding force at the interfaces between layers, the effects of which are not modeled well in the proposed approach. In low angle specimens, failure occurred perpendicularly to the deposited direction, but high build angle specimens are broken along the interface between deposited filaments, as shown in Figure 5-23. The bonding force between filaments is generally lower than the yielding or breaking force of a filament. This leads to lower tensile strength in high angle specimens. Thus, the interface characteristics, which are not modeled in the proposed method, induce additional degradation in ultimate tensile strength. In addition, since the lower bonding force limits the force at failure, interface characteristics have more impact on ultimate strength than does elastic modulus. In Designs 2 and 3, failure patterns were similar to those of Design 1 specimens but failure was initiated in joint regions. The estimates using as-fabricated models gave significant errors, although they were closer than other estimates. Based on the comparison between Design 1 and Designs 2 and 3, it can be concluded that the effects of interfaces have an impact that is more significant on lattice structures than on bulky parts.



(a) Design 1



(b) Design 2



(c) Design 3

Figure 5-22 Comparison: Ultimate tensile strength

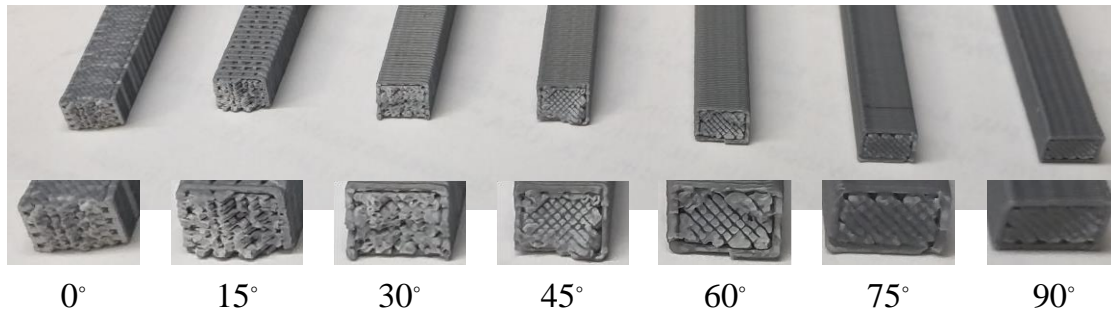


Figure 5-23 Fracture section of Design 1 specimens at each build angle

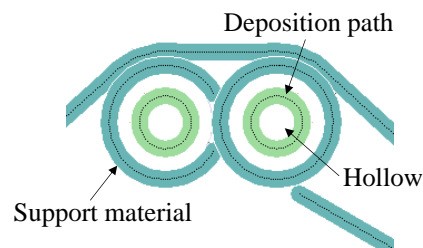


Figure 5-24 Deposition path for lattice region in Design 2 specimen at 75° build angle

Furthermore, errors are larger at high building angles for lattice specimens. Another possibility for larger errors at high build angles is the effect of the support material in material extrusion AM. The presented approach does not account for the effects of the support material during fabrication or during post-processing when a solvent is used to dissolve support material. As mentioned in Section 4.2, lattice parts in specimens fabricated at greater the 60° build angles are built surrounded by support material. Moreover, there is no infill raster deposition at high building angles (75° and 90°), as shown in Figure 5-24 since the area inside the contour deposition path is too small to accommodate infill deposits, and as a result, the fabricated struts are hollow. Therefore, the support materials can more easily disturb the fabricated dimensions at high building angles than low building angles by pushing structural materials inward due to fabrication

conditions, such as vibration, tip positioning tolerance and leaving debris between layers. This leads to additional property degradation in high build angle specimens.

5.4 Chapter Summary

In this chapter, the as-fabricated voxel modeling approach was proposed and validated with test results. In Section 5.1, the modeling procedure for constructing as-fabricated voxel models in the material extrusion and the powder bed fusion process was explained. The deposition shape images explained in Chapter 5 were extruded along the build direction in order to generate voxels. In the material extrusion process, the voxel generation process is performed based on the assumption for cross sectional shape of deposited filaments. The cross sectional shape is assumed as an edge blended rectangle with ellipses. In the powder bed fusion process, the generation procedure is conducted to capture powder particle stuck on the melting pool.

In section 5.2, the effects of the voxel resolution on geometrical accuracy, mechanical properties and computational resources were investigated to find the optimal resolution. The target resolution was set to 220 PPCM based on the parametric studies.

In Section 5.3, the proposed as-fabricated voxel model scheme was validated by comparing analysis results using as-fabricated voxel models with test results for the material extrusion process. The validation results showed that the as-fabricated voxel model could describe degradation in the elastic modulus. In contrast, the validation results for the yield strength implies that the voxel model has a limitation that it cannot capture the drastic strength reduction of material extrusion lattice structures fabricated at

high build angles over 45°. However, the trend of property degradation is match with tests.

Based on the validation results, a part of Research question 2 can be answered in the aspect of the modeling methodology: the as-fabricated voxel modeling can describes the propagation of geometrical and material variations in the layer deposition parameters to the structural element parameters. The other part regarding the quantification method will be addressed in Chapter 6, based on the analysis of the as-fabricated voxel models.

CHAPTER 6 Determination of Structural Element Parameters

This chapter presents how to determine the structural element parameters using an as-fabricated voxel model that integrates the design and process parameters and the layer deposition parameters. The goal of this chapter is to answer the remaining part of the second research question. To explain the mechanical characteristics of cellular materials more efficiently and accurately, the presented method investigates the effects of a joint region as well as common consideration in the literature, such as dimensions of struts and representative unit cells. In order to assess the effects of a joint region, a new finite element, a semi-rigid jointed frame element, is proposed and formulated. Parametric studies are performed to examine the effect of layer deposition parameters as well as design and process parameters.

6.1 Structural Element Parameters

The mechanical performances of a cellular material depend on mechanical characteristics of basic features such as struts and walls. To construct a numerical model for estimating the mechanical performance of a cellular material, the features are modeled using structural elements such as frame and plate elements. In this research, the structural element parameters are defined as the geometrical and material parameters of the basic features, which affect mechanical performance of a cellular material. This research focuses on lattice structures, which are composed of struts.

A strut in a lattice structure is divided into two regions, frame and joint regions, as shown in Figure 6-1. To model the frame region, two geometrical parameters, diameter

and length, and a material parameter, elastic modulus, are required. The structural element parameters such as cross sectional area and the second moment of area are derived. For the joint region, two parameters are defined: fixity and eccentricity factors. The fixity factor defines the stiffness of a joint, and the eccentricity factor is related to the size of the joint. The structural elements adopted in this research are listed in Table 6-1.

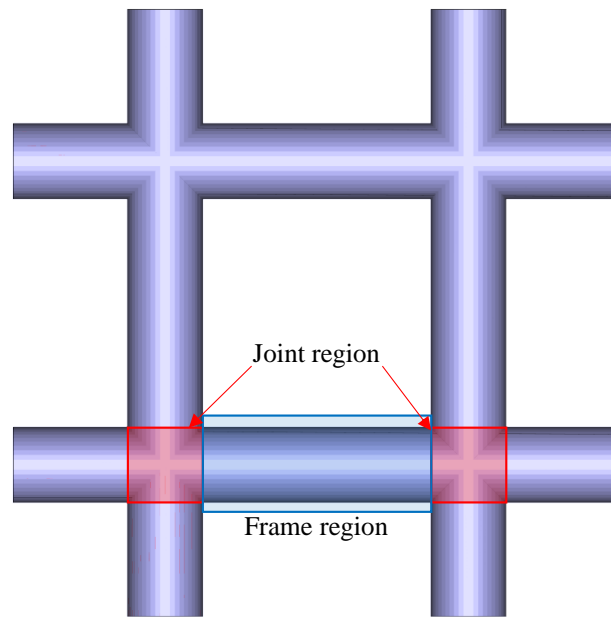


Figure 6-1 Two regions of a strut in a lattice structure

Table 6-1 Structural element parameters

Region	Parameters	Symbol
Frame	Strut diameter	d
	Strut length	L
	Cross sectional area	A
	The second moment of area	I_{yy}, I_{zz}
	Polar moment of area	I_p
Joint	Fixity	γ
	Eccentricity	e

6.2 Derivation of Semi-rigid Joint Frame Element

This section presents a finite element formulation for a semi-rigid joint frame element. The structural element parameters in the previous section are incorporated into the formulation.

When modeling a cellular material to analyze its mechanical characteristics, struts are modeled using beam or frame elements. However, use of conventional beam and frame elements can yield significant error due to their limitations. The first is that a joint among struts is expressed as a point. A point representation of a joint ignores important geometrical information in lattice structures. Struts in lattice structures have distinctive geometrical characteristics: (1) the size of joints is relatively large compared to strut length, and (2) there is a large number of joints. A large joint significantly reduces the effective length of a strut, and this affects the mechanical characteristics of a frame element such as frame stiffness and slenderness. Moreover, the effects of joints are magnified due to the large number of joints. Thus, the point representation is not suitable for modeling lattice structure. The second source of error is that a joint is rigid. A rigid joint does not allow relative angular displacement between struts. However, in reality, since it is impossible to fabricate a perfectly rigid joint, the use of conventional elements yields inaccuracy. To overcome these problems, a new frame element, a semi-rigid joint frame element, must be implemented for modeling lattice structures.

The semi-rigid joint frame element has been used to analyze large frame structures such as building structures [54, 88-91]. In large frame construction, making a perfectly rigid joint is impractical and is not economical. However, a numerical model based on the ideal rigid joint assumption cannot represent the real structural behavior. Consequently,

various methods have been proposed to investigate the effects of semi-rigid joint connection on structural characteristics. Since struts in a lattice structure play the same role as frame elements in large structures, a semi-rigid joint frame element can be applied for lattice structures as considering joint effects. A semi-rigid joint frame element consists of two regions, an effective frame and two flexible joints, as shown in Figure 6-2. Flexible joint regions are attached to both ends of the effective frame region, and they represent the lumped volume of joints. The effective frame region works as a frame element.

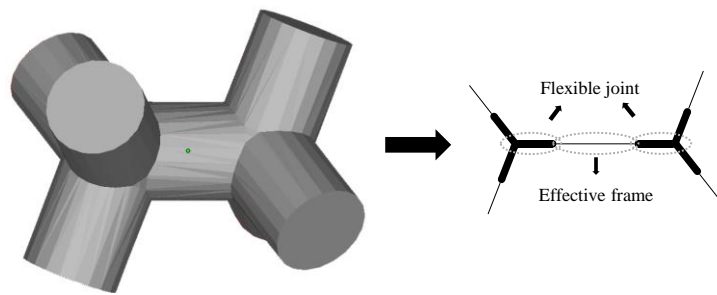


Figure 6-2 Semi-rigid joint frame element

In this research, a semi-rigid jointed beam formulation, presented by Sekulovic and Salatic [54], is modified and expanded for lattice structure implementation. The conceptual configuration of the semi-rigid joint frame element is shown in Figure 6-3. The semi-rigid joint frame element consists of two regions as mentioned above. The effective frame region is modeled using conventional frame elements. The joint region is formed by a rigid bar and a rotational spring.

For the effective frame region, an element formulation for conventional shear flexible frame element was implemented. Thus, a stiffness matrix for the region was the

same as the conventional shear flexible element except for the element length, since the length was reduced by the joint size. In the formulation of the joint region, the original approach was modified by moving the rotational springs to both ends of the frame instead of both end of the effective frame region. This modification allows relative displacement among struts, which are connected to the same joint. The fixity and eccentricity are implemented to the formulation of this region. The range of these parameters is between zero and one. The fixity controls stiffness of the torsional spring. The joint becomes rigid when the fixity value equals one. In contrast, the joint has no resistance, like a pin-joint, when the fixity becomes zero. The eccentricity is related to a length of the rigid bar, and it is defined as a ratio between rigid bar length and strut diameter. The eccentricity becomes one when the joint length is the same as the strut diameter, but it becomes zero when the point representation is assumed.

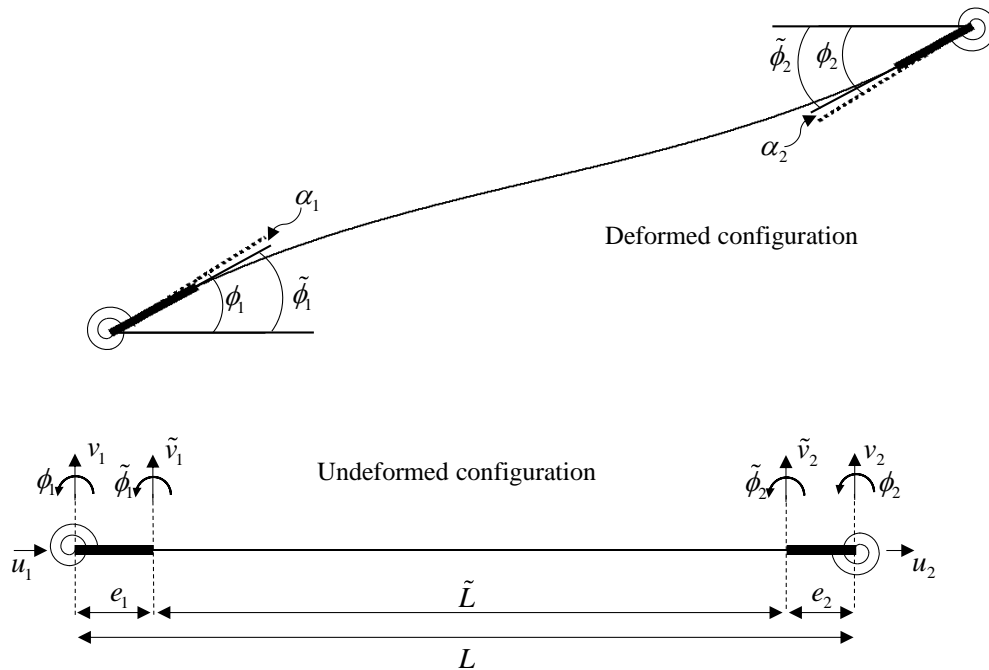


Figure 6-3 Conceptual deformed configuration of semi-rigid joint frame

The semi-rigid jointed frame element has three stiffness components for axial, torsional and flexural deformation. To formulate the axial stiffness matrix, the joint region is assumed as a reinforced truss with finite joint size. The whole frame can be considered as three connected trusses in series. The axial stiffness of the semi-rigid joint frame element is derived as follows:

$$K_{Truss} = \begin{bmatrix} k & -k \\ -k & k \end{bmatrix}, \quad \frac{1}{k} = \frac{1}{k^{e_1}} + \frac{1}{k^{\bar{L}}} + \frac{1}{k^{e_2}}$$

$$\text{where, } k^{e_1} = \frac{EA_{e_1}}{e_1} \frac{\gamma^{e_1}}{(1-\gamma^{e_1})}, \quad k^{\bar{L}} = \frac{EA_{\bar{L}}}{\bar{L}}, \quad k^{e_2} = \frac{EA_{e_2}}{e_2} \frac{\gamma^{e_2}}{(1-\gamma^{e_2})} \quad (6.1)$$

$$0 \leq \gamma^{e_1}, \gamma^{e_2} \leq 1$$

where, k^{e_1} and $k^{\bar{L}}$ are the axial stiffness in the joint and the effective truss region, respectively. γ^{e_1} and γ^{e_2} are the fixity factors for the axial stiffness. e_1 and e_2 represent the sizes of the joints. Similarly, the torsional stiffness is obtained as the following:

$$K_{Torsion} = \begin{bmatrix} k_t & -k_t \\ -k_t & k_t \end{bmatrix}, \quad \frac{1}{k_t} = \frac{1}{k_t^{e_1}} + \frac{1}{k_t^{\bar{L}}} + \frac{1}{k_t^{e_2}}$$

$$\text{where, } k_t^{e_1} = \frac{GJ_{e_1}}{e_1} \frac{\gamma_t^{e_1}}{(1-\gamma_t^{e_1})}, \quad k_t^{e_2} = \frac{GJ_{e_2}}{e_2} \frac{\gamma_t^{e_2}}{(1-\gamma_t^{e_2})}, \quad k_t^{\bar{L}} = \frac{GJ_{\bar{L}}}{\bar{L}} \quad (6.2)$$

$$0 \leq \gamma_t^{e_1}, \gamma_t^{e_2} \leq 1$$

where, $k_t^{e_1}$ and $k_t^{\bar{L}}$ are the torsional stiffness in the joint and the effective torsion bar region, respectively. $\gamma_t^{e_1}$ and $\gamma_t^{e_2}$ are the fixity factors for the torsional stiffness.

In order to formulate the flexural stiffness, two sets of nodal displacements are defined. One is a nodal displacement vector, $\mathbf{d}^T = \{v_1 \ \phi_1 \ v_2 \ \phi_2\}$, for the entire semi-rigid jointed frame. The other is an internal nodal displacement, $\tilde{\mathbf{d}}^T = \{\tilde{v}_1 \ \tilde{\phi}_1 \ \tilde{v}_2 \ \tilde{\phi}_2\}$, for the effective frame region, as shown in Figure 6-3. The relationship between two sets of displacement vector can be derived from geometrical compatibility with the small displacement assumption as follows:

$$\begin{Bmatrix} \tilde{v}_1 \\ \tilde{\phi}_1 \\ \tilde{v}_2 \\ \tilde{\phi}_2 \end{Bmatrix} = \begin{Bmatrix} v_1 + e_1 \tilde{\phi}_1 \\ \tilde{\phi}_1 \\ v_2 - e_2 \tilde{\phi}_2 \\ \tilde{\phi}_2 \end{Bmatrix} = \begin{Bmatrix} v_1 + e_1 (\phi_1 - \alpha_1) \\ \phi_1 - \alpha_1 \\ v_2 - e_2 (\phi_2 - \alpha_2) \\ \phi_2 - \alpha_2 \end{Bmatrix} = \begin{Bmatrix} v_1 \\ \phi_1 \\ v_2 \\ \phi_2 \end{Bmatrix} + \begin{bmatrix} 0 & e_1 & 0 & 0 \\ 0 & 0 & 0 & 0 \\ 0 & 0 & 0 & -e_2 \\ 0 & 0 & 0 & 0 \end{bmatrix} \begin{Bmatrix} \begin{Bmatrix} v_1 \\ \phi_1 \\ v_2 \\ \phi_2 \end{Bmatrix} - \begin{Bmatrix} 0 \\ \alpha_1 \\ 0 \\ \alpha_2 \end{Bmatrix} \end{Bmatrix} - \begin{Bmatrix} 0 \\ \alpha_1 \\ 0 \\ \alpha_2 \end{Bmatrix} \quad (6.3)$$

where, α_1 and α_2 represent the difference in the rotation angles of the two nodal displacements. In matrix form, Equation (6.3) is rewritten as follows:

$$\tilde{\mathbf{d}} = \mathbf{d} + \mathbf{E}(\mathbf{d} - \boldsymbol{\alpha}) - \boldsymbol{\alpha} = (\mathbf{I} + \mathbf{E})(\mathbf{d} - \boldsymbol{\alpha}) \quad (6.4)$$

In order that Equation (6.4) completely defines the relationship between two nodal displacements, the relationship between the nodal displacement, \mathbf{d} , and the rotational angle difference, $\boldsymbol{\alpha}$, is required. To derive the $\mathbf{d} - \boldsymbol{\alpha}$ relationship, firstly the bending moments at the joints are considered. Since the bending moments are the same as those in the rotational springs, they are represented as follows:

$$\begin{aligned} \begin{Bmatrix} M_1 \\ M_2 \end{Bmatrix} &= \begin{bmatrix} c_1 & 0 \\ 0 & c_2 \end{bmatrix} \begin{Bmatrix} \alpha_1 \\ \alpha_2 \end{Bmatrix} = \mathbf{C} \begin{Bmatrix} \alpha_1 \\ \alpha_2 \end{Bmatrix} \\ \text{where, } c_1 &= \frac{3EI_{zz}}{L} \frac{\gamma_b^{e_1}}{(1-\gamma_b^{e_1})}, \quad c_2 = \frac{3EI_{zz}}{L} \frac{\gamma_b^{e_2}}{(1-\gamma_b^{e_2})} \\ &0 \leq \gamma_b^{e_1}, \gamma_b^{e_2} \leq 1 \end{aligned} \quad (6.5)$$

where, c_1 and c_2 are rotational spring constants defined using fixity factors at both joints.

$\gamma_b^{e_1}$ and $\gamma_b^{e_2}$ are fixity factors for the torsional stiffness. The bending moments also can be obtained from the moment equilibrium over an entire semi-rigid joint frame. The relation is derived as the following:

$$\begin{Bmatrix} M_1 \\ M_2 \end{Bmatrix} = \begin{Bmatrix} \tilde{M}_1 + e_1 \tilde{V}_1 \\ \tilde{M}_2 - e_2 \tilde{V} \end{Bmatrix} \quad (6.6)$$

By combining Equations (6.5) and (6.6), the rotational angle difference vector at the joint can be represented using the internal force vector as follows:

$$\mathbf{C} \begin{Bmatrix} \alpha_1 \\ \alpha_2 \end{Bmatrix} = \begin{Bmatrix} \tilde{M}_1 + e_1 \tilde{V}_1 \\ \tilde{M}_2 - e_2 \tilde{V} \end{Bmatrix} = \begin{bmatrix} e_1 & 1 & 0 & 0 \\ 0 & 0 & -e_2 & 1 \end{bmatrix} \begin{Bmatrix} \tilde{V}_1 \\ \tilde{M}_1 \\ \tilde{V}_2 \\ \tilde{M}_2 \end{Bmatrix} = \mathbf{F} \begin{Bmatrix} \tilde{V}_1 \\ \tilde{M}_1 \\ \tilde{V}_2 \\ \tilde{M}_2 \end{Bmatrix} \quad (6.7)$$

Since a conventional shear deformable frame element is used for the effective frame region, the internal force-displacement equation is represented as the following:

$$\begin{Bmatrix} \tilde{V}_1 \\ \tilde{M}_1 \\ \tilde{V}_2 \\ \tilde{M}_2 \end{Bmatrix} = \frac{EI_{zz}}{(1+\Lambda)\tilde{L}^3} \begin{bmatrix} 12 & 6\tilde{L} & -12 & 6\tilde{L} \\ 6\tilde{L} & (4+\Lambda)\tilde{L}^2 & -6\tilde{L} & (2-\Lambda)\tilde{L}^2 \\ -12 & -6\tilde{L} & 12 & -6\tilde{L} \\ 6\tilde{L} & (2-\Lambda)\tilde{L}^2 & -6\tilde{L} & (4+\Lambda)\tilde{L}^2 \end{bmatrix} \begin{Bmatrix} \tilde{v}_1 \\ \tilde{\phi}_1 \\ \tilde{v}_2 \\ \tilde{\phi}_2 \end{Bmatrix} = \tilde{\mathbf{K}}_b \tilde{\mathbf{d}} \quad (6.8)$$

$$\Lambda = \frac{12EI_{zz}}{GAK_s\tilde{L}^2}$$

where, \tilde{V}_1 and \tilde{V}_2 are shear force and \tilde{M}_1 and \tilde{M}_2 are bending moment in the frame, respectively. I_{zz} is the second moment of area about the z-axis and K_s is a shear correction factor. Substituting Equation (6.8) into Equation (6.7), the relationship between the rotational angle difference and the nodal displacement vector in the effective frame region is derived as follows:

$$\mathbf{C} \begin{Bmatrix} \alpha_1 \\ \alpha_2 \end{Bmatrix} = \mathbf{F}\tilde{\mathbf{K}}_b\tilde{\mathbf{d}} = \mathbf{F}\tilde{\mathbf{K}}_b(\mathbf{I} + \mathbf{E})(\mathbf{d} - \mathbf{a}) \quad (6.9)$$

$$\text{where, } \mathbf{a} = \begin{bmatrix} 0 & 0 \\ 1 & 0 \\ 0 & 0 \\ 0 & 1 \end{bmatrix} \begin{Bmatrix} \alpha_1 \\ \alpha_2 \end{Bmatrix}$$

Simplifying Equation (6.9), the rotational angle difference is obtained as the following equations:

$$\left(\mathbf{C} + \mathbf{F}\tilde{\mathbf{K}}_b(\mathbf{I} + \mathbf{E}) \begin{bmatrix} 0 & 0 \\ 1 & 0 \\ 0 & 0 \\ 0 & 1 \end{bmatrix} \right) \begin{Bmatrix} \alpha_1 \\ \alpha_2 \end{Bmatrix} = \mathbf{B} \begin{Bmatrix} \alpha_1 \\ \alpha_2 \end{Bmatrix} = \mathbf{F}\tilde{\mathbf{K}}_b(\mathbf{I} + \mathbf{E})\mathbf{d} \quad (6.10)$$

$$\begin{Bmatrix} \alpha_1 \\ \alpha_2 \end{Bmatrix} = \mathbf{B}^{-1} \mathbf{F} \tilde{\mathbf{K}}_b (\mathbf{I} + \mathbf{E}) \mathbf{d} = \mathbf{S} \mathbf{d} \quad (6.11)$$

$$\mathbf{a} = \begin{Bmatrix} 0 \\ \alpha_1 \\ 0 \\ \alpha_2 \end{Bmatrix} = \begin{bmatrix} 0 & 0 & 0 & 0 \\ s_{11} & s_{12} & s_{13} & s_{14} \\ 0 & 0 & 0 & 0 \\ s_{21} & s_{22} & s_{23} & s_{24} \end{bmatrix} \mathbf{d} = \mathbf{S} \mathbf{d} \quad (6.12)$$

Substituting Equation (6.12) into Equation (6.4), the relationship between two nodal displacement vectors is completely determined as follows:

$$\tilde{\mathbf{d}} = (\mathbf{I} + \mathbf{E})(\mathbf{d} - \mathbf{a}) = (\mathbf{I} + \mathbf{E})(\mathbf{I} - \mathbf{S}) \mathbf{d} \quad (6.13)$$

Finally, the flexural stiffness matrix can be derived from stored strain energy in the entire semi-rigid joint frame element. The stored energy in the effective frame region and the rotational springs is represented as the following equations:

$$U_{frame} = \frac{1}{2} \tilde{\mathbf{d}}^T \tilde{\mathbf{K}}_b \tilde{\mathbf{d}} \quad (6.14)$$

$$U_{spring} = \frac{1}{2} \begin{Bmatrix} 0 & \alpha_1 & 0 & \alpha_2 \end{Bmatrix} \begin{bmatrix} 0 & 0 & 0 & 0 \\ 0 & c_1 & 0 & 0 \\ 0 & 0 & 0 & 0 \\ 0 & 0 & 0 & c_2 \end{bmatrix} \begin{Bmatrix} 0 \\ \alpha_1 \\ 0 \\ \alpha_2 \end{Bmatrix} = \frac{1}{2} \mathbf{a}^T \mathbf{C}_s \mathbf{a} \quad (6.15)$$

The total energy is obtained by summing Equations (6.14) and (6.15) as follows:

$$U = U_{frame} + U_{spring} = \frac{1}{2} \tilde{\mathbf{d}}^T \tilde{\mathbf{K}}_b \tilde{\mathbf{d}} + \frac{1}{2} \boldsymbol{\alpha}^T \mathbf{C}_s \boldsymbol{\alpha} \quad (6.16)$$

Substituting Equations (6.12) and (6.13) into Equation (6.16), the total stored energy is rewritten as follows:

$$U = \frac{1}{2} \mathbf{d}^T \left[(\mathbf{I} - \mathbf{S})^T (\mathbf{I} + \mathbf{E})^T \tilde{\mathbf{K}}_b (\mathbf{I} + \mathbf{E})(\mathbf{I} - \mathbf{S}) + \mathbf{S}^T \mathbf{C}_s \mathbf{S} \right] \mathbf{d} \quad (6.17)$$

The flexural stiffness matrix for the entire semi-rigid joint beam element is obtained from Equation (6.17) as follows:

$$\mathbf{K}_b = (\mathbf{I} - \mathbf{S})^T (\mathbf{I} + \mathbf{E})^T \tilde{\mathbf{K}}_b (\mathbf{I} + \mathbf{E})(\mathbf{I} - \mathbf{S}) + \mathbf{S}^T \mathbf{C}_s \mathbf{S} \quad (6.18)$$

The semi-rigid jointed frame element is obtained by collecting the stiffness components in Equations (6.1), (6.2) and (6.18). Details in the stiffness matrix are explained in Appendix A.

6.3 Effective Structural Element Parameters

In the semi-rigid formulation derived in Section 6.2, the stiffness matrix is a function of structural parameters such as material properties, geometrical dimensions, fixity and eccentricity. Geometrical discrepancies that arise during the AM process alter the structural element parameters, and as a result, the mechanical properties of the cellular material are changed. When modeling an additively manufactured cellular material using semi-rigid frame elements, geometrical degradation due to the AM process

can be considered by utilizing the effective values of the structural element parameters. This section explains how to calculate the effective structural element parameters.

Since the as-fabricated voxel model in Chapter 5 is capable to capture the geometrical degradation due to AM processes, we can use the voxel model to assess the deterioration. Accordingly, the effective structural element parameters can be determined by comparing the mechanical responses of an as-fabricated voxel model of struts with those of a semi-rigid joint frame model. Figure 6-4 shows a basic concept of a determination procedure for effective structural element parameter.

The first step is to construct the as-fabricated voxel models and semi-rigid joint frame models of representative struts in a lattice structure. Next, structural analysis that simulates tensile and bending tests is performed to obtain the displacement fields. The last step is to approximate the resulting displacement field of the as-fabricated voxel model using the displacement field of the semi-rigid joint frame model by changing the structural element parameters. The effective values of the structural element parameters are determined as the values that result in the minimal squared error sum.

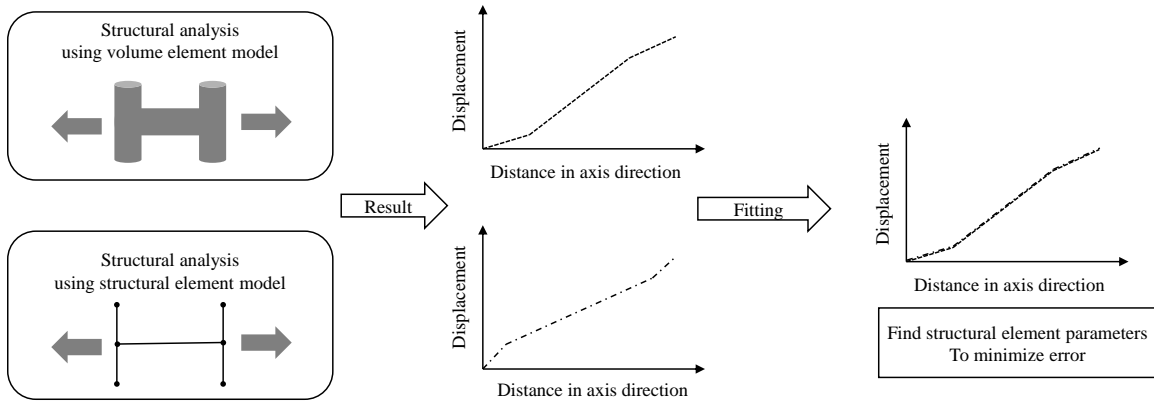


Figure 6-4 Structural element parameter determination procedure

In this research, three major structural element parameters are considered because the parameters in Table 6-1 are interrelated: (1) effective strut diameter, (2) eccentricity, and (3) fixity. These values are calculated in two loading conditions, i.e. in the tensile loading and in the flexural bending loading. Each set of the structural element parameters is integrated into each component in the stiffness matrix in the previous section. In addition, the fabricated density of a strut that is related to density of an additively manufactured cellular material is also calculated.

6.3.1 Fabricated Density

The fabricated density is defined by a volume ratio between an as-fabricated model and an intact model of a strut as follows:

$$V_f = \frac{V_{\text{as-fabricated}}}{V_{\text{STL}}} \quad (6.19)$$

where, V_f , $V_{\text{as-fabricated}}$ and V_{STL} are the fabricated density, the volume of the as-fabricated model, and the volume of the intact STL file, respectively. The volume of the models can be calculated in various pre-processing software for finite element analysis, such as HyperMesh[®] and ABAQUS[®] CAE.

6.3.2 Effective Strut Diameter, Eccentricity and Fixity

In order to calculate the effective value of the structural element parameters in the semi-rigid joint frame element formulation, the mechanical responses of a target strut are required. Since a strut works as a truss, beam or frame in a cellular material, two

structural responses, tensile and bending responses, are required. The structural behavior is obtained using the as-fabricated voxel models to integrate the AM process effects. Since the as-fabricated voxel models are composed of voxels, the finite element method can be directly implemented to the models.

To simulate the tensile and bending loading condition, two types of boundary conditions were imposed to the voxel models as shown in Figure 6-5. The analysis was performed in ABAQUS[®]. The typical resulting axial and lateral displacement fields from the analysis are represented as blue lines in Figure 6-6. The effective structural element parameters were determined by fitting the blue lines using the response of semi-rigid joint frame denoted by red lines in Figure 6-6.

Firstly, the displacement field from the tensile loading condition was approximated to determine the effective structural element parameters for constructing the axial component in the stiffness matrix. Theoretically, the axial displacement of a prismatic truss is linearly increased through the axial direction. However, the resulting displacement field is not linear due to the joint stiffness. The slope of the displacement field near the joints is less than that in the middle of the strut because the stiffness is larger due to the additional joint stiffness. Thus, the displacement can be approximated using the axial response of the semi-rigid joint frame, which consists of three line segments as follows:

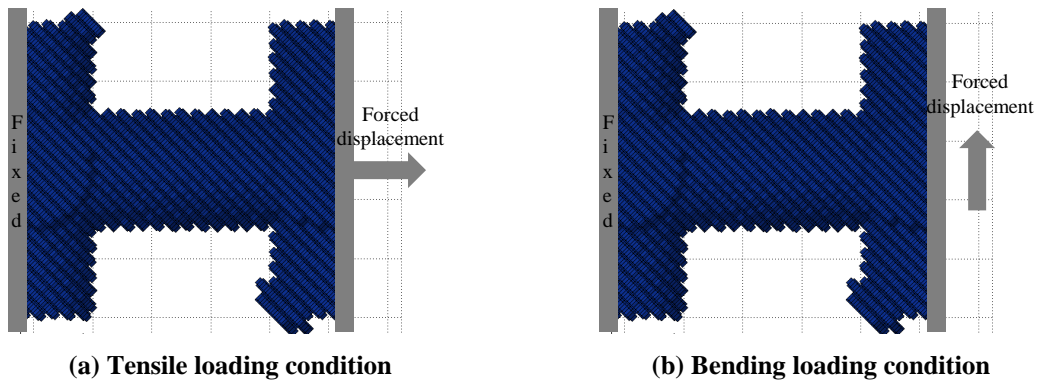
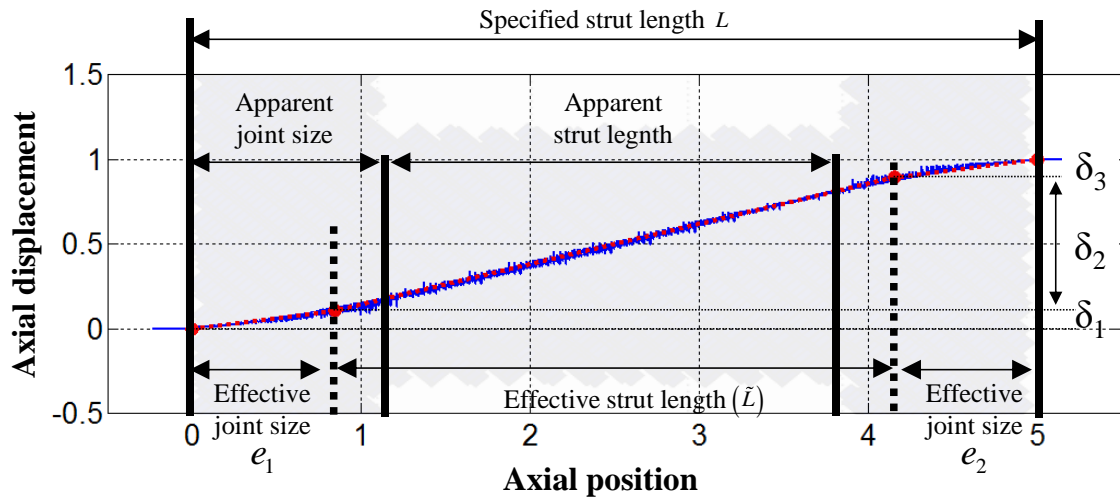
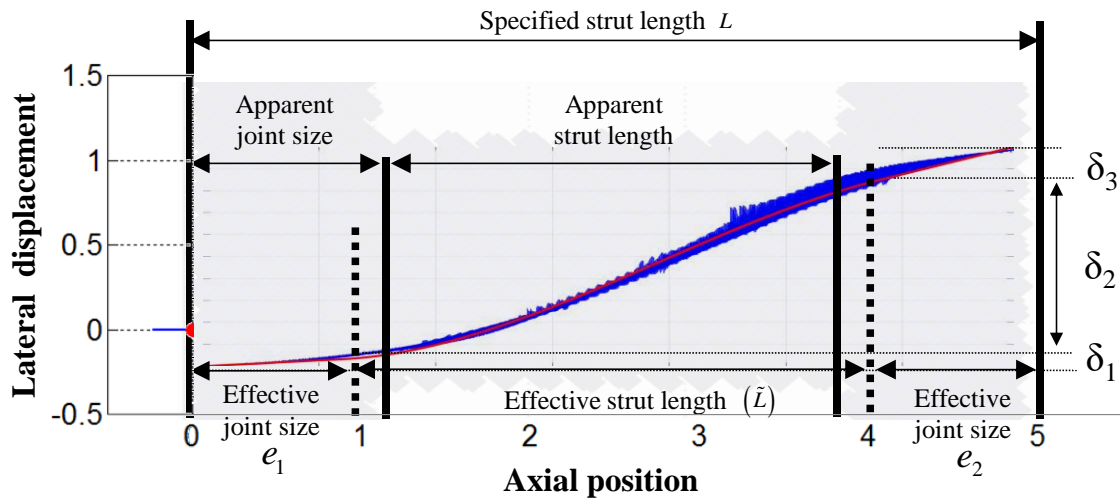


Figure 6-5 Boundary conditions



(a) Axial displacement field in tensile loading condition



(b) Lateral displacement in bending loading condition

Figure 6-6 Typical resulting displacement fields

$$u(s) = \begin{cases} m^{e_1} s & 0 \leq s < e_1 \\ m^{\tilde{L}} (s - e_1) + m^{e_1} s & e_1 \leq s < e_1 + \tilde{L} \\ m^{e_2} (s - (e_1 + \tilde{L})) + m^{\tilde{L}} \tilde{L} + m^{e_1} e_2 & e_1 + \tilde{L} \leq s \leq \tilde{L} \end{cases} \quad (6.20)$$

where, s is the local axial coordinates in the frame element. The notations are the same as in Equation (6.1).

In order to determine the displacement field in Equation (6.20), five parameters are required. Three parameters (m^{e_1} , $m^{\tilde{L}}$ and m^{e_2}) are the slope of the segments, and the other two parameters (e_1^* and e_2^*) are the effective joint size. These parameters are determined by minimizing the squared error between the two responses using the following formulation:

$$\begin{aligned} & \text{Find } e_1^*, e_2^*, m^{e_1^*}, m^{\tilde{L}^*} \text{ and } m^{e_2^*} \\ & \min \sum (u_a(s) - u(s))^2 \end{aligned} \quad (6.21)$$

where, $u_a(s)$ is the axial displacement field of the as-fabricated voxel model. The remaining effective structural element parameters were also determined as follows:

$$\tilde{L} = L - e_1^* - e_2^* \quad (6.22)$$

$$d_{eff} = \sqrt{\frac{4F_R}{\pi E m^{\tilde{L}^*}}} \quad (6.23)$$

$$\begin{aligned}
\gamma_1 &= \frac{k^{e_1^*}}{k^{e_1^*} + k_{nom}^{e_1}} \\
\gamma_2 &= \frac{k^{e_2^*}}{k^{e_2^*} + k_{nom}^{e_2}} \\
k^{e_1^*} &= \frac{F_R}{e_1^*}, k^{e_2^*} = \frac{F_R}{e_2^*}, k_{nom} = \frac{EA_{eff}}{d_{eff}}
\end{aligned} \tag{6.24}$$

where, F_R is the reaction force at the fixed end. $k^{e_1^*}$ and $k^{e_2^*}$ are the calculated joint stiffness based on the as-fabricated voxel model, and k_{nom}^e is the nominal joint stiffness. The effective structural parameters in Equations (6.21) - (6.24) are used for constructing the axial and torsional stiffness matrix components.

Next, the same procedure is applied for determining the effective structural parameters in the flexural stiffness component. The lateral displacement of the semi-rigid joint frame is also divided into three segments as follows:

$$v(s) = \begin{cases} \alpha_1 s & 0 \leq s < e_1 \\ \begin{bmatrix} N_1(s) & N_2(s) & N_3(s) & N_4(s) \end{bmatrix} \begin{bmatrix} \alpha_1 e_1 \\ \alpha_1 \\ 1 - \alpha_2(L-s) \\ \alpha_2 \end{bmatrix} & e_1 \leq s < e_1 + \tilde{L} \\ 1 - \alpha_2(L-s) & e_1 + \tilde{L} \leq s \leq \tilde{L} \end{cases} \tag{6.25}$$

where, $N_i(s)$ is the shape function of the shear flexible beam element as follows:

$$\begin{aligned}
N_1(s) &= \bar{\Lambda}(1 - 3s^2 + 2s^3 + \Lambda(1 - s)) \\
N_2(s) &= \tilde{L}\bar{\Lambda}\left(s - 2s^2 + s^3 + \frac{\Lambda}{2}(s - s^2)\right) \\
N_3(s) &= \bar{\Lambda}(3s^2 - 2s^3 + \Lambda s) \\
N_4(s) &= \tilde{L}\bar{\Lambda}\left(-s^2 + s^3 - \frac{\Lambda}{2}(s - s^2)\right) \\
\bar{\Lambda} &= \frac{1}{(1 + \Lambda)}
\end{aligned} \tag{6.26}$$

The effective values of the structural element parameters were determined by minimizing the squared error sum using the following optimization problem formulation:

$$\begin{aligned}
& \text{Find } e_1^*, e_2^*, \gamma_1^*, \gamma_2^*, d_{eff} \\
& \min \sum (v_a(s) - v(s))^2
\end{aligned} \tag{6.27}$$

where, $v_a(s)$ is the lateral displacement of the as-fabricated voxel model. This formulation determines the effective structural element parameters without further calculation. The obtained effective parameters were applied for constructing the flexural stiffness matrix.

6.4 AM Process Effects on Structural Element Parameters

This section presents a series of parametric studies to investigate AM process effects on structural element parameters. The selected DMP parameters for the material extrusion process are the joint shape, build angle and raster angle, and for the powder bed fusion process, the powder size and build angle are selected. The effective structural parameters in the parametric studies are for the axial stiffness component.

6.4.1 Material Extrusion

To study the AM process parameters, parametric studies are performed without uncertainty firstly and then, the manufacturing uncertainties are imposed. In the parametric studies, manufacturing parameters for constructing as-fabricated voxel models were selected for the Statasys 400mc machine. The T16 nozzle tip, which yields 0.356 mm deposition width and 0.178 mm layer thickness, was assumed, and the deposition paths were generated using the MATLAB function explained in Section 4.1.

6.4.1.1 Joint Shape

In order to examine the effects of the joint shape in a cellular material, four different joint shapes were studied. Figure 6-7 presents the selected joint shapes. The size of the strut diameter was 2 mm for cubic unit cells and 1.5 mm for a diamond unit cell. To determine the effective structural parameters, as-fabricated voxel models of the struts were generated, and they were exported to commercial FEA software, ABAQUS®, with axial loading conditions. From the analysis, the axial displacement field in the struts was obtained. The structural element parameters were determined using the process, which was explained in a previous section.

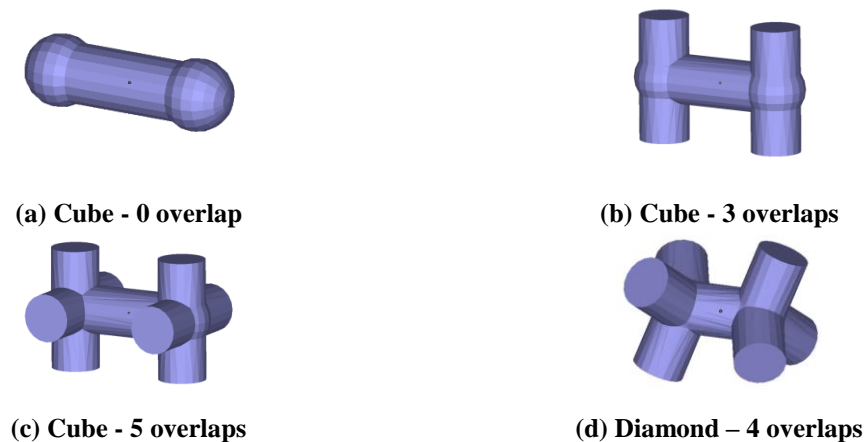
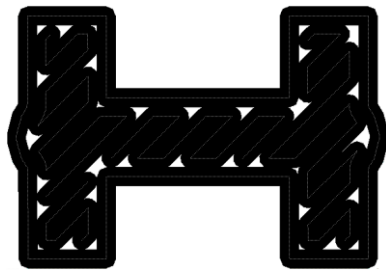


Figure 6-7 Joint models

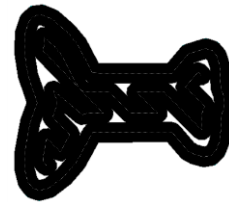
The resulting effective structural parameters are listed in Table 6-2. The fabricated densities of struts that have the same unit cell shape are similar. The struts in the cubic unit cell result in 90 ~ 91% of the fabricated density. However, the strut in the diamond unit cell exhibits 94% of the density. This is the result of the different deposition paths between the two unit cells, which are dependent on the shape as shown in Figure 6-8. Since the strut in the cubic unit cell has more voids among the deposition paths, it shows lower fabricated density than the strut in the diamond unit cell does.

Table 6-2 Effective structural element parameters of the joint models

Structural element parameters	Cube 0 overlap	Cube 3 overlaps	Cube 5 overlaps	Diamond 4 overlaps
Fabricated density	90%	91%	90%	94%
Effective strut length (mm) / specified length (mm)	3.90 / 5	3.50 / 5	3.38 / 5	1.21 / 2.1651
Eccentricity	0.55	0.75	0.81	0.64
Fixity	0.51	0.54	0.58	0.57
Effective strut diameter (mm) / specified diameter (mm)	1.75 / 2	1.76 / 2	1.76 / 2	1.35 / 1.5



(a) Cube – 5 overlaps



(b) Diamond – 4 overlaps

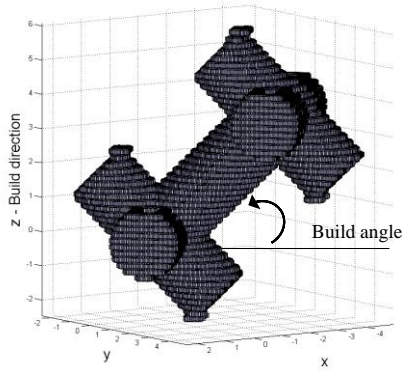
Figure 6-8 Pattern of deposition paths

It is noteworthy that the trend of change in the effective strut length and eccentricity implies that as more struts are overlapped at the joints, the size of a joint is increased and, as a result, the effective strut length is reduced. The eccentricity of the joint with five struts was 47% bigger than that of the non-overlapping joint. Furthermore, the fixity also increased as the joint became larger. The fixity of the five overlapping joint was 13% bigger than that of the non-overlapping joint. From this result, it can be concluded that the larger joint shape yields the stiffer effective structural parameters related to joint properties.

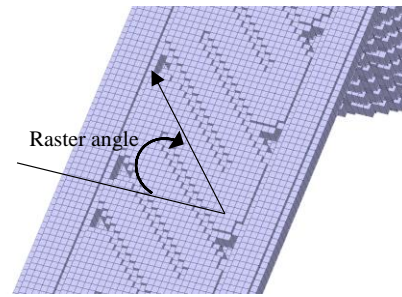
In contrast, the joint shape does not affect the effective strut diameter, which is related to the frame region. The size of the effective diameter does not change as the shape varies. Thus, the structural element parameters in the joint and frame can be considered as properties independent of each other. In later parametric studies, the joint model (c) in Figure 6-7 is used.

6.4.1.2 Build Angles and Raster Angle

In this section, the effects of two direction angles are studied: the build angle and the raster angle. The build angle is the angle with respect to the build plane, which is related to the stair stepping phenomenon. The raster angle defines the direction of infill deposition paths. The build and raster angles affect the internal and external deposition shapes. Figure 6-9 shows the build angle and the raster angle.

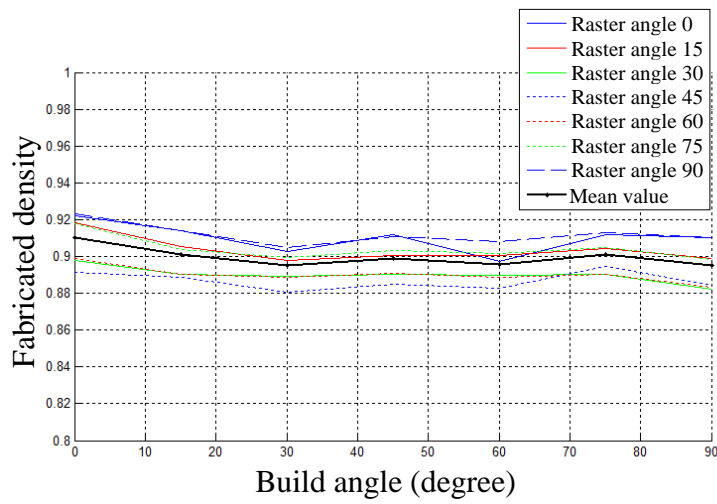


(a) Building angle

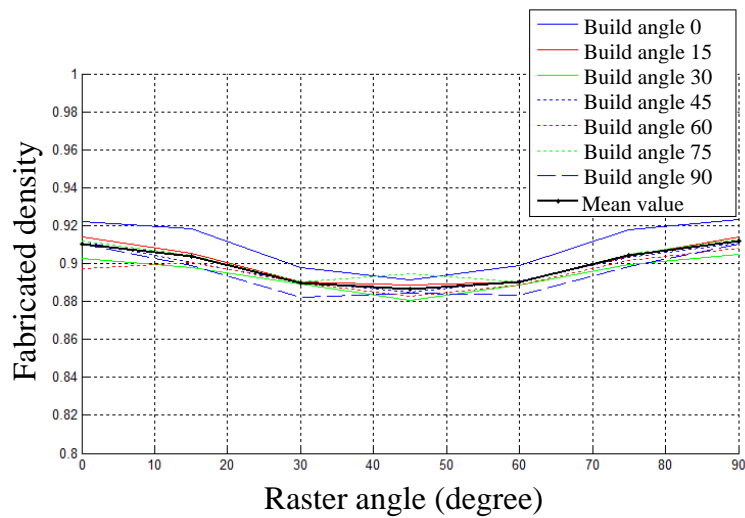


(b) Raster direction angle

Figure 6-9 Inclined angle and raster direction angle



(a) Fabricated density as varying build angle



(b) Fabricated density as varying raster angle

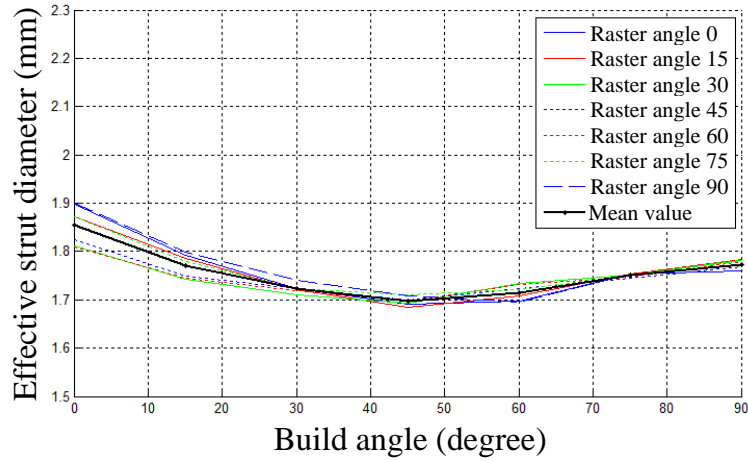
Figure 6-10 Change in fabricated density

- *Fabricated Density*

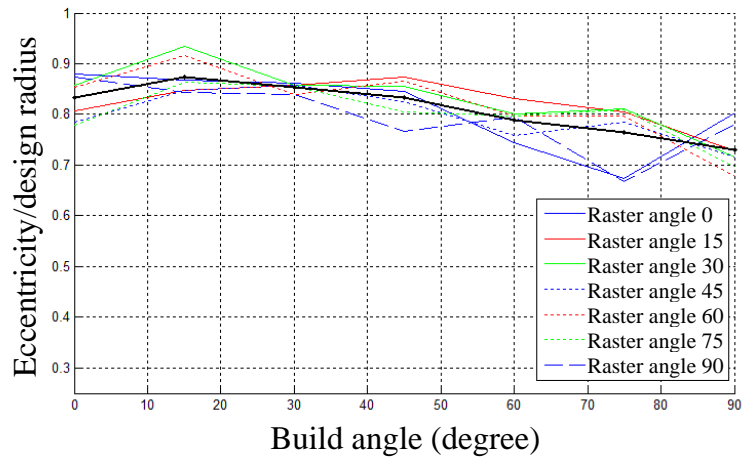
The change in the fabricated density with respect to build and raster angles is represented in Figure 6-10. This parameter is related to the amount of raw material in the fabricated strut. The fabricated density is insensitive to changes in the build angle. However, the change in the raster angle leads to a trend in which the fabricated density is at a minimum at $\pm 45^\circ$, which yields parallel or perpendicular deposition paths to the strut direction.

- *Effective diameter, Eccentricity and Fixity*

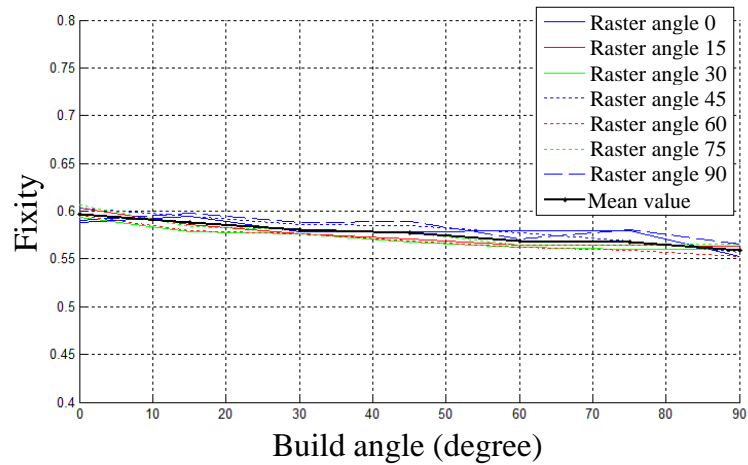
The change of structural element parameters due to increase in the build angle and raster angle is shown in Figure 6-11 and Figure 6-12, respectively. The effective strut diameter is at a minimum at the 45° build angle. This is consistent with the result in Section 5.3.4. Since this parameter is related to the frame region where the stair step effect dominates the fabricated shape, the effective diameter is reduced at the 45° build angle. However, the effect of raster angle on the effective strut diameter is limited except for low build angles such as 0° and 15° . At the low build angles, fewer stair steps are generated and, as a result, the amount of raw material used affects the effective strut diameter more. Thus, the trend of the effective strut diameter follows the trend of the fabricated density in Figure 6-10, but the effect is diminished at high build angles.



(a) Effective strut diameter

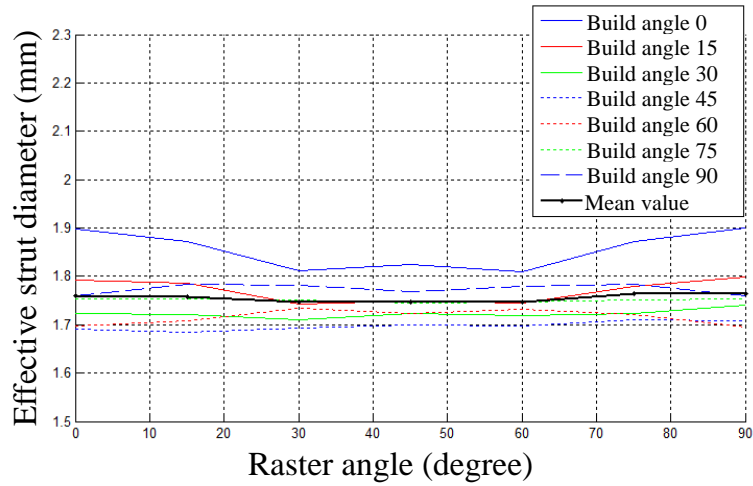


(b) Eccentricity

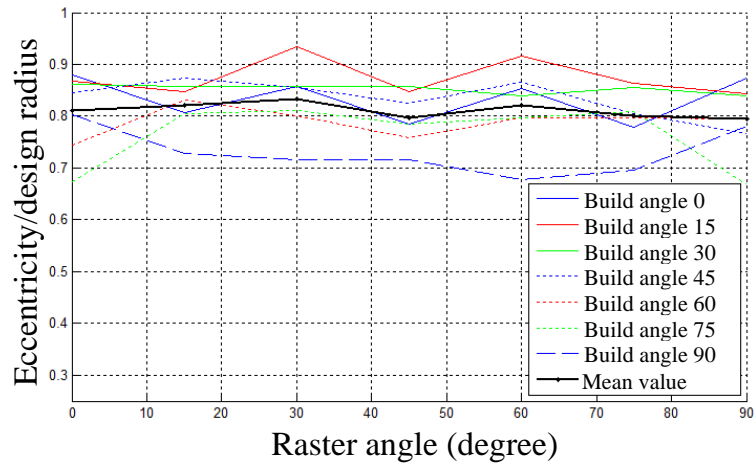


(c) Fixity

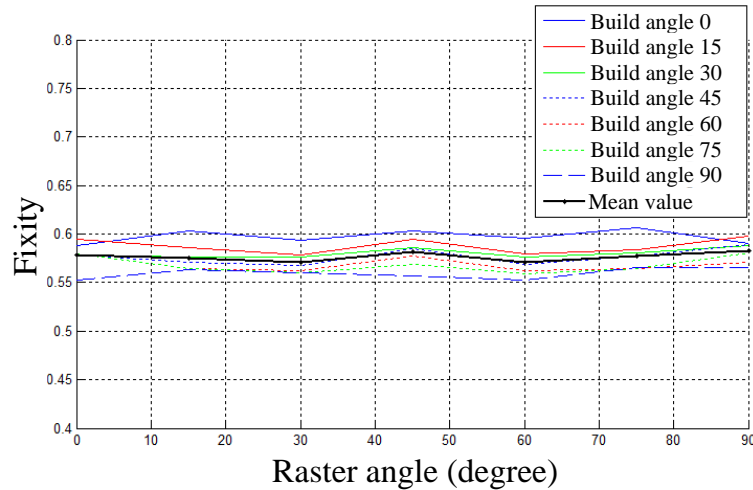
Figure 6-11 Structural element parameters as varying the build angle



(a) Effective strut diameter

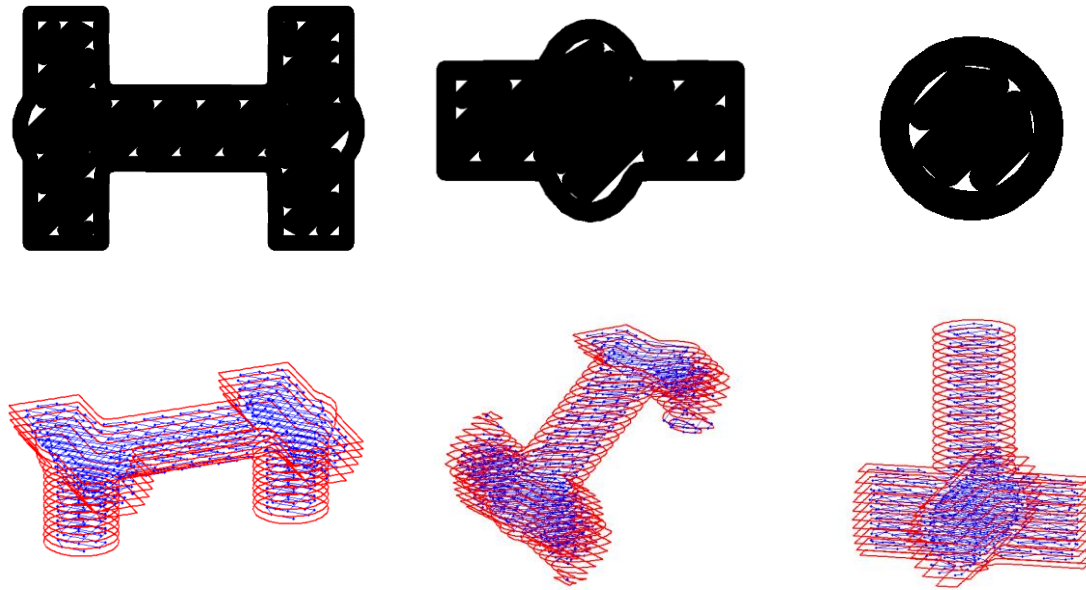


(b) Eccentricity



(c) Fixity

Figure 6-12 Structural element parameters as varying the raster angle



(a) 0° inclined angle

(b) 45° inclined angle

(c) 90° inclined angle

Figure 6-13 Deposition path near joint

Moreover, the build angle also has influence on the joint properties, such as eccentricity and fixity. The effective joint size and joint stiffness in terms of the eccentricity and fixity decrease as the build angle increases. This can be explained by observing the deposition patterns. Figure 6-13 presents the deposition paths at three build angles. In the low build angle, the filaments are deposited across joint regions through frame regions. However, the number of filaments passing through joint is reduced as the build angle increases. This indicates that a joint at a low build angle can support more loading from struts and, as a result, the joint properties are increased. However, the raster angle does not have a critical influence on the joint properties. From the parametric studies performed in this section, it can be concluded that the effects of the build angle are more dominant on the structural behavior of the additively manufactured struts.

6.4.1.3 Manufacturing Uncertainty

To study the effect of the manufacturing uncertainties, the location and the deposition width are perturbed based on the probabilistic distributions mentioned in Section 4.1.3. The uncertainties are applied to steps for deposition shape image generation and as-fabricated voxel modeling. The applied distribution for the location of the nozzle is a uniform distribution with a range of 0.011-0.014 mm. The distribution of the scaling factor for the width is a normal distribution, with the mean value of 1 and the standard deviation of 0.0158.

In order to obtain the probabilistic distributions of the structural element parameters, twenty as-fabricated voxel models were generated at each build angle. The raster angle was fixed to 45° because the parametric studies in the previous section indicate that the raster angle does not meaningfully influence the structural parameters.

• Fabricated Density

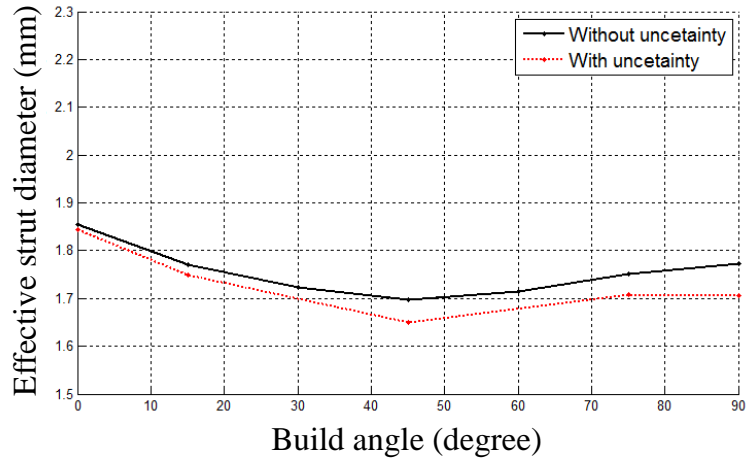
Table 6-3 lists the mean values and the standard deviation of the fabricated density with manufacturing uncertainty at each build angle. The densities are compared with the fabricated density without manufacturing uncertainty. The fabricated densities without manufacturing uncertainty are the mean values in Figure 6-10 (a), which are obtained from as-fabricated voxel models constructed without uncertainties in Section 6.4.1.2. Since the standard deviation is small, which yields 99% of the density within the mean value $\pm 1.3\%$, the distributions can be explained with the mean values. The comparison indicates that the geometrical uncertainties reduce the fabricated density by about 4 ~ 5%. The variation of the deposition width results in the difference.

Table 6-3 Comparison of fabricated density

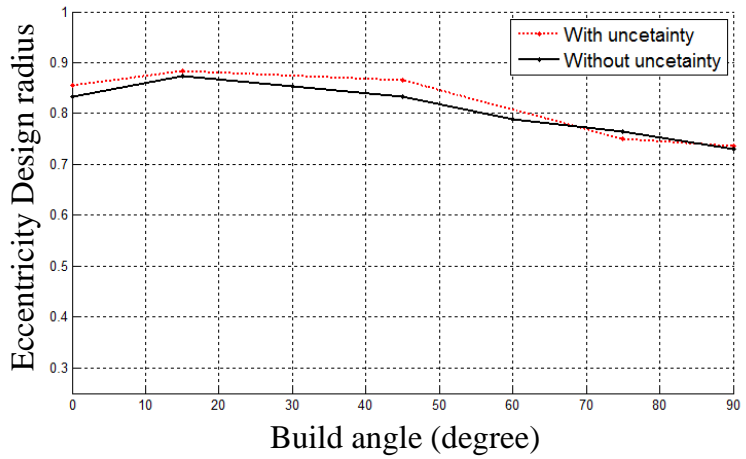
	Build angle				
	0°	15°	45°	75°	90°
With manufacturing uncertainty (Mean value / Standard deviation)	0.866/ 0.013	0.862/ 0.010	0.862 / 0.011	0.862 / 0.01	0.850 / 0.01
Without manufacturing uncertainty	0.910	0.901	0.899	0.901	0.895
Difference (%)	-4.86%	-4.38%	-4.09%	-4.32%	-5.04%

● Effective diameter, Eccentricity and Fixity

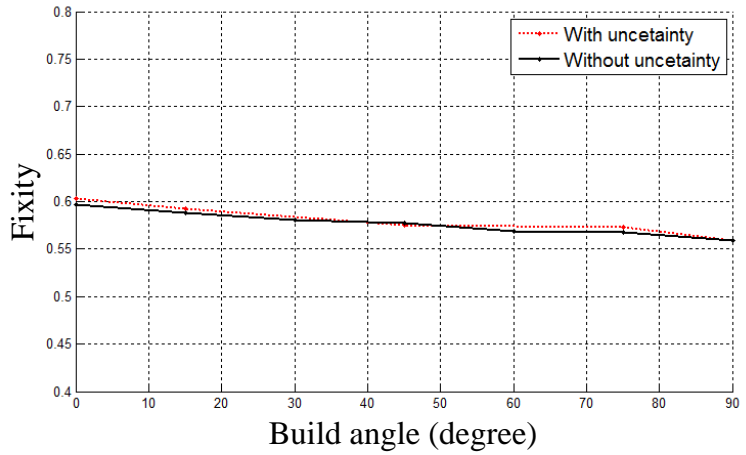
The resulting structural element parameters as a function of build angle are shown in Figure 6-14. The black line indicates the SEP values without manufacturing uncertainty, and the red dotted line expresses the SEP values with manufacturing uncertainty. For SEP related to joint characteristics, the difference in the two lines at each angle is small. This means that manufacturing uncertainties caused by machine tolerance have limited impact on the SEP associated with joint properties. However, the effective strut diameter, which is related to the frame region, is affected by the manufacturing uncertainties. The amount of reduction in diameter becomes larger as the build angle increases. This can be explained based on the deposition paths in Figure 6-13. In the 0° build angle shown in Figure 6-13 (a), the dimension of the strut in the horizontal direction is much larger than the dimension in the vertical direction. Accordingly, relative manufacturing errors in the horizontal direction become smaller. Thus, only the error in vertical direction alters the shapes. However, in the 90° build angles shown in Figure 6-13 (c), errors in both directions can affect the deposited shape. This results in larger reduction of the effective strut diameter in the high build angle.



(a) Effective strut diameter



(b) Eccentricity



(c) Fixity

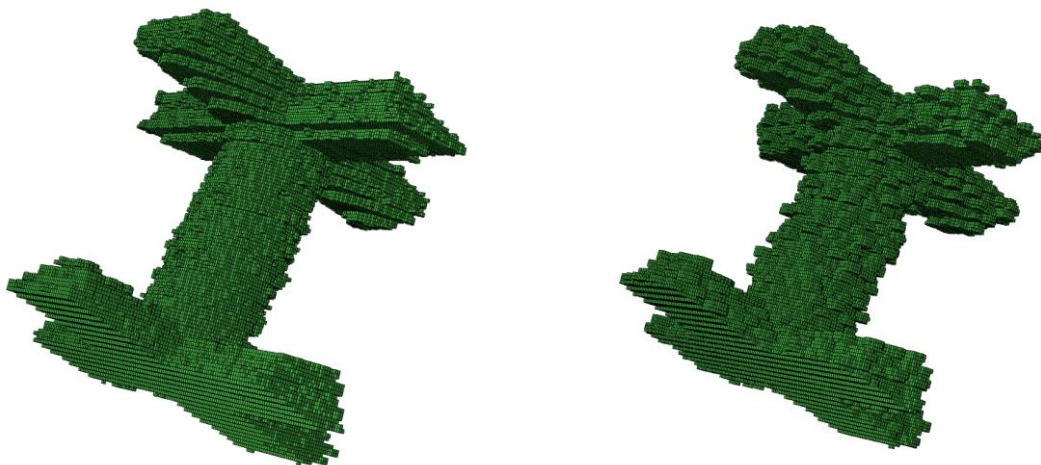
Figure 6-14 Degradation of structural parameters due to manufacturing uncertainty

6.4.2 Powder Bed Fusion Process

To investigate the effect of the PBF process, as-fabricated voxel models of a strut in Figure 6-7 (c) with 0.4 mm design diameter were generated and their effective structural element parameters were determined. The manufacturing parameters were set for EBM and SLM processes. The layer thickness and strut length were set to 0.04 mm and 1.2 mm, respectively. Powder particles were randomly generated with distributions represented in Figure 4-9. Two parameters were studied: Powder size and build angle. Ten as-fabricated voxel models were constructed at seven difference build angles: 0°, 15°, 30°, 45°, 60°, 75° and 90°. In total, 140 voxel models were studied.

6.4.2.1 Powder size

Figure 6-15 shows a comparison between two voxel models that were generated based on SLM and EBM process parameters. Apparently, the strut using EBM manufacturing parameters has a rougher surface because the Arcam powder has larger particle morphology.



(a) Utilization of Raymor powder distribution

(b) Utilization of Arcam powder distribution

Figure 6-15 As-fabricated voxel models based on each distribution

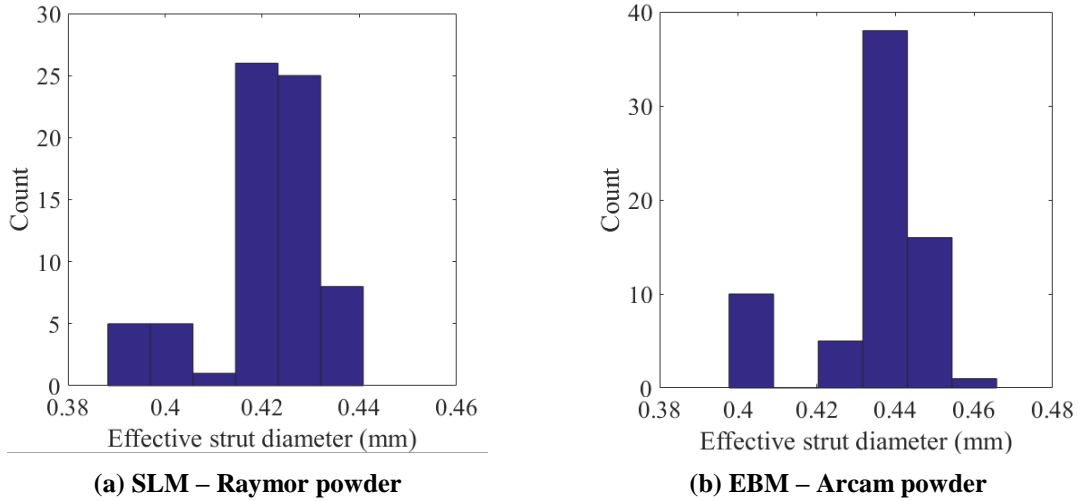


Figure 6-16 Histogram for effective strut diameter

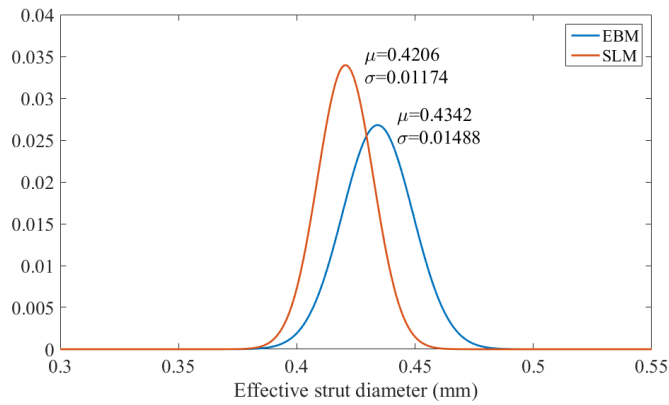


Figure 6-17 Probabilistic density functions of effective strut diameters

The resulting effective strut diameters are compared in Figure 6-16 and 6-17. The distribution of SLM processed struts has a lower mean value, and its standard deviation is smaller than that of the distribution of EBM processed struts. Thus, the variation of SLM processed effective diameter is smaller. The reason for this difference can be explained the powder morphology. The mean value and standard deviation of SLM powder are smaller those of EBM powder. Accordingly, the particles stuck on the surface are smaller. This affects the effective strut diameter distribution.

6.4.2.2 Build angle

To examine the effect of build angle, the effective structural parameters are compared for varying build angles. Figure 6-18 shows the effective strut diameter at each build angle. The mean values of the effective strut diameter increase as the build angle increases up to a 30° build angle. After the 30° build angle, the mean values of the effective diameter are slightly reduced. This is a different trend from that shown in the material extrusion process. In the ME process, the fabricated diameter with a certain build angle is reduced. However, in the PBF process, powder particles around the melting pool fill the discontinuous region between layers and, as a result, the effective strut diameters are thicker in the high build angles, as represented in Figure 6-19.

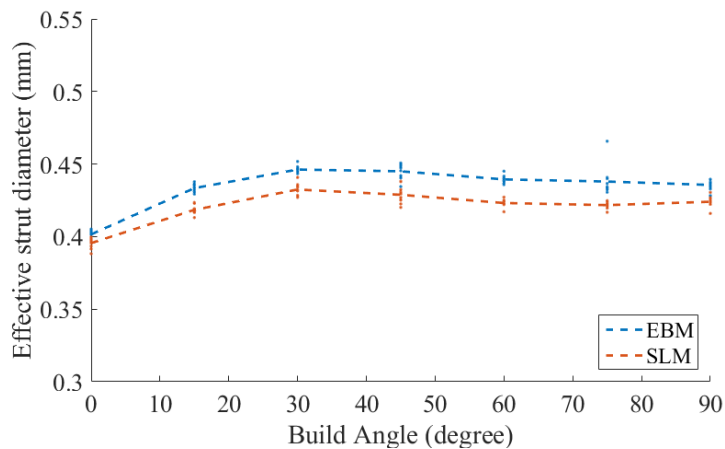


Figure 6-18 Effective strut diameter with varying build angle

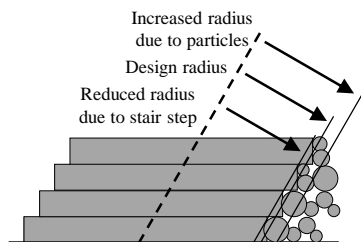
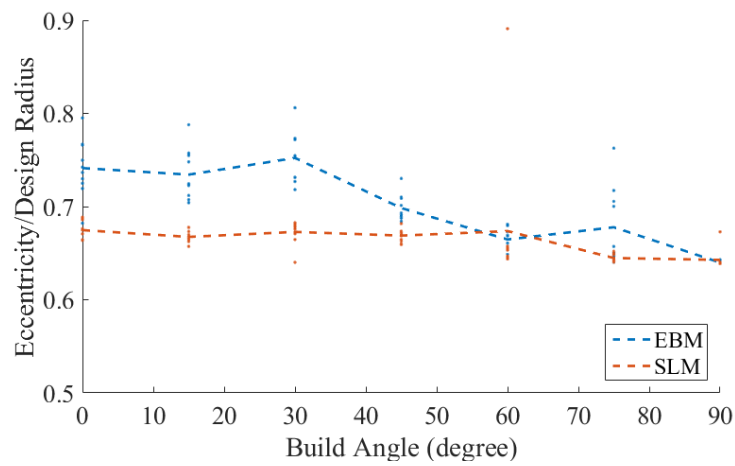
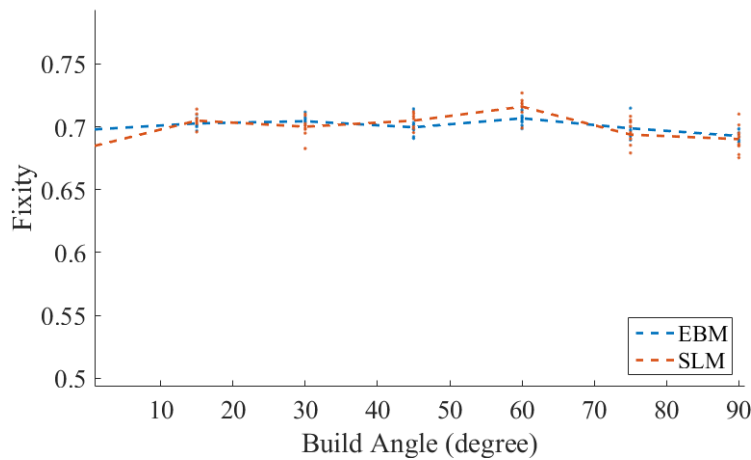


Figure 6-19 Change in radius due to AM process

The joint related structural element parameters at each angle are presented in Figure 6-20. The fixity is insensitive to the build angle, whereas the eccentricity decreases as the build angle increases. This implies that joints have more impact on structural behaviors in the low build angles. Since both joint and strut regions are deposited simultaneously in the low build angle, a joint fabricated in the low build angle are stiffer than a joint in the high build angle, which is affected by stair stepping. All things considered, an increase in build angle stiffens the strut regions but limits the joint regions.



(a) Eccentricity



(b) Fixity

Figure 6-20 Structural element parameters with varying build angles

6.5 Chapter Summary

In this chapter, the structural element parameters were explained and were selected to describe two regions in a strut, such as frame and joint regions. The semi-rigid joint frame element was formulated to model a strut in cellular materials. The effective structural element parameters were determined by approximating the structural behavior of as-fabricated voxel models.

To investigate the effect of the AM process on structural element parameters, parametric studies were performed for two AM processes. The results of the material extrusion process draw three points: (1) the bigger joint shape yields larger joint-related structural parameters, (2) the build angle has influence on structural element parameters but the effects of the raster angle are limited, and (3) the manufacturing instabilities degrade the effective strut diameter. Two points are inferred from the results of the powder bed fusion process: (1) the effective strut diameter is affected by powder morphology, and (2) the effective strut diameter is larger as the build angle increases, whereas joint related structural element parameters are reduced as the build angle increases.

The remaining part of Research question 2 is now answered: the propagation of geometrical and material variation can be captured quantitatively by determining the structural element parameters based on the displacement fields obtained by analyzing the as-fabricated voxel model. The resulting structural element parameters are used in discrete homogenization procedures in the next chapter.

CHAPTER 7 Property Estimation Procedure for Cellular Material

This chapter presents a homogenization procedure for estimating the mechanical properties of a cellular solid material. The goal of this chapter is to address research issues in Research question 3. In order to achieve the goal, the semi-rigid joint frame element derived in the previous chapter is integrated with the proposed discrete homogenization approach. Two mechanical properties, elastic modulus and yield strength, are investigated. The estimates from the proposed method are compared with test results for validation.

7.1 Discrete Homogenization Approach

Since a cellular material is comprised of many structural members such struts and walls, its complex geometries make it time-consuming and computing resource intensive to model and analyze. One approach to overcome this problem is to replace a cellular material with homogenized media that has equivalent mechanical properties. This procedure is called as homogenization. Figure 7-1 represents conceptual explanation of the homogenization approach. The mathematical theory of homogenization has been developed for a heterogeneous material with periodic microstructures. A fundamental concept of the homogenization approach is that the mechanical characteristics of microstructures govern the macroscopic mechanical properties of a heterogeneous media. Thus, equivalent mechanical properties are derived by analyzing a representative unit cell of a medium in a homogenization approach. This approach can be applied to a cellular material because it can be considered as a heterogeneous material, which is a mixture of

solid materials and voids. In this research, a cellular material is assumed to be a regular lattice structure whose representative unit cell is repeated along the periodic direction.

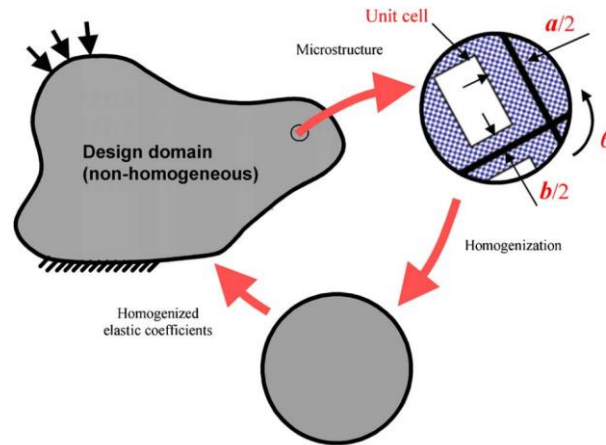


Figure 7-1 Homogenization approach[92]

Various homogenization methods have been proposed to derive the equivalent mechanical properties of periodic cellular materials, as discussed in Chapter 2. Conventional homogenization approaches apply expansion schemes, such as the Taylor's or asymptotic expansion, in order to express physical quantities and to formulate a self-equilibrium equation that is used to analyze a representative unit cell. The conventional approaches have two disadvantages for application to additively manufactured cellular material. The first is that they require a detailed geometrical model of a unit cell, which is not easy to modify in order to include manufacturing effects in the model. The second is that the numerical procedure is computationally cost-intensive. Since the unit cell model is discretized by a large number of elements to increase accuracy, much computational resource is required. Moreover, applying periodic conditions to the model is complicated for periodicity defined in the non-Cartesian coordinate. To mitigate these problems, this

research implements and modifies a discrete homogenization approach proposed by Vigliotti and Pasini [74]. Since this approach utilizes structural elements such as a beam and a truss to model a representative unit cell, its modeling procedure is simple, and manufacturing effects can be incorporated into the modeling procedure by adjusting relevant parameters. Moreover, the numerical procedure for this approach reduces the computational cost. The approach can utilize structural elements, such as truss, beam and plate elements. This reduces significantly the needed computational resources. Furthermore, since periodic vectors define the periodicity, periodic boundary conditions are easily imposed.

In the discrete homogenization approach, a representative unit cell of a lattice structure is modeled using nodes and edges as shown in Figure 7-2. A set of periodic vectors that represent the periodicity of a lattice structure is constructed, as shown in Figure 7-2 (a). Its edges describe strut connectivity among nodes. Any edges duplicated due to periodicity are excluded in the unit cell definition, as described in Figure 7-2 (c). A node represents an end-point of a strut. Two classes of nodes in a unit cell are defined: independent and dependent nodes. Figure 7-2 (c) presents node classification in a cubic unit cell. Independent nodes are the reference nodes from which dependent nodes are positioned and oriented. The position of a dependent node is expressed by adding position vectors of corresponding independent nodes to integer multiples of periodic direction vectors. All internal nodes are independent, but some boundary nodes are independent and other boundary nodes are dependent. In the definition of a unit cell, the designer can identify any convenient node as the independent node. For example, in a cubic unit cell in Figure 7-2 (c), the node at the bottom-left corner is selected as the

independent node for convenience, and other nodes can be positioned relative to this one. Figure 7-3 shows various unit cell definitions. Red and blue nodes are independent and dependent nodes, respectively.

A fundamental concept of the discrete homogenization is to equate target macroscopic physical quantities to corresponding microscopic physical quantities in a representative unit cell. For example, a displacement field of a lattice structure, a primary physical quantity, is expressed by change in periodic vectors. Therefore, the homogenized mechanical properties can be determined in terms of microscopic parameters such as strut diameter and length. Figure 7-4 presents an overview of the presented approach for determining an equivalent elastic constitutive matrix.

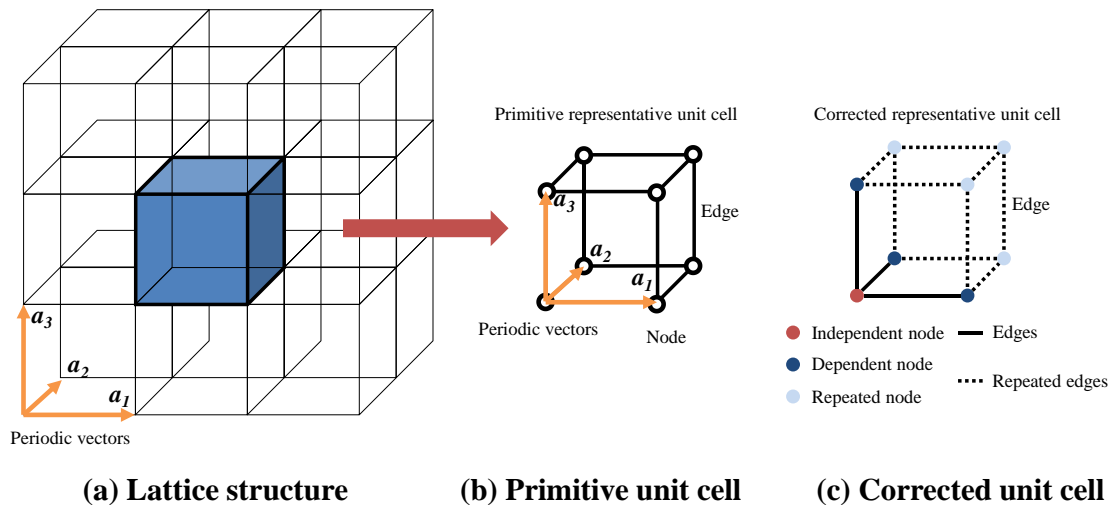


Figure 7-2 Definition of representative unit cell

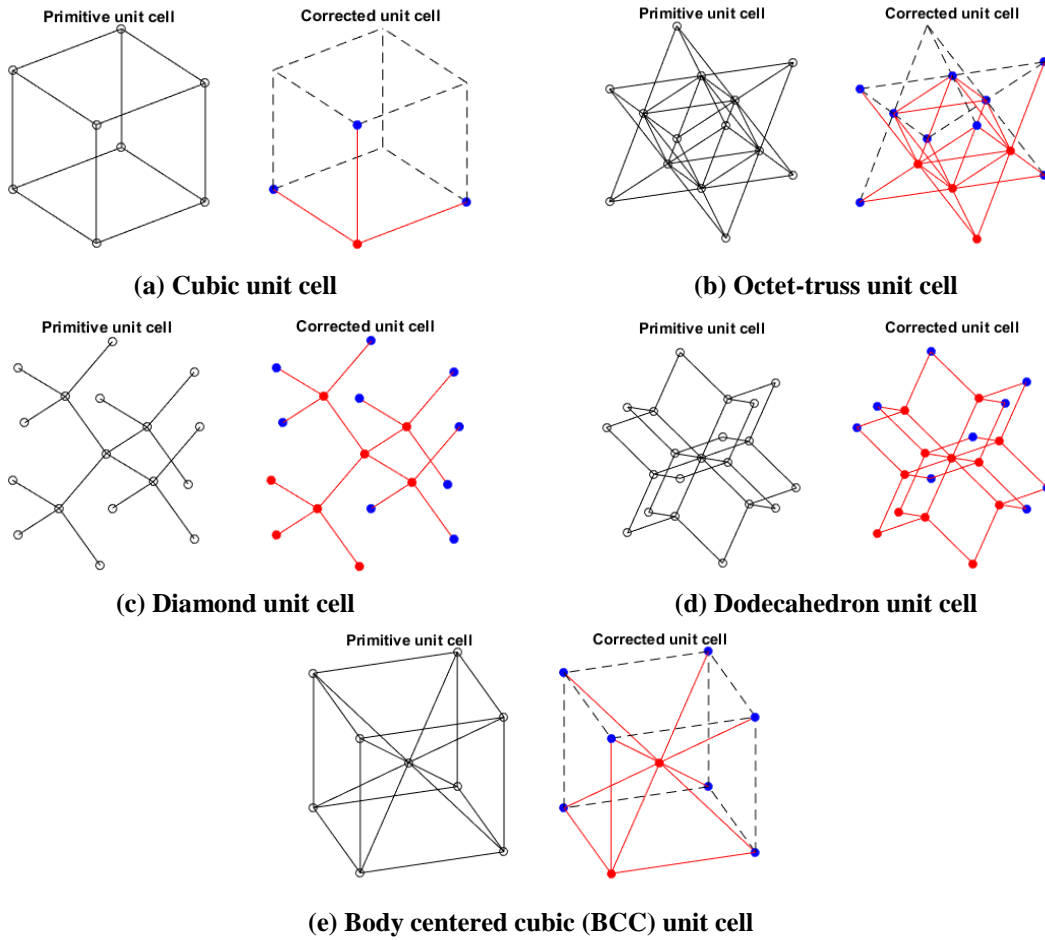


Figure 7-3 Example of unit cell definition

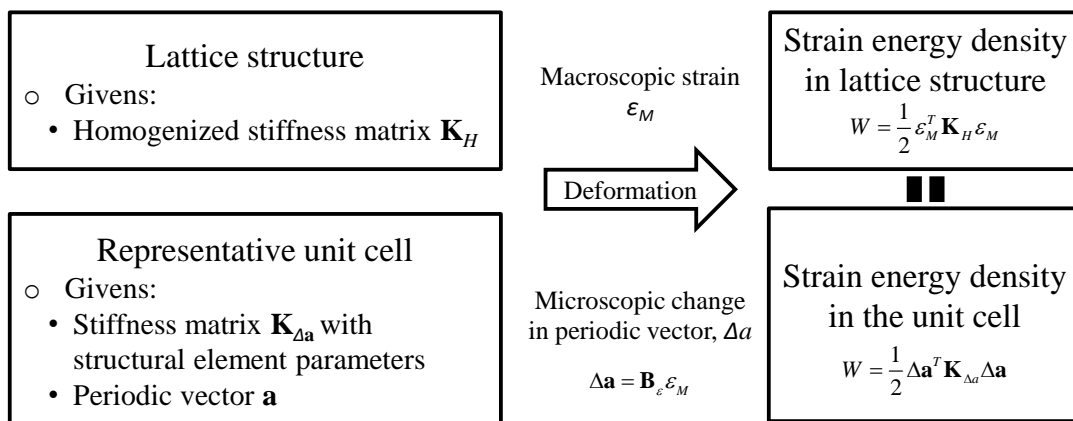


Figure 7-4 Overview of discrete homogenization method for elastic constitutive matrix

7.2 Derivation of Homogenized Mechanical Properties

7.2.1 Homogenized Elastic Modulus and Poisson's Ratio

The elastic modulus and Poisson's ratio are the most important mechanical properties in order to assess the elastic behavior of a cellular material. These properties can be determined by comparing stored strain energy in both scales after deformation. In order to derive the strain energy in both scales, the procedure starts by defining the relative position and displacement vectors at each node in the representative unit cell based on periodicity. The position of an arbitrary node in the lattice structure is represented as follows:

$$\mathbf{r}_k = \mathbf{r}_m + \sum_{i=1}^p n_i \mathbf{a}_i \quad (7.1)$$
$$\begin{cases} k \in \{1, \dots, N\} \\ m \in \{m_1, \dots, M\} \\ p \in \{1, 2, 3\} \end{cases}$$

where, \mathbf{r}_k is a position vector of the k^{th} node and \mathbf{r}_m is a position vector of its corresponding independent node. \mathbf{a}_i is a periodic direction vector and n_i is the corresponding integer multiplier that counts the number of periods between the k^{th} node and its corresponding independent node. The numbers N and M represent the total number of nodes and independent nodes, respectively. The number p means the number of periodic vectors, which can be up to three in a three dimensional lattice structure. The subscript m indicates the corresponding independent node number of the k^{th} node and the

subscript k indexes over all nodes in the unit cell. A translational displacement vector at the k^{th} node is expressed as:

$$\mathbf{u}_k = \mathbf{u}_m + \sum_{i=1}^p n_i \Delta \mathbf{a}_i \quad (7.2)$$

where, \mathbf{u}_k is a translational displacement vector at the k^{th} node and \mathbf{u}_m is a translational displacement vector of the corresponding reference node. $\Delta \mathbf{a}_i$ is the deformation in periodic vectors.

In this approach, we implemented the finite element method using semi-rigid frame elements in order to analyze the unit cell. Thus, six nodal DOFs are assumed at each node, including rotational displacement components in addition to translational displacement components. The displacement vector at each node is substituted by \mathbf{d}_i instead of \mathbf{u}_i , which is represented as $\mathbf{d}_i = [u_i \quad v_i \quad w_i \quad \theta_i \quad \phi_i \quad \psi_i]^T$. Using this notation, Equation (7.2) is rewritten as the following:

$$\mathbf{d}_k = \mathbf{d}_m + \sum_{i=1}^p \begin{bmatrix} n_i \mathbf{I} \\ \mathbf{0} \end{bmatrix} \Delta \mathbf{a}_i = \mathbf{d}_m + \sum_{i=1}^p n_i \mathbf{I}_i \Delta \mathbf{a}_i \quad (7.3)$$

where, \mathbf{I} and $\mathbf{0}$ are a 3×3 identity matrix and a 3×3 zero matrix, respectively. \mathbf{I}_i is a block matrix composed of \mathbf{I} and $\mathbf{0}$, whose dimension is 6×3 . The block matrices are used for matching dimensions between \mathbf{d} and $\Delta \mathbf{a}$. In the following, n_i is set to zero or one because only one presentative unit cell is considered in this formulation. n_i is zero

for an independent node, or n_i is determined by nodal dependency on its reference node.

For deriving global finite element equations, a total nodal displacement vector that is a collection of all nodal displacements in the unit cell is defined as the following:

$$\mathbf{d} = \begin{bmatrix} \mathbf{d}_1 \\ \vdots \\ \mathbf{d}_N \end{bmatrix} \quad (7.4)$$

where, \mathbf{d} is the total nodal displacement vector. Similarly, a total independent nodal displacement vector is defined as follows:

$$\mathbf{d}_0 = \begin{bmatrix} \mathbf{d}_{m_1} \\ \vdots \\ \mathbf{d}_M \end{bmatrix} \quad (7.5)$$

where, \mathbf{d}_0 is the total independent nodal displacement vector. The total deformation in the periodic direction vectors is constructed as the following:

$$\Delta \mathbf{a} = \begin{bmatrix} \Delta \mathbf{a}_1 \\ \vdots \\ \Delta \mathbf{a}_p \end{bmatrix} \quad (7.6)$$

where, $\Delta \mathbf{a}$ is a total deformation vector of the periodic vector. Using Equations (7.3) - (7.6), the total nodal displacement vector is expressed as the following:

$$\mathbf{d} = \mathbf{B}_0 \mathbf{d}_0 + \mathbf{B}_a \Delta \mathbf{a} \quad (7.7)$$

where, \mathbf{B}_0 and \mathbf{B}_a are block matrices that define nodal dependency and nodal periodicity. \mathbf{B}_0 expresses the dependencies among nodal displacements and \mathbf{B}_a relates dependent nodes to their reference independent nodes. Both \mathbf{B}_0 and \mathbf{B}_a consist of identity and zero sub-matrices. The matrices for various unit cell topologies are provided in Appendix B. For the cubic unit cell in Figure 7-3 (a), the matrices are derived as follows:

$$\mathbf{B}_0 = \begin{bmatrix} \mathbf{I} \\ \mathbf{I} \\ \mathbf{I} \\ \mathbf{I} \end{bmatrix} \quad (7.8)$$

$$\mathbf{B}_a = \begin{bmatrix} \mathbf{0} & \mathbf{0} & \mathbf{0} \\ \mathbf{I}_t & \mathbf{0} & \mathbf{0} \\ \mathbf{0} & \mathbf{I}_t & \mathbf{0} \\ \mathbf{0} & \mathbf{0} & \mathbf{I}_t \end{bmatrix} \quad (7.9)$$

where, \mathbf{I} is a 6×6 identity matrix and $\mathbf{0}$ is a 6×3 zero matrix.

The next step is to formulate the static equilibrium expression for the periodic lattice structure using the finite element analysis. The static equilibrium equation without consideration of periodicity is written as follows:

$$\mathbf{K}_{uc} \mathbf{d} = \mathbf{F}_{uc} \quad (7.10)$$

where, \mathbf{K}_{uc} and \mathbf{F}_{uc} are an unconstrained total stiffness matrix and an unconstrained total force vector, respectively. In order to construct the stiffness matrix, semi-rigid joint frame elements are implemented.

In the deformed configuration, the resultant force applied by surrounding edges at each node must be zero. Due to the periodicity of the lattice structure, the equilibrium equation can be represented by nodal forces in the unit cell using \mathbf{B}_0 in Equation (7.7) as follows:

$$\mathbf{B}_0^T \mathbf{K}_{uc} \mathbf{d} = \mathbf{B}_0^T \mathbf{F}_{uc} = \mathbf{0} \quad (7.11)$$

Substituting Equation (7.7) into Equation (7.11), the self-equilibrium equation is derived in terms of an independent nodal displacement vector as follows:

$$\mathbf{B}_0^T \mathbf{K}_{uc} \mathbf{B}_0 \mathbf{d}_0 = -\mathbf{B}_0^T \mathbf{K}_{uc} \mathbf{B}_a \Delta \mathbf{a} \quad (7.12)$$

Since the unconstrained stiffness matrix is singular in Equation (7.12), it cannot be solved by implementing conventional solution techniques. Thus, one of the non-unique solution techniques is applied, which multiplies a pseudo-inverse at both sides to determine a non-unique solution as follows:

$$\mathbf{d}_0 = -\left(\mathbf{B}_0^T \mathbf{K}_{uc} \mathbf{B}_0\right)^+ \mathbf{B}_0^T \mathbf{K}_{uc} \mathbf{B}_a \Delta \mathbf{a} = \mathbf{D}_0 \Delta \mathbf{a} \quad (7.13)$$

where, $(\bullet)^+$ denotes the Moore-Penrose pseudo-inverse, which yields a least square solution [93]. After substituting Equation (7.13) into Equation (7.7), the total displacement vector is calculated as the following:

$$\mathbf{d} = (\mathbf{B}_0 \mathbf{D}_0 + \mathbf{B}_a) \Delta \mathbf{a} = \mathbf{D}_a \Delta \mathbf{a} \quad (7.14)$$

Equation (7.14) relates the deformation of the periodic vectors to the nodal displacement. The deformation of periodic vectors is directly related to macroscopic deformation. The deformation can be evaluated using the macroscopic strain field as:

$$\Delta \mathbf{a} = \mathbf{a}' - \mathbf{a} = (\mathbf{I} + \boldsymbol{\varepsilon}_M) \mathbf{a} - \mathbf{a} = \boldsymbol{\varepsilon}_M \mathbf{a} \quad (7.15)$$

$$\begin{Bmatrix} \Delta a_x^i \\ \Delta a_y^i \\ \Delta a_z^i \end{Bmatrix} = \begin{bmatrix} \varepsilon_{xx} & \gamma_{xy} & \gamma_{xz} \\ \gamma_{xy} & \varepsilon_{yy} & \gamma_{yz} \\ \gamma_{xz} & \gamma_{yz} & \varepsilon_{zz} \end{bmatrix} \begin{Bmatrix} a_x^i \\ a_y^i \\ a_z^i \end{Bmatrix} \quad (7.16)$$

where, \mathbf{a}' is a deformed periodic vector and $\boldsymbol{\varepsilon}_M$ is a macroscopic strain tensor of a lattice structure. After rewriting the strain tensor in vector-form using the Voigt notation, Equation (7.15) is represented as follows:

$$\Delta \mathbf{a} = \mathbf{B}_\varepsilon \mathbf{e}_M \quad (7.17)$$

$$\Delta \mathbf{a}^i = \mathbf{B}_\varepsilon^i \mathbf{e}_M = \begin{bmatrix} a_x^i & 0 & 0 & 0 & a_z^i & a_y^i \\ 0 & a_y^i & 0 & a_z^i & 0 & a_x^i \\ 0 & 0 & a_z^i & a_y^i & a_x^i & 0 \end{bmatrix} \begin{Bmatrix} \varepsilon_{xx} \\ \varepsilon_{yy} \\ \varepsilon_{zz} \\ \gamma_{yz} \\ \gamma_{xz} \\ \gamma_{xy} \end{Bmatrix} \quad (7.18)$$

where, \mathbf{e}_M is a macroscopic strain vector and \mathbf{B}_ε is a conversion matrix from the macroscopic strain to the periodic vector. Substituting Equation (7.17) into Equation (7.14), the total displacement vector in a representative unit cell is represented by macroscale strain as below:

$$\mathbf{d} = \mathbf{D}_\varepsilon \mathbf{B}_\varepsilon \mathbf{e}_M = \mathbf{D}_\varepsilon \mathbf{e}_M \quad (7.19)$$

where, \mathbf{D}_ε is a conversion matrix from the macroscopic strain to the total nodal displacement vector.

The strain energy stored in a unit cell after deformation can be represented using the total nodal displacement vector in Equation (7.19) as follows:

$$W = \frac{1}{2V} \mathbf{d}^T \mathbf{K}_{uc} \mathbf{d} = \frac{1}{2V} \mathbf{e}_M^T \mathbf{B}_\varepsilon^T \mathbf{D}_a^T \mathbf{K}_{uc} \mathbf{D}_a \mathbf{B}_\varepsilon \mathbf{e}_M = \frac{1}{2V} \mathbf{e}_M^T \mathbf{D}_\varepsilon^T \mathbf{K}_{uc} \mathbf{D}_\varepsilon \mathbf{e}_M \quad (7.20)$$

where, V is the volume of a unit cell.

The stain energy can be also represented using the macroscale strain field and the homogenized stiffness matrix as follows:

$$W = \frac{1}{2} \mathbf{e}_M^T \mathbf{K}_H \mathbf{e}_M \quad (7.21)$$

where, \mathbf{K}_H is the homogenized stiffness matrix. By comparing Equation (7.20) with Equation (7.21), the homogenized stiffness matrix is derived as follows:

$$\mathbf{K}_H = \frac{1}{V} \mathbf{D}_\varepsilon^T \mathbf{K}_{uc} \mathbf{D}_\varepsilon \quad (7.22)$$

In this research, it is assumed that a periodic cellular material is an orthotropic material, which has the following compliance matrix:

$$S = \mathbf{K}_H^{-1} = \begin{bmatrix} \frac{1}{E_1} & -\frac{\nu_{21}}{E_2} & -\frac{\nu_{31}}{E_3} & 0 & 0 & 0 \\ -\frac{\nu_{12}}{E_1} & \frac{1}{E_2} & -\frac{\nu_{32}}{E_3} & 0 & 0 & 0 \\ -\frac{\nu_{13}}{E_1} & -\frac{\nu_{23}}{E_2} & \frac{1}{E_3} & 0 & 0 & 0 \\ 0 & 0 & 0 & \frac{1}{G_{23}} & 0 & 0 \\ 0 & 0 & 0 & 0 & \frac{1}{G_{31}} & 0 \\ 0 & 0 & 0 & 0 & 0 & \frac{1}{G_{12}} \end{bmatrix} \quad (7.23)$$

Based on Equation (7.23), the equivalent elastic modulus and Poisson's ratio can be extracted.

7.2.2 Homogenized Yield Strength

A homogenized yield strength of cellular material is defined as the maximum effective stress on a unit cell that initiates yielding at any structural member in a unit cell. In the proposed homogenization approach, a microscopic total nodal displacement vector, \mathbf{u}_k , can be expressed by a macroscopic strain vector, \mathbf{e}_M , acting on a lattice structure. The microscopic displacement field yields internal strut forces and stresses that can result in a microscopic yield of struts. In this research, the macroscopic stress that leads to the first microscopic yield among struts is defined as the homogenized yield strength.

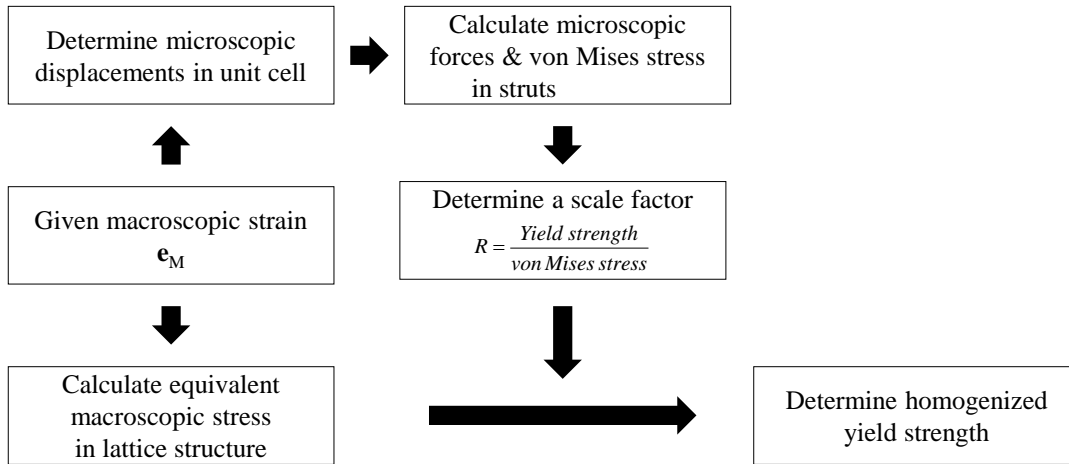


Figure 7-5 Overall procedure for homogenized yield strength

The overall procedure for determining the homogenized yield strength is represented in Figure 7-5. The procedure starts with determining a total displacement vector for a given macroscopic strain field. To mimic a tensile test, the macroscopic strain field is given as the following:

$$\begin{aligned}
\mathbf{e}_M^x &= \{\varepsilon_{xx} \quad 0 \quad 0 \quad 0 \quad 0 \quad 0\}^T \text{ for } x\text{-direction} \\
\mathbf{e}_M^y &= \{0 \quad \varepsilon_{yy} \quad 0 \quad 0 \quad 0 \quad 0\}^T \text{ for } y\text{-direction} \\
\mathbf{e}_M^z &= \{0 \quad 0 \quad \varepsilon_{zz} \quad 0 \quad 0 \quad 0\}^T \text{ for } z\text{-direction}
\end{aligned} \tag{7.24}$$

where, ε_{xx} , ε_{yy} and ε_{zz} are macroscopic strains in the x, y and z directions, respectively.

In this research, the macroscopic strains are set to unity for simplification. For given macroscopic strain fields, the microscopic total displacement vector is calculated using Equation (7.19) as follows:

$$\mathbf{d} = \mathbf{D}_a \mathbf{B}_\varepsilon \mathbf{e}_M^x = \mathbf{D}_\varepsilon \mathbf{e}_M^x = \mathbf{D}_\varepsilon \begin{Bmatrix} 1 \\ 0 \\ 0 \\ 0 \\ 0 \\ 0 \end{Bmatrix} \text{ for } x\text{-direction} \tag{7.25}$$

Next, elemental displacement vectors are extracted from the microscopic displacement vector. The elemental force vectors are determined using the element equilibrium equation as follows:

$$\mathbf{F}_e = \mathbf{K}_e \mathbf{d}_e \tag{7.26}$$

where, \mathbf{F}_e and \mathbf{d}_e are an elemental force vector and a displacement vector. \mathbf{K}_e is an elemental stiffness matrix. The elemental vectors are defined in the elemental coordinates as shown in Figure 7-6. The subscripts 1, 2 and 3 represent the axial direction and two

lateral directions, respectively. The elemental force vector can be represented as the following:

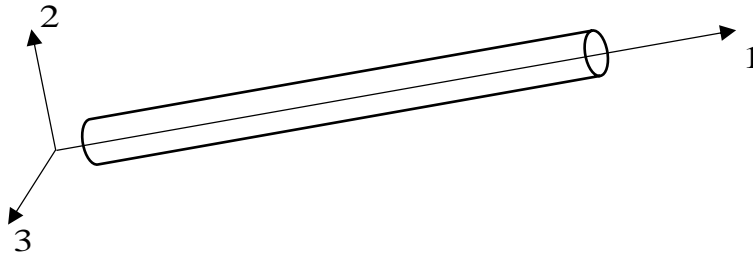


Figure 7-6 Elemental coordinates in a strut

$$F = \begin{Bmatrix} F_1 \\ V_2 \\ V_3 \\ T_1 \\ M_2 \\ M_3 \end{Bmatrix} \quad (7.27)$$

where, F_1 , V_2 and V_3 are axial and two shear forces, respectively, and T_1 , M_2 and M_3 are the torsional moment and two bending moments.

Next, the von Mises stresses in the struts are determined using elemental force components as the following:

$$\begin{aligned}
\sigma_{11}^e &= \frac{F_1}{A_e} + \frac{M_2 r}{I_{33}} + \frac{M_3 r}{I_{22}} \\
\tau_{12}^e &= \frac{V_2}{A_e} + \frac{T_1 r}{J_p} \\
\tau_{13}^e &= \frac{V_3}{A_e} + \frac{T_1 r}{J_p} \\
\sigma_v^e &= \sqrt{\sigma_{11}^{e2} + 3\tau_{12}^{e2} + 3\tau_{13}^{e2}}
\end{aligned} \tag{7.28}$$

where, σ_v is von Mises stress. I_{22} and I_{33} are the second moment of area and J_p is a polar moment of area. r is the radius of a strut. The scale factor is determined as follows:

$$R = \frac{\sigma_Y}{\text{Max}(\sigma_v)} \tag{7.29}$$

where, σ_Y is the yield strength of the raw material. R is a scale factor, which is a ratio between the largest von Mises value over all struts and the yield strength.

Next, the macroscopic stress is determined by post-multiplying the macroscopic strain vector to the homogenized stiffness matrix as the following:

$$\sigma_M = \mathbf{K}_H \mathbf{e}_M \tag{7.30}$$

where, σ_M represents the macroscopic stress.

Finally, the homogenized strength of the lattice structure is determined by multiplying the scale factor to the macroscopic stress as the following:

$$\sigma_Y^H = R\sigma_M \tag{7.31}$$

where, σ_Y^H is the homogenized strength.

7.3 Effects of Structural Element Parameters on Homogenized Properties

In order to study the effects of change in effective structural parameters on mechanical properties, parametric studies were performed on three types of unit cells presented in Figure 7-2 (a), (b) and (c). The range of the three structural element parameters is listed in Table 7-1. The unit cell size was set to 5 mm. The raw material was assumed as ABS-P400, whose elastic modulus and yield strength are 1627 MPa and 22 MPa.

Table 7-1 Selected structural parameters

Structural parameter	Range
Strut diameter	$0.5\text{ mm} \leq d_{\text{effective}} \leq 1.5\text{ mm}$
Fixity	$0 < \gamma < 1$
Eccentricity/radius	$0 < \frac{e}{r} < 1$

7.3.1 Elastic modulus

Figure 7-7, Figure 7-8 and Figure 7-9 present normalized elastic moduli calculated from the proposed discrete homogenization approach. Based on the results, two points can be inferred. Firstly, in all types of unit cells, as fixity and eccentricity increase, the lattice structures become stiffer. This means that the larger and stiffer the joint is, the stiffer the lattice structure is. The reason for the results is that the larger and stiffer joint

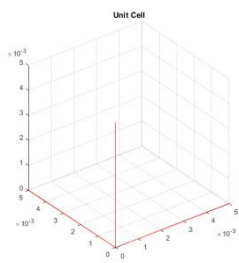
reduces total displacement or it increases internal reaction force. Moreover, the reduced strut length also increases the stiffness of the frame region. Thus, the increasing fixity and eccentricity make the lattice structure less flexible.

Next, a bending dominated lattice structure is more sensitive to variation in joint related parameters than a stretching dominated lattices structure. In this parametric study, the cubic unit cell that is aligned to the force direction and the octet-truss unit cell are stretching dominated. In contrast, the diamond unit cell is bending dominated. By contrasting the results from the cubic unit cell in Figure 7-7 and an octet-truss unit cell in Figure 7-9 with the diamond unit cell in Figure 7-8, the variation in the cubic and octet-truss unit cells due to change in fixity and eccentricity is smaller than the variation in the diamond unit cell. This can be explained by axial and flexural stiffness in the semi-rigid frame element. The stiffness can be presented as the following:

$$k_{Axial} = \frac{EA}{L} \quad (7.32)$$

$$k_{flexural} = \frac{EI}{L^3} \quad (7.33)$$

where, E , A and I are the elastic modulus, area, and the second moment of area, respectively. Equations (7.32) and (7.33) indicate that the stiffness is inversely proportional to the length of a strut. The flexural stiffness is more sensitive to the length because it is inversely proportional to L^3 . Therefore, a change in eccentricity alters the stiffness of the bending dominated unit cell more.



Cube

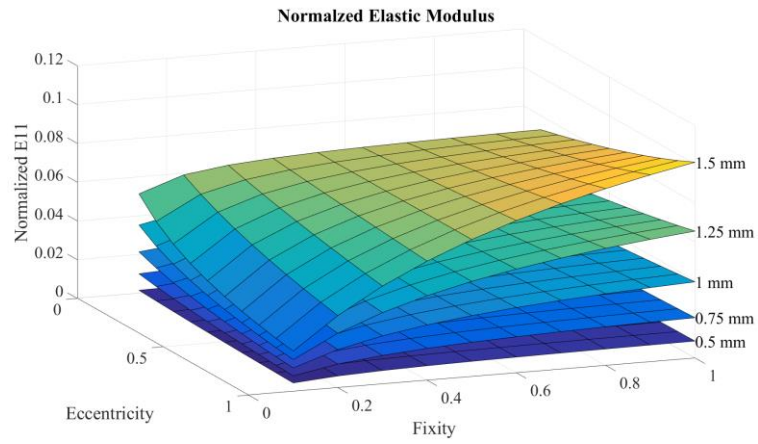
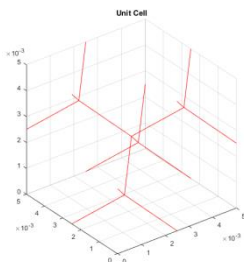


Figure 7-7 Elastic moduli of cubic unit cell



Diamond

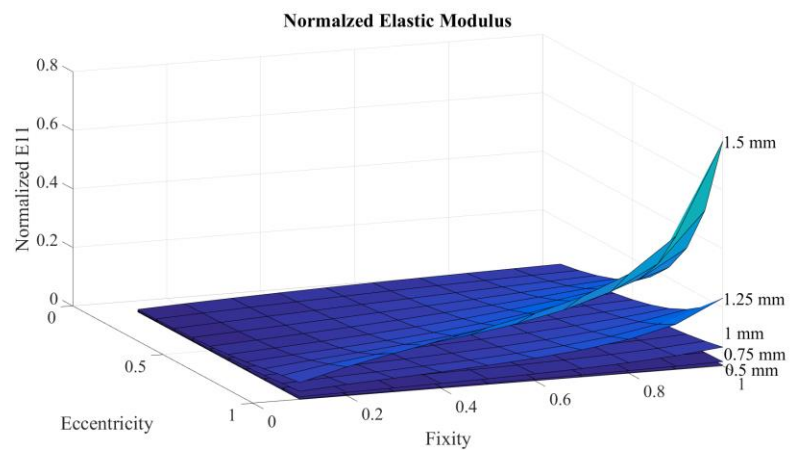
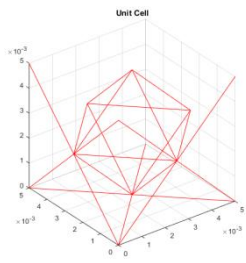


Figure 7-8 Elastic moduli of diamond unit cell



Octet-truss

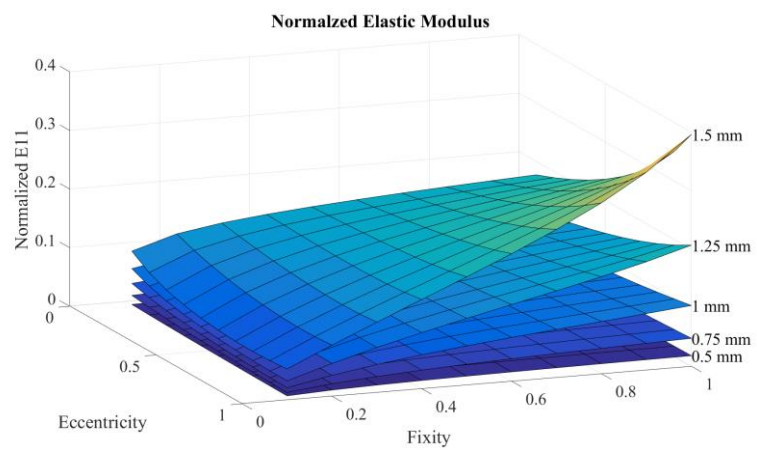


Figure 7-9 Change in elastic modulus for octet-truss lattice

7.3.2 Yield Strength

The yield strength of a cubic unit cell only depends on the strut diameter, as presented in Figure 7-10. Since the force in the joint is the same in the frame region, the joint properties do not affect the strength. Thus, the failure occurred when satisfying the failure criteria of the frame region, which is represented as follows:

$$\frac{F}{A} = \frac{4F}{\pi d^2} = \sigma_Y \quad (7.34)$$

The strength of the diamond unit cell and octet-truss unit cell is shown in Figure 7-11 and Figure 7-12, respectively. The trend of both results is complicated, since the yield strength is determined based on a ratio between maximum von Mises stress and homogenized stress that is the product of the effective elastic modulus and the macroscale strain. To understand the trend, the maximum von Mises stress variation among struts is presented in Figure 7-13. In both unit cells, as fixity and eccentricity increase, the resulting stress is increased. It is noteworthy that the amount of change in the diamond unit cell is larger than in the octet-truss unit cell. The reason for the difference is the same as mentioned in the previous section.

Comparing between von Mises stress and effective modulus, in the diamond unit cell, the change in effective modulus in the previous section is larger than the change in von Mises stress. Thus, the strength increase as the joint becomes larger. This can be explained that as joint size increases, the bending displacement and resulting stress is reduced. Accordingly, the resulting effective yield strength is increased. However, in the

octet-truss unit cell, the change is larger in the von Mises stress. Thus, the effective strength is slightly reduced as the joint becomes larger.

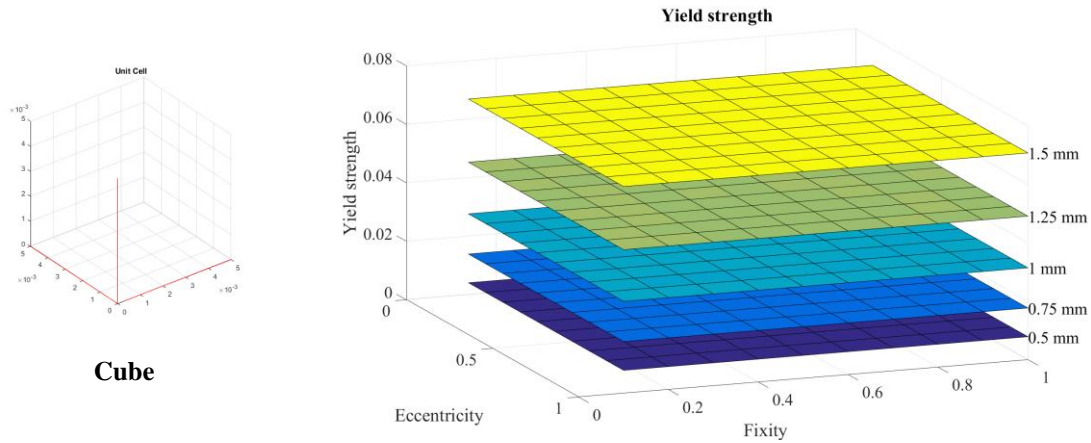


Figure 7-10 Yield strength of cubic unit cell

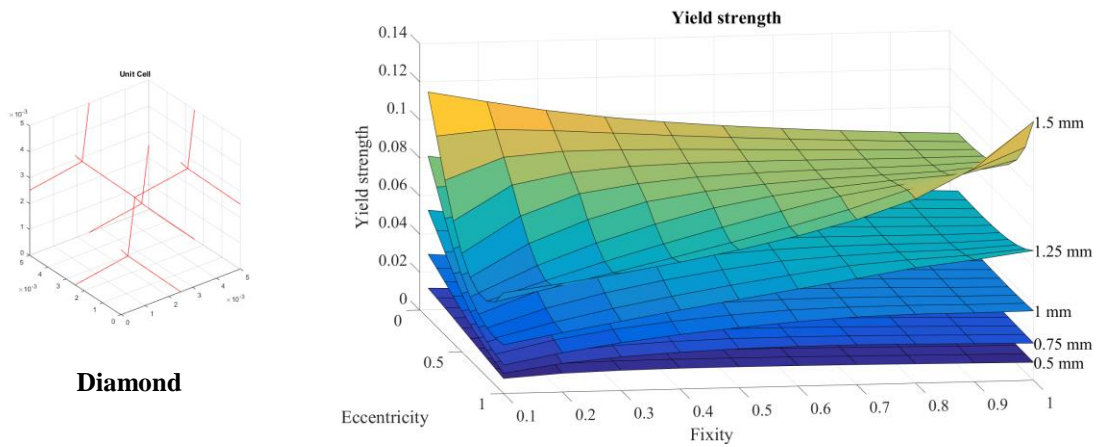


Figure 7-11 Yield strength of diamond unit cell

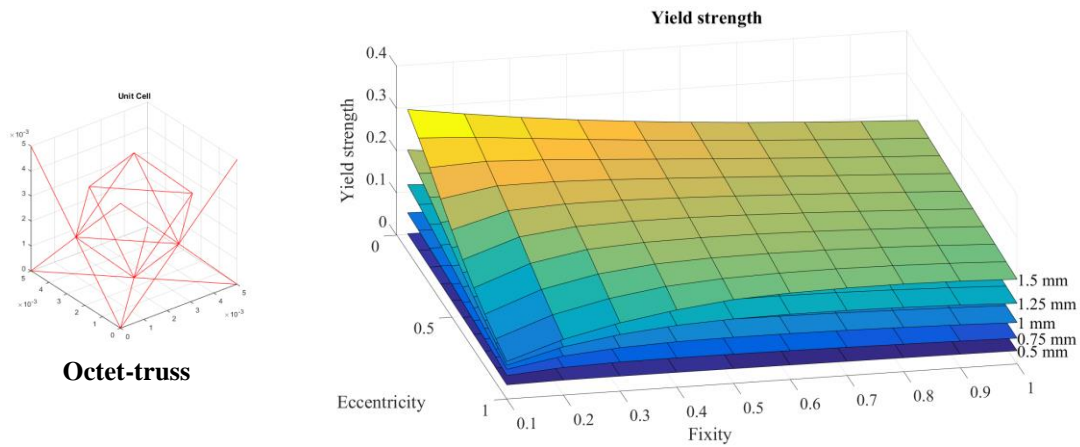


Figure 7-12 Yield strength of the octet-truss unit cell

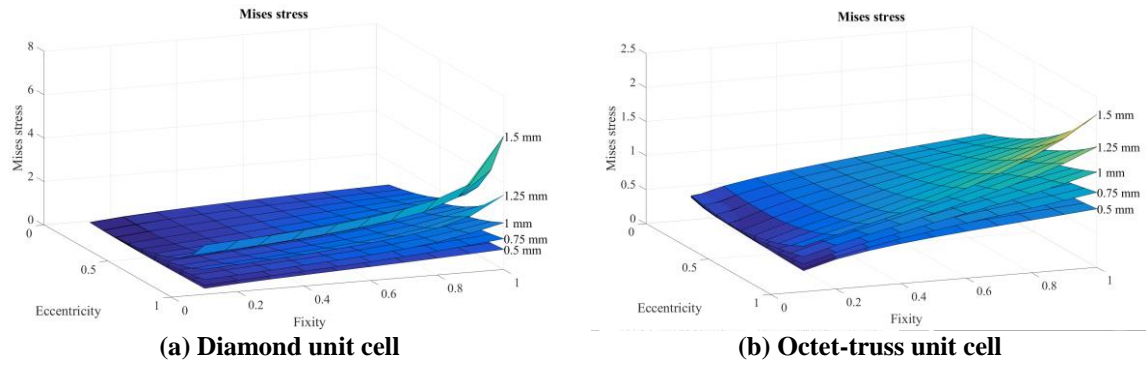


Figure 7-13 Maximum von Mises stress in struts

7.4 Validation of Homogenized Properties

7.4.1 Material Extrusion Process

In order to validate the proposed method, two sets of lattice structures were fabricated and tested. The obtained mechanical properties of the lattice structures were compared with estimates from the proposed discrete homogenization approach. The first set of lattices structures was designed to study the effect of unit cell topology. Three types of three-dimensional unit cells were fabricated and analyzed. The second set of lattice structures was intended for investigating the effect of the build angle. Two types of one-dimensional unit cells were selected. The first set of specimens was fabricated in the Fortus 400mc (Stratasys) with ABS M30 plastic material. An in-house tensile machine was used for tests. The second set of specimens was manufactured in the Dimension 1200es (Stratasys) using ABS P400 plastic material. Tensile tests were performed on the Instron universal test machine.

7.4.1.1 Unit Cell Topology

In order to validate the estimation procedure, two set of tensile specimens were fabricated and tested. The design of specimens is presented in Figure 7-14. In the first

batch of specimens, the cubic unit cells were embedded. The embedded unit cells were rotated to change the shape of the lattice structure. The specification of specimens is listed in Table 7-2. All cubic unit cell specimens have the same dimensions, but the direction of the unit cells' arrangement is different.

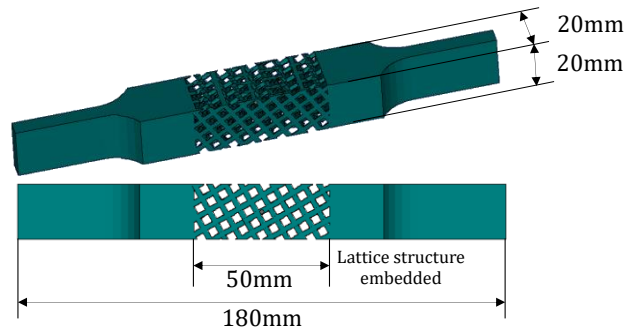
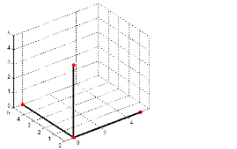

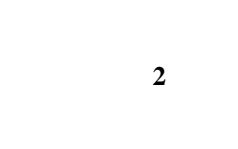
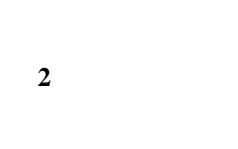


Figure 7-14 Design of specimens

Table 7-2 Specification of cubic type unit cell specimens

Specimen	Unit cell	Unit cell size (mm)	Strut diameter (mm)
1		5x5x5	2
2		5x5x5	2
3		5x5x5	2
4		5x5x5	2

In this section, four different homogenization approaches are implemented for comparison purpose: (1) the discrete homogenization approach with semi-rigid joint frame element that is proposed in this research, (2) the discrete homogenization approach with conventional Euler frame element, (3) the discrete homogenization approach with conventional shear flexible frame element, and (4) the asymptotic homogenization approach [94]. To implement semi-rigid frame elements for cubic unit cell specimens, the effective structural element parameters were set to the result of the parametric studies in Section 6.4. In the three other approaches, intact geometries are assumed.

The estimation results for elastic moduli are presented in Figure 7-15. The results are normalized with test results. The mean values of the test results are 230.06 MPa, 111.86 MPa, 49.39 MPa, and 54.17 MPa in the order of ascending build angle. In most rotation angles, the proposed discrete homogenization approach leads to accurate estimates. Euler frame implementation results in stiffer estimates while use of the shear flexible frame yields a more flexible elastic modulus. The result of the asymptotic homogenization approach leads to a large error except for the case of a 0° rotation angle. The approach overestimates the stiffness of lattice structures. Since the asymptotic homogenization approach utilizes solid elements that enables us to describe detailed geometries such as joints, intact geometries give additional stiffness to the lattice structure in the estimation process compared to degraded geometries. Therefore, the estimates were much stiffer than other estimates.

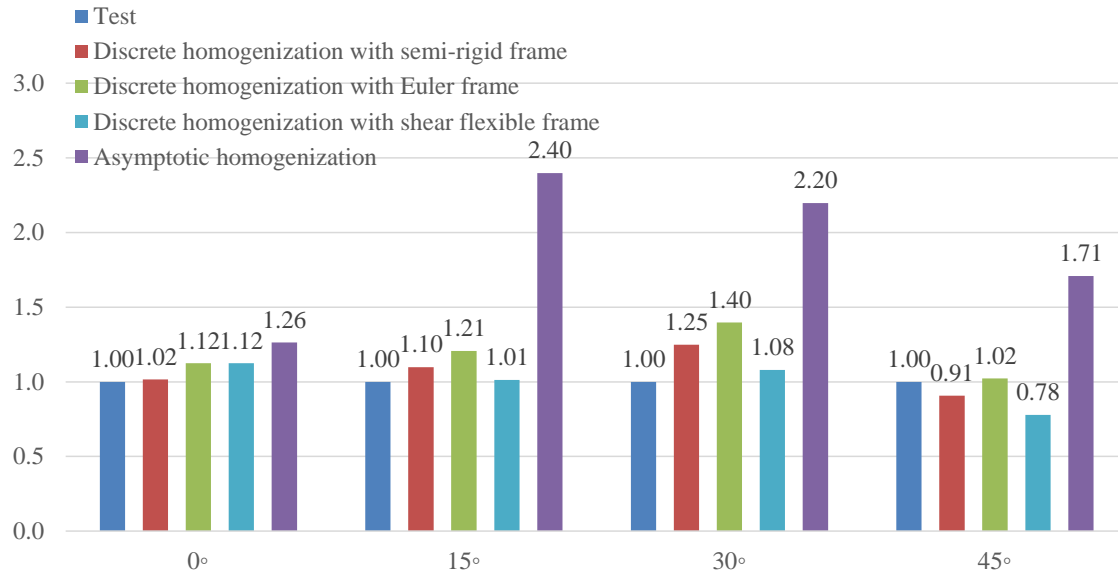


Figure 7-15 Comparison of elastic moduli in cubic unit cell

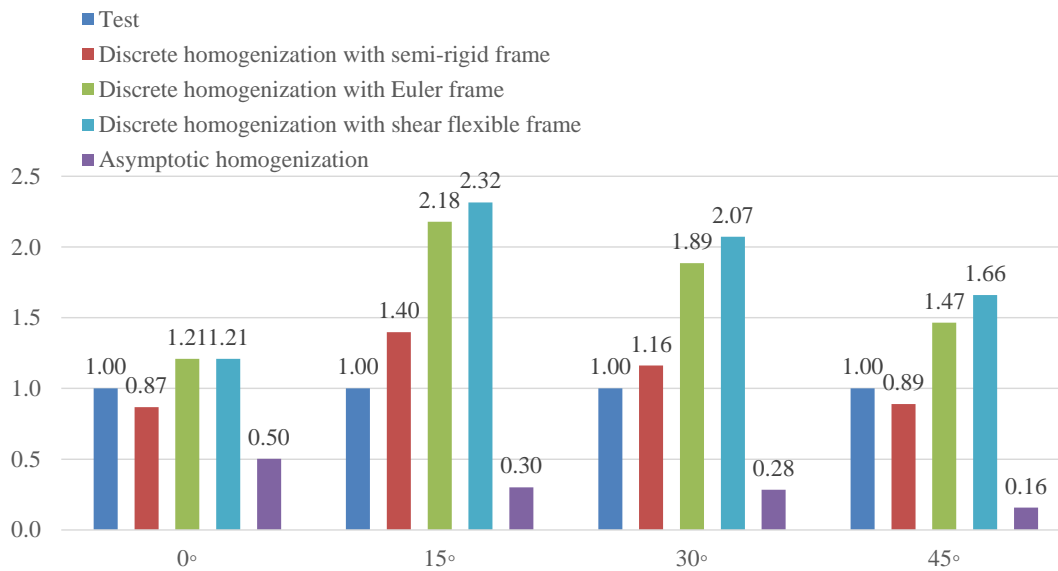


Figure 7-16 Comparison of yield strength in cubic unit cell

The estimated yield strength of the specimens is presented in Figure 7-16. The mean values of the test specimens are 2.57 MPa, 1.03 MPa, 0.87 MPa, and 1.08 MPa in the order of ascending build angle. The implementation of the semi-rigid joint frame

element reduced error significantly. Other homogenization approaches with Euler and shear flexible frame elements tend to extremely overestimate the strength of lattice structures by up to 2.32 times. This can be explained based on the bending stress in frame elements. The maximum bending stress is inversely proportional to the cubic power of the diameter as the following:

$$\sigma_{\max} = \frac{Mr}{I} = \frac{4M}{\pi r^3} \quad (7.35)$$

where M is the bending moment and I is the second moment of area. Since the intact diameter is applied to the Euler and shear flexible frames without considering degradation, the diameter is larger than the effective strut diameter, which is used in a semi-rigid frame. Therefore, the resulting estimated maximum stresses are smaller than estimates from the proposed method and as a result, the approaches overestimate the strength of the lattice structures.

However, the asymptotic homogenization approach significantly underestimates the yield strength by less than 84%. Since the asymptotic homogenization utilizes continuum elements such as tetrahedron and hexahedron elements and implements linear analysis, impractical stress concentration can be observed at sharp geometries where struts are connected to each other. This results in lowering the estimated yield strength.

In the second set of specimens, diamond and dodecahedron unit cells were embedded. The unit cell specification and design are presented in Table 7-3. In contrast to the cubic unit cell specimens, all diamond unit cell specimens are the same in cell topology but the dimensions are different. The fundamental shape of the strut is the same in all specimens. The mean values of test results are listed in Table 7-4.

Table 7-3 Specification of diamond type unit cell specimens

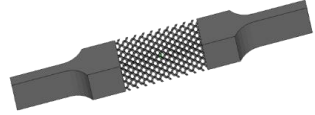
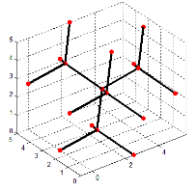
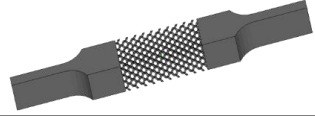
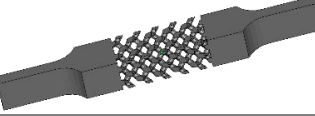
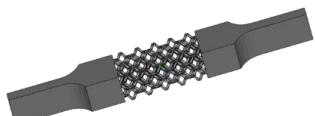
Specimen	Unit cell	Unit cell size (mm)	Strut diameter (mm)
1 		5x5x5	1
2 		5x5x5	1.5
3 		10x10x10	3
4 		10x10x10	1.5

Table 7-4 Mean value of obtained mechanical properties from tensile test

Unit: MPa	1	2	3	4
Elastic modulus	20.4	107.81	79.17	17.20
Yield strength	0.87	3.39	2.38	0.75

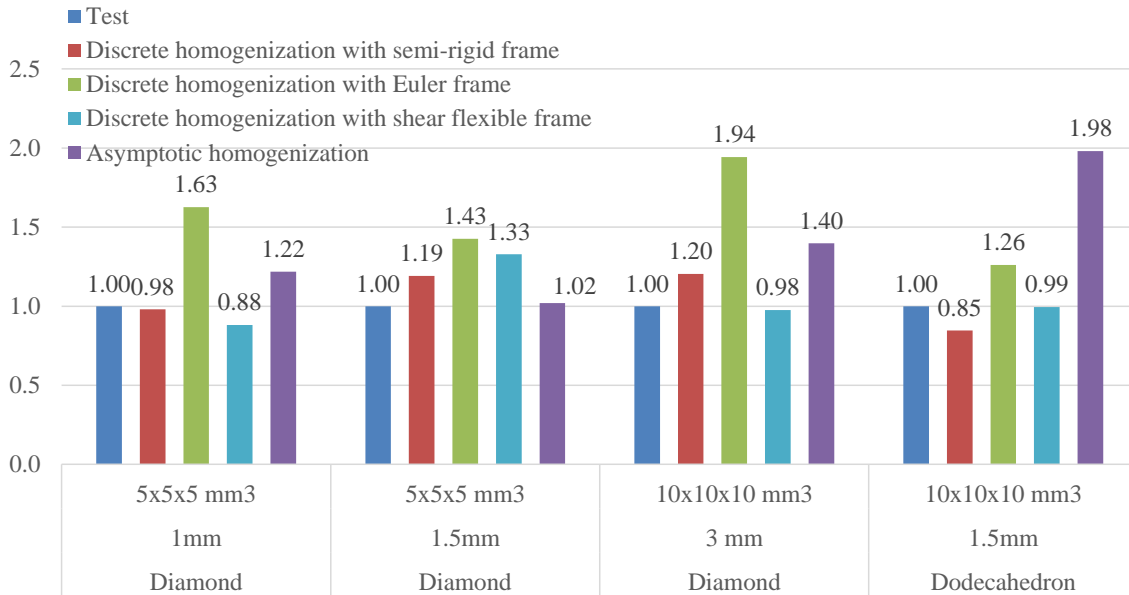


Figure 7-17 Comparison of elastic moduli in diamond and dodecahedron unit cell

The results of elastic moduli of the diamond unit cell specimens in Figure 7-17 show that the proposed method can estimate elastic modulus within $\pm 20\%$ error. The results imply that the proposed homogenization approach overestimates the elastic modulus, as the strut diameter is larger. In addition, the use of Euler frame elements for the diamond unit cells results in overestimation in the stiffness. Since the diamond unit cell is bending dominated and the struts have a low slenderness ratio, the Euler frame element, which ignores the deformation due to shear force, overestimates the stiffness. For the same reason mentioned in the previous section, the asymptotic homogenization approach provides larger values of elastic modulus.

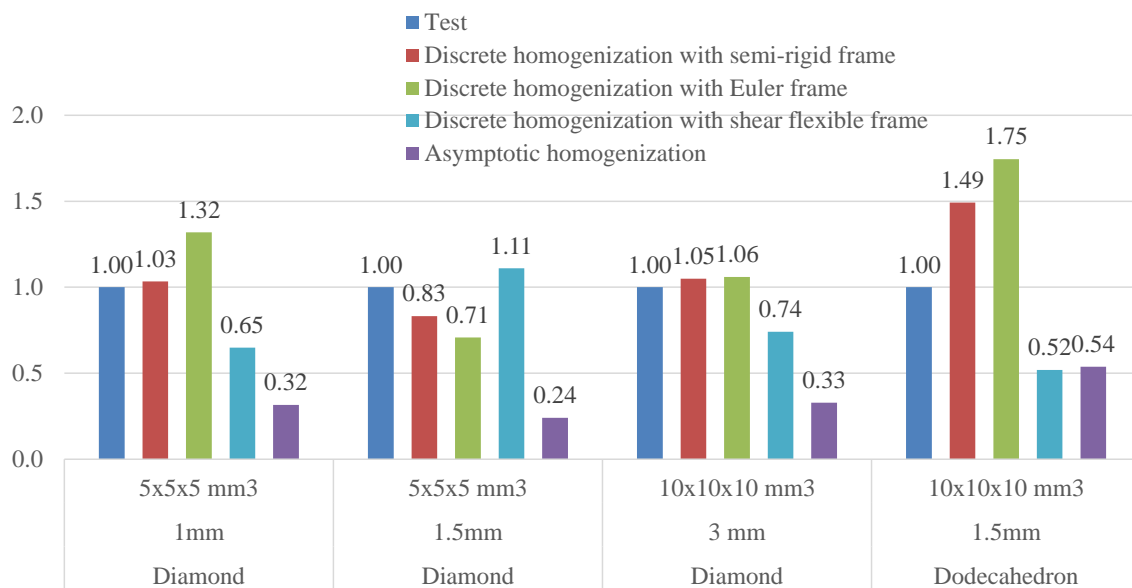


Figure 7-18 Comparison of yield strength in diamond and dodecahedron unit cell

Figure 7-18 compares estimated yield strength among estimation methods. The proposed method results in relatively small error in the range of $\pm 17\%$ for specimens with a diamond unit cell. However, estimates from other discrete homogenization

methods are fluctuated. This is because the intact geometries are used in the approaches, which cannot incorporate the AM process effect into the property-estimation processes.

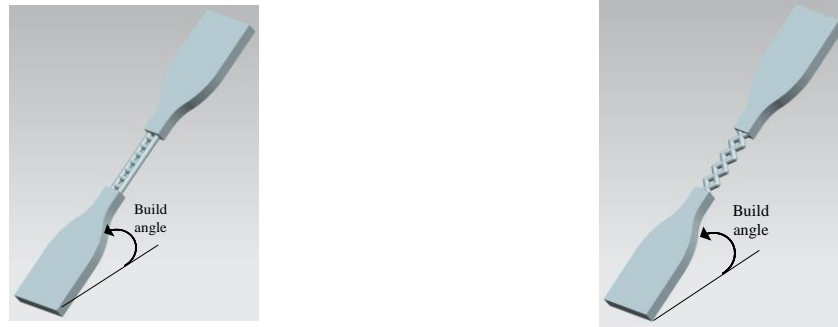
For specimens with dodecahedron unit cells, all estimation approaches show larger error compared to specimens with diamond unit cells. In discrete homogenization approach, stress concentration effect is not considered in failure criterion but the complex joint shape can yield stress concentration. Thus, the proposed method overestimates the strength. However, use of shear deformable frame without joint consideration leads to high maximum stress due to addition stress by shear deformation and, as a result, the strength is underestimated. The asymptotic homogenization significantly underestimates the strength due to stress concentration as the same reason in cubic unit cell specimens.

7.4.1.2 Effects of Build Angle

In order to investigate the effects of the build angle, two one-dimension lattice structure were embedded into ASTM type 4 specimens. The designs of the specimens are presented in Figure 7-19. Rectangular and crossed one-dimensional unit cells were selected for the parametric study. The specimens were fabricated with varying build angle. Five different angles (0° , 30° , 45° , 60° , 90°) for the rectangular unit cell and seven different build angles (0° , 15° , 30° , 45° , 60° , 75° , 90°) for the cross unit cell were used. Three tensile specimens were fabricated at each angle. The strut diameters and the strut lengths were set to 2 mm and 3.175 mm, respectively. The length of the embedded region was 22.86 mm.

The as-fabricated voxel model was generated to determine effective structural element parameters based on the default machine setting. The layer thickness and deposited filament width were set to 0.254 mm and 0.4445 mm, respectively. The

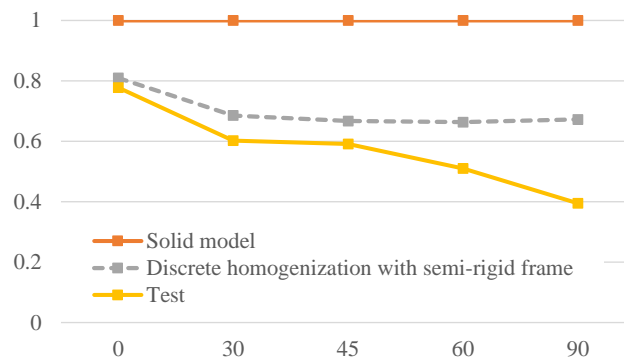
effective structural parameters were calculated from the voxel models, and the effective structural parameters were applied to the homogenization procedure.



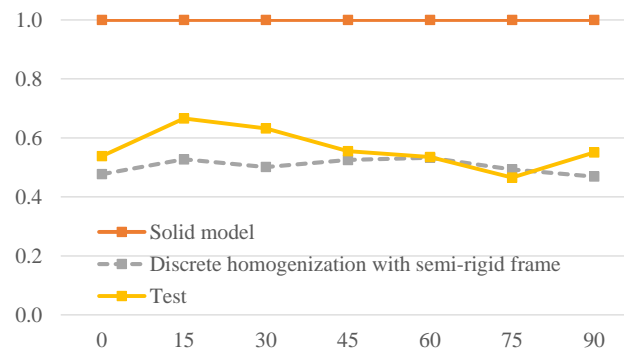
(a) Specimen 1: rectangular unit cell

(b) Specimen 2: cross unit cell

Figure 7-19 Design of 1D lattice specimens



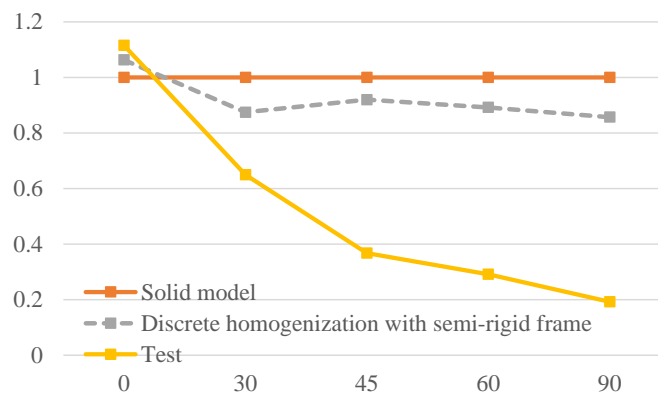
(a) Specimen 1



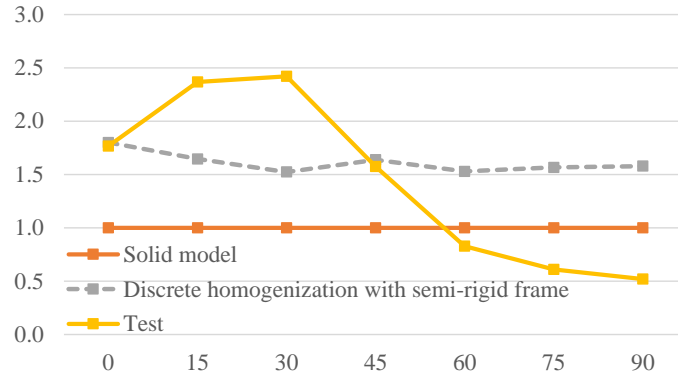
(b) Specimen 2

Figure 7-20 Normalized elastic modulus with varying build angle

The estimated elastic moduli from the homogenization procedure are compared with test results in Figure 7-20. The results were normalized with a reference value, which was determined using solid models with intact geometries. The reference values are 423.18 MPa for the rectangular unit cell and 236.73 MPa for the cross unit cell. The values were not changed with varying build angle because the geometrical degradation was ignored. The elastic moduli decreased as build angle increased due to geometric degradation. Since the proposed homogenization approach integrates the geometrical degradation into the estimation process, the result follows the trend in the results of test specimens. However, in the range of build angles over 45°, the estimates do not show the same trend as the test specimens in rectangular unit cell specimens. The error comes from additional manufacturing instabilities, which this research does not consider, such as support material surrounding the lattice structures, vibrations during fabrication and weak bonding force among layers due to reduction in bonding area.



(a) Specimen 1



(b) Specimen 2
Figure 7-21 Normalized yield strength with varying angle

The estimates of yield strength show large error compared with the test results. The resulting yield strength from the test rapidly decreases as the build angle increases. Implementation of the effective structural parameter can estimate the yield strength at a 0° build angle. Nonetheless, the estimation error is magnified in higher angles. Since the as-fabricated voxel model was constructed based on deposition path analysis, the model can include the effect of voids and deposition path patterns. However, the model cannot reflect all kinds of manufacturing instability. Thus, further study for additional manufacturing uncertainty can improve the estimates in the range of high build angles.

7.4.2 Powder Bed Fusion process

In order to validate the proposed homogenization procedure in the PBF process, body centered cubic lattice structures were fabricated and compression tests were performed. The resulting elastic modulus and yield strength are compared with the estimates from the proposed homogenization procedure.

Figure 7-22 presents the fabricated lattice structure, unit cell topology and its elementary strut. The strut diameter was 0.5 mm and the size of the unit cell was 4 mm.

Three layers of nine unit cells (3 x 3) were stacked. The total lattice size was 12 mm. Three specimens were fabricated in the SLM 280 selective laser melting system from SLM Solutions®. The layer thickness was set to 0.05 mm and AlSi10Mg aluminum powder was used. The size of powder particles was distributed between 0.02 mm and 0.06 mm with the mean value of 0.048 mm. Three specimen are fabricated and tested.

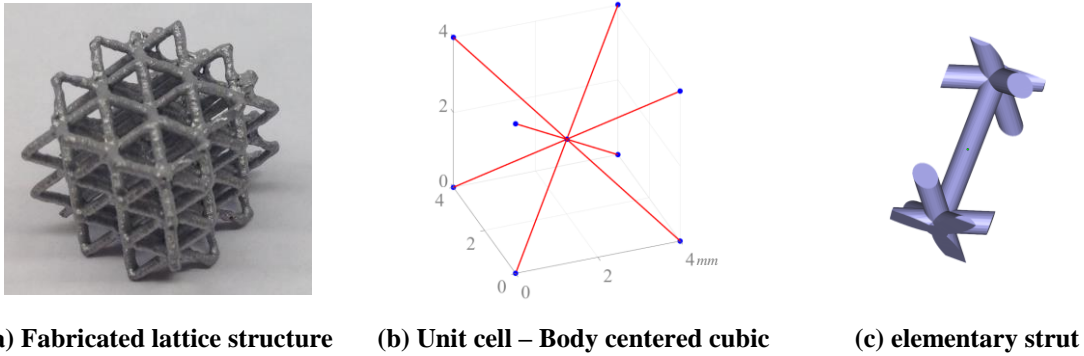


Figure 7-22 specimens for PBF process

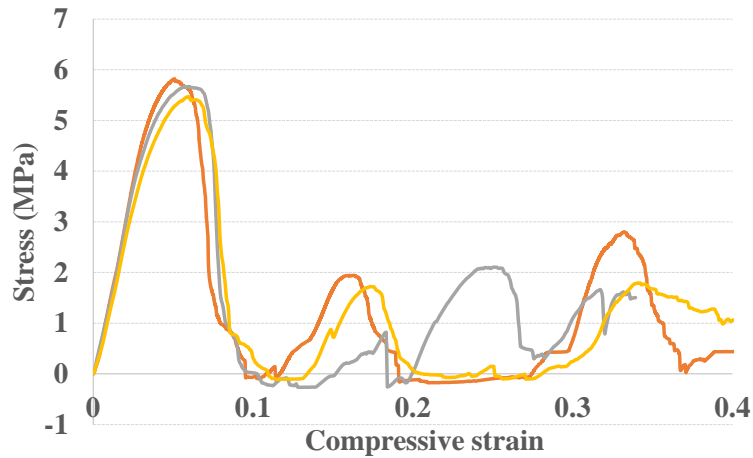


Figure 7-23 Result of compression test

The compression test was performed with the fabricated specimens in an in-house compression test machine. The resulting three stress-strain curves are presented in Figure 7-23. The peak stresses are observed at the failure stress of each layer in lattice structure. The elastic modulus and yield strength were determined based on the range between zero

to the first peak stress. The resulting elastic modulus and yield strength are 152 MPa and 5.82 MPa, respectively.

The as-fabricated voxel model for the elementary strut was constructed based on the manufacturing parameters. The effective strut diameter was determined to be 0.66 mm using the voxel model. The obtained structural element parameters were applied to the proposed homogenization approach. For comparison, two other approaches were implemented: discrete homogenization with shear flexible frame and asymptotic homogenization. The resulting mechanical properties are compared in Table 7-5. For the asymptotic homogenization, two strut diameters, the design strut diameter (0.5 mm) and the effective strut diameter (0.66 mm), were used in order to compare the results from homogenization approach.

The result shows that the proposed homogenization method yields more accurate elastic modulus and yield strength than the other approach does. The errors are 13.82 % for elastic modulus and -0.5% for yield strength. In contrast, asymptotic homogenization approaches lead to large error compared to the test result. Implantation of the design diameter significantly underestimated the mechanical properties. Since the strut diameter is increased due to geometrical degradation, the as-manufactured lattice structure is stiffer and stronger than the design. Furthermore, use of the effective strut diameter overestimates the elastic strength but underestimates the yield strength, which is the same trend in the results of material extrusion process. The result from shear flexible frame implementation with the effective diameter predicts less stiffness but higher yield strength. Since the effect of a joint is not considered in this approach, more deformation is expected and, as a result, larger deformation leads to lower stiffness. However, flexural

stress due to bending is reduced so that the estimated yield strength is increased. Based on this result, it can be concluded that the estimation process based on the discrete homogenization with semi-rigid frame elements is more accurate than the conventional asymptotic homogenization approaches due to lack of consideration for the effect of the AM process in the asymptotic homogenization.

Table 7-5 Comparison between test result and estimates

Unit: MPa	Test	Discrete homogenization with semi-rigid frame	Discrete homogenization with shear flexible frame	Asymptotic homogenization with 0.5 mm strut diameter	Asymptotic homogenization with 0.66 mm strut diameter
Elastic modulus	152	173.17 (+13.82%)	123.91 (-18.48%)	59.81 (-60.65%)	202.51 (+33.23%)
Yield strength	5.82	5.815 (-0.5%)	7.22 (+24.05%)	1.34 (-76.98%)	2.033 (-65.06%)

7.5 Chapter Summary

In this chapter, the estimation procedure for homogenized mechanical properties of additively manufactured cellular materials was developed by integrating semi-rigid joint frame elements into the discrete homogenization approach. In Sections 7.1 and 7.2, the discrete homogenization approach was introduced and explained.

In Section 7.3, the effects of the structural element parameters on two mechanical properties, elastic modulus and yield strength, were investigated. The parametric studies lead to two results: (1) the elastic modulus becomes stiffer as the joint related structural element parameters, such as fixity and eccentricity, are larger, and (2) the yield strength of the stretching dominated lattice structures is less sensitive to the joint related parameters.

In Section 7.4, the proposed discrete homogenization approach was validated by comparing the estimates with the test results. In the material extrusion process, the estimated elastic moduli were well matched with test results. The property-degradation due to geometrical degradation was able to be captured by this approach. However, in the asymptotic homogenization, resulting elastic moduli were significantly higher than test results. This is because use of intact dimensions in the asymptotic homogenization led to less deformation and, as a result, predicted stiffness became higher.

The estimated yield strength from the proposed method also exhibited less error than other methods but parametric studies on build angles indicated that the estimated yield strength of lattice structures fabricated in high build angles is extremely stronger than the test result. One reason for this phenomenon is the bonding strength between layers. The interlayer bonding strength limits the strength of lattice structure fabricated by the material extrusion process because the bonding is weaker than yield strength of the material. Thus, larger bonding area exposed to the opening force at high build angles increases the possibility of fracture failure. Consequently, apparent yield strength becomes lower as build angle increases and the difference between test result and estimates is increased.

In the powder bed fusion process, the proposed discrete homogenization approach with semi-rigid joint frame elements can predict mechanical properties more accurately. The geometrical degradation assessed from as-fabricated voxel models can be integrated into the proposed property-estimation procedure. Especially, since lattice structures fabricated by PBF do not have an obvious interlayer bonding problem process, which is observed in the material extrusion process, the accuracy for the estimated yield strength

was improved. In addition, use of designed dimensions without consideration of AM process effects yielded significant error in implementation of asymptotic homogenization as the same in the ME process.

Based on the results of Section 7.4, it can be conclude that the proposed method can estimate mechanical properties of additively manufactured lattice structure more accurately. Therefore, the third research question can be answered: the discrete homogenization approach can estimated mechanical properties of cellular material and the AM process effects can be integrated into the procedure by utilizing semi-rigid joint frame elements.

CHAPTER 8 Closure and Contribution

This chapter summarizes this dissertation and presents the conclusions from the previous chapters. Firstly, the entire research work in this dissertation is summarized. Next, the proposed research questions are revisited and answered based on the results of this research. Then, the contribution of this research is assessed. Finally, the dissertation ends up with the recommendation for future work to extend this research.

8.1 Summary of Dissertation

The goal of this research was introduced in Chapter 1 as the following:

To develop an estimation method for the mechanical properties of a lattice structure, in which the effects of the AM process are integrated

In Chapter 2, the research gap was identified based on a literature review. There are major issues: (1) process-modeling simulation in the previous research was confined to investigation of the AM process, (2) studies on propagation of the effects of the AM process were limited, and (3) conventional homogenization approaches yielded significant error in estimating the mechanical properties of lattice structures.

In Chapter 3, the research framework was proposed to achieve the research goal. The proposed research framework was developed based on four groups of parameters and three transformations among the groups. The parameters are Design and Manufacturing process parameters, Layer deposition parameters, Structural element parameters and

Cellular material properties. In order to define the transformation, three research questions were proposed and corresponding hypotheses were presented.

Chapter 4 introduced a deposition shape image, which is a result of process-modeling simulation. For the material extrusion process, the deposition process was modeled based on deposition path analysis. For the powder bed fusion process, the process are modeled based on assumptions from heat transfer analysis of a beam heating. Two functional relationships between DMPs and LDPs were derived in terms of the area and the dimensions of deposition geometries.

In Chapter 5, the as-fabricated voxel modeling approach was proposed and implemented for investigating the propagation of manufacturing instability through the layer-by-layer deposition process. The approaches for material extrusion and powder bed fusion process were explained. The voxel modeling approach was validated with material extruded tensile specimens. The result shows that the voxel model quantifies the geometrical degradation and reflects the effect of the degradation to the modeling process. It was also found that the voxel model approach has limited capacity to express degradation in yield strength built at high build angles.

In Chapter 6, the semi-rigid joint frame element was formulated in order to incorporate joint stiffening effects into the property-estimation process. The effective values of the required structural element parameters such as strut length, diameter, joint size and joint stiffness were determined based on as-fabricated voxel models. A parametric study of effective structural element parameters shows that instabilities in AM processes degrade the effective value of structural parameters and that the bigger joint design leads to stiffer and larger joint related structural element parameters.

Chapter 7 presented the discrete homogenization approach for two mechanical properties of cellular materials, elastic modulus and yield strength. Integrating a semi-rigid joint frame element into the homogenization approach enables the system to reflect the AM process effects in the estimates. The properties are affected by three major structural element parameters: (1) as the strut diameter grows larger, the lattice structure becomes stronger and stiffer, (2) as the joint stiffness and size grow larger, the lattice structure becomes stiffer, and (3) the yield strength of stretching-dominated lattice structures is less sensitive to joint stiffness and size than that of bending dominated lattice structures. The proposed method was validated by comparing the estimates with test results. The comparison indicates that the proposed discrete homogenization approach can predict mechanical properties more accurately than conventional asymptotic homogenization approach.

The following section will address the answer for the research questions posed in Chapter 3.

8.2 Revisiting Research Questions

8.2.1 Research Question 1

How are functional relationships between the design and manufacturing process parameters and the layer deposition parameters quantitatively explained?

Hypothesis 1: The functional relationships can be explained by the use of process-modeling simulation and the computation of the stochastic distributions of LPDs using a

Monte Carlo method. The LPDs can be evaluated based on deposition shape images, which are obtained from the process-modeling simulation.

Validation of Hypothesis 1: In Chapter 4, a shape deposition image that is the result of process-modeling simulation was introduced. In the material extrusion process, the image was obtained based on deposition paths and manufacturing process parameters such as nozzle size, layer thickness and deposition width. In the powder bed fusion process, the assumptions for the melting pool were drawn from a heat transfer analysis. The image was generated by considering powder particle distributions and internal void generation. While constructing the image, the uncertainties were imposed to manufacturing process parameters. The layer deposition parameters were calculated by analyzing the images. The results of the parametric studies in Chapter 4 showed that the variation in layer deposition parameters, which were propagated from instabilities in manufacturing process parameters, could be captured by a process-modeling scheme in two AM processes. The stochastic distributions of the deposited area and the dimension of deposition shaped were obtained based on the method of Monte Carlo simulation. Therefore, Hypothesis 1 has been validated and Research question 1 has been answered.

8.2.2 Research Question 2

How is the propagation of geometrical and material variations from the layer deposition parameters to the structural element parameters quantitatively described through the repeated stacking procedure?

Hypothesis 2: The effective values of the structural element parameters, such as the sizes of joints and struts, may quantify the geometrical and material variations that accumulate during the repeated stacking procedure. These effective values can be determined by equating the analytic formula for structural elements and the mechanical responses from numerical analysis using a voxel based model that mimics the layer stacking process.

Validation of Hypothesis 2: In Chapter 5, the as-fabricated voxel-modeling scheme was proposed to construct a geometrical model of deposited shape. This modeling scheme has capabilities to incorporate manufacturing process parameters into the geometrical model by utilizing the deposition shape images to generate the voxel model. Thus, propagation of the geometrical variation due to manufacturing instabilities from layer scale to structural feature scale can be described. The validation results showed that manufacturing instabilities embedded in the deposition shape images affected the mechanical properties and the voxel model could describe the property-degradation.

In Chapter 6, the semi-rigid joint frame element enables to quantify the impacts of manufacturing instabilities embedded in the voxel model on structural element parameters such as the diameter, joint stiffness and joint size. The effective values were determined by comparing structural responses of the voxel models and semi-rigid joint frame element. The results of parametric studies in Section 6.4 support Hypothesis 2. The results imply that the large joint leads to stiffer and larger joint related structural parameters and build angle alter the effective values. The manufacturing uncertainties weaken the structural parameters in the material extrusion process. Therefore, Hypothesis 2 is fully supported by validation results.

8.2.3 *Research Question 3*

What numerical method can be implemented in order to formulate an estimation procedure for the mechanical properties of a periodic cellular material fabricated by the AM process?

Hypothesis 3: The discrete homogenization technique can be used to estimate the mechanical properties for the cellular material, and the parameters for integrating the effects of the AM process could be introduced by employing semi-rigid jointed frame elements to model the representative unit cell.

Validation of Hypothesis 3: In Chapter 8, the discrete homogenization approach was introduced and implemented with semi-rigid joint frame elements. The effective structural element parameters that were evaluated using the as-fabricated voxel model could be incorporated into the homogenization procedure. The parametric studies on the effective structural parameters support the Hypothesis 3. Moreover, the validation results in Section 7.4 indicate that the proposed discrete homogenization increases the accuracy compared to the asymptotic homogenization. Therefore, Hypothesis 3 is validated and Research question 3 is answered.

8.3 Contributions

Although various mechanical property evaluation procedures for cellular materials have been developed over three decades, there is still a large gap to fill. Mathematical and numerical approaches tend to significantly over- or under-estimate the mechanical properties than those of the as-manufactured cellular materials. Especially, unreliable and unrepeatable mechanical characteristics of additive manufactured lattice structures prevent to extend the application of cellular materials. The main contribution of this research is to initiate to assess the effects of manufacturing process on mechanical properties. The contribution of this research is summarized as below:

1. The as-fabricated geometry modeling procedure for AM processes was proposed. There is numerous research reporting the qualitative assessment of geometrical defects originated from additive manufacturing processes. However, little research has proposed modeling methods. The methods are not general and they are limited to solve specific problems from their applications. In this research, the systematic as-fabricated geometry modeling approach is proposed, which is based on the voxel model and two-dimensional deposition shape images from process-modeling analysis. This method is extendable to most AM processes that utilize a repeated stacking method. Therefore, the original contribution is to develop the general as-fabricated geometrical modeling procedure.

2. The manufacturing effect quantification scheme was developed. Much research addresses that there is discrepancy in geometrical dimension and mechanical properties between a design and an additively manufactured part due to manufacturing effects. To

calibrate this difference, most research utilizes heuristic approaches, which do not have mathematical background or is not based on mechanics. In this context, our contribution is to develop the manufacturing effect evaluation scheme that is based on a semi-rigid joint frame element and corresponding voxel model. With this approach, geometrical degradation originated from manufacturing instabilities is transformed to structural parameters, which affects mechanical properties of cellular material. The effectiveness of this approach is supported by the series of parametric studies in this dissertation and the method can help the engineer to design lattice structures.

3. The homogenization procedure that enables to integrate joint effects was developed. Most developed homogenization approach ignores the effects of joint characteristics. However, the joint has critical impacts on mechanics of lattice structures. The joint augments additional stiffness and reduces the effective length of structural elements in cellular materials. Especially, it has critical impacts on cellular materials that have small and high-density unit cell topology. Moreover, two kinds of conventional numerical modeling approaches for a lattice structure, such as use of frame (beam) elements and continuum elements, have inherent disadvantages: (1) ignoring joint effect in a frame element and (2) relatively large computational resource and impractical stress concentration problem in a continuum element. In this research, one of main contributions is to introduce a semi-rigid joint frame element to solve the problems. This enables to take account for joint characteristics and to solve unrealistic stress concentration problems.

8.4 Recommendation for Future work

The following future work will help to extend this dissertation research to implementation in real engineering tasks and engineer to utilize the results of this research.

1. Support for design methodology

The property estimation approach proposed and investigated in this dissertation aims to analyze lattice structures whose geometries are given. To help the engineers to design cellular materials, research on supporting for design method is critical. Since the design task is a reverse procedure of analysis, this research can be a baseline to develop cellular material design method using AM process.

2. Property estimation for tailored cellular materials

This research focused on periodic cellular materials, in which infinitely repeated unit cell are assumed. However, the cellular materials should be tailored in order to implement them in the real engineering applications. Much research has reported that estimated mechanical properties using homogenization approach with periodicity are not consistent with mechanical properties of fabricated cellular material. Therefore, a study on property-change due to eliminating periodicity is required to help to extend the application of cellular materials.

3. Considering anisotropy in estimation procedure

Since AM processes stacks up a series of two-dimensional material deposition, fabricated parts inherently exhibits material anisotropy. Especially, failure strength is critically affected by material anisotropy. As explained in Section 7.4.1.2, the proposed method has limitations to predict the yield strength of material extrusion lattice structures at high build angle. Thus, future research on integrating material anisotropy is required to increase reliability of cellular materials.

4. Integrating various process modeling simulation

In order to implement the proposed method to other AM processes, their processes are needed to be modeled simulated. In this research, the simulation model is confined to material extrusion and powder bed fusion process. Therefore, integrating other AM process simulation will help to extend application of this research.

8.5 Lessons Learned

1. Voxel modeling approach

As-fabricated voxel model approach provides a simple model to substitute complex high-fidelity process simulation model. This approach can reduce computational resource and cost. However, since this approach emphasizes only geometrical modeling aspects, there are limitations that need to be addressed in the future research.

Firstly, the as-fabricated voxel model cannot describes defects from material characteristics. Geometrical defects such as stair steps, voids and gaps can be captured by implementing this approach but non-geometrical defects such as layer separation and

cracks in the material extrusion process, which are explained by not only geometric modeling but also additional physics, cannot be expressed using this approach. This approach assumes perfect bonding among voxels. Therefore, this approach can be utilized to estimate properties only in elastic range where perfect bonding can be assumed. However, proper material models should be considered for predicting mechanical performance beyond the elastic range. The results in Section 5.3.4 support this. The as-fabricated voxel model can evaluate degradation in elastic modulus due to manufacturing instabilities in the material extrusion process. However, degradation in yield strength cannot be explained by this approach. To solve this problem, a proper material model for each AM process needs to be considered during ad-fabricated voxel modeling. One recommendation to take account for degradation in yield strength is to apply fracture mechanics approaches to describe crack propagation embedded due to the material extrusion process

Secondly, this approach does not fully consider related physics in AM processes. Especially, for the powder bed fusion process, this approach cannot reflect complex heat transfer phenomena on as-fabricated voxel models. Accordingly, implementation of this approach is confined to small features compared to the process resolution such as thin struts whose cross-section can be filled using simple infill beam scan patterns that do not yield thermal distortion, which is an important manufacturing issue. Thus, higher-level process simulation model will help to overcome this limitation.

Lastly, this approach only focuses on modeling given parts without consideration for ancillary structures required in process. In reality, support structures are necessarily generated and they affects the as-manufactured shape of cellular material. In the material

extrusion process, struts can be fabricated as surrounded by the support material at the high build angle as mentioned in Section 5.3.4. The support material limits the location of deposited filaments so that the amount of bonding area between the layers can be fluctuated from the original design. In addition, manufacturing instability in deposition of support material also can alter the shape of a deposited filament. In the powder bed fusion process, support structures are not used but structures that plays a role of a heat sink is important. Improper heat sink structure leads to failure during fabrication. Moreover, since struts near the heat sink structure are exposed to more heat energy, they can be thicker than other struts in the cellular material. Thus, consideration of artificial structures generated during manufacturing will improve accuracy of the approach.

2. Considerations for designing cellular materials

One of important geometrical characteristics of cellular materials is that cellular materials consist of small features compared to overall dimension of the material. In general implementation of lattice structure, struts have small diameter as a few times of AM process resolution. Since relative magnitude of geometrical variation in a small feature is larger than in large feature, the effect of geometrical degradation becomes more critical in cellular material. Thus, manufacturing characteristics should be considered from design stages and understanding characteristics of AM processes helps engineers to design cellular materials.

In material extrusion process, the fundamental concept of this process is to place molten material to approximate part geometries. Thus, the effective fabricated dimension, which reflects physical bonding among the layers, tends to be smaller than design

specification. This is caused by manufacturing instability in deposited filament width and stair-stepping phenomenon. There can be regions inside struts, which are totally void or include large gaps and voids inside strut contour boundaries if the regions inside contour boundaries cannot be approximated properly by integer multiples of width of the filament. This significantly deteriorates the mechanical property of cellular materials. In this context, when designing cellular materials which have low material fraction for the material extrusion process, large unit cell size that ensures larger strut size compared to filament width is recommended than small unit cell size at the same volume fraction.

In the powder bed fusion process, the fundamental process is melting. Accordingly, the process tend to yield bigger strut than design specification due to heat transfer phenomena. Moreover, the size of powder particles thickens geometric dimensions of fabricated struts and its effect become more critical as strut size is smaller. Therefore, the heat sources, laser or electron beam, need to be controlled during manufacturing based on powder particles distribution. This will help to reduce mismatch between design and as-manufactured cellular material.

Since the struts in the lattice structure are generally small compared to the manufacturing process resolution such as filament width and melting pool size, there is no minimum feature size that is insensitive to the manufacturing process parameters in both process. The geometrical characteristics are always affected by manufacturing process parameter. Based on the experience in material extrusion process, minimum feature size to prevent failure in build can be recommended as 1.5 mm. Building lattice structure with strut diameter below 1.5 mm was always failed in Stratasys machines with

T16 and T10 tips. Thus, designer can use this diameter as the guideline. However, due to limited experience in powder bed fusion process, recommendation cannot be made.

3. Testing

Testing is the important part of this research. Since the general testing standards for additively manufactured cellular material have not been set up, designing specimen is not easy. One issue in preparing specimens is the amount of raw material. The cost for testing is proportional to the amount of the material. This become more critical in the metal powder bed fusion process since the process is cost-intensive. Thus, compression tests are highly recommended for the metal powder bed fusion process since specimens consist of only lattice structures without grips that are necessarily required in tensile tests. For material extrusion process, to measure only elastic modulus, compression tests are recommended for the same reason as the powder bed fusion. However, beyond the elastic range, the type of tests should be selected based on the target responses.

The other issue in preparing specimens of cellular material is determining a number of unit cell repetition. Since theoretical and numerical estimating approaches are based on periodicity while the specimens are tailored, approximating periodicity is important. Based on the testing experience in this research, at least four unit cells are required to express periodicity. However, this number depends on the shape of the unit cell.

For validation of modeling and estimation procedure, 2D lattice structure specimens in Section 7.4.2 can be used since analytic estimations are available based on structural mechanics. In addition, the effect of the build angle can be studied at relatively low testing cost compared to 3D lattice structures. However, since periodicity needs to be

consider in the homogenization procedure, 3D lattice specimens mentioned in Section 7.4.1 is recommended for validating mechanical properties of lattice structure. In these specimens, the periodicity can be assumed. Thus, the 3D lattice specimens are recommended for validating performance of lattice structures.

4. Important manufacturing parameters

Mechanical properties of cellular materials mainly depend on the structural and topological characteristics of corresponding representative unit cells defined by the arrangement of structural elements. Thus, structural element parameters determine the mechanical properties of the cellular material. However, the structural element parameters are affected by manufacturing instabilities propagated and accumulated through the layer-by-layer deposition process. In this research, propagation and accumulation of manufacturing instabilities are captured by the as-fabricated voxel modeling approach, which is simplified modeling approach for process-simulation. The as-fabricated voxel modeling is an important step to convert the manufacturing instability to geometrical model. The effects of manufacturing process parameters are integrated into the voxel model in the form of voids, gaps and stair-steps. The effects of manufacturing process are evaluated by analyzing the voxel model and are incorporated into structural element parameters. As a result, the mechanical properties are dependent on the process parameters and are more sensitive to two manufacturing process parameters for each AM process.

The major parameters in the material extrusion process are the deposition pattern and the nozzle tip size. Since the deposition pattern changes the internal structure and

bonding of as-fabricated cellular material, the properties of as-fabricated cellular materials are closely related. Moreover, the nozzle tip size controls two major variables in material extrusion, which are the filament width and layer thickness. The filament width can alter the deposition path pattern. Thus, it affects the properties. Since the layer thickness is related to the stair-step phenomenon, it also affects the mechanical response of the cellular material.

In the powder bed fusion processes, powder particle distribution and melting pool size are important parameters based on the result of this research. Since powder particle distribution is selected based availability from manufacturers, the melting pool size needs to be controlled based on the particle distribution. In this research, the melting pool size is assumed as beam diameter and the as-fabricated voxel model is constructed based on this assumption. To increase accuracy and reliability of the estimation process, more studies on process modeling, which evaluate the relationship between laser or electron beam energy and melting pool size, are required.

5. Use of homogenized cellular material properties

Designers and engineers can treat the lattice structure as the continuum by using the estimated homogenized properties. Since evaluating mechanical response of cellular material is a crucial step in design procedure for a cellular material embedded part, they can reduce modeling time and cost by implementing proposed homogenization approach.

Popular approach to calculate mechanical responses of cellular material is to model the material using conventional frame elements. However, this approach tends to overestimate the performance of lattice structures. From the results in Section 7.4.1, it is

obvious that use of the conventional Euler frame elements with design diameter overestimates the mechanical performance of lattice structures. In addition, use of the flexible frame elements shows fluctuated mechanical properties. This leads to unexpected mechanical performance or failure of parts. Thus, homogenized mechanical properties derived from developed estimation procedure in this research can be used as conservative design criteria because the degradation during manufacturing is considered and incorporated in the homogenized properties.

One disadvantage of using the homogenized properties is that the properties are confined to a part, which ensures a periodicity. Since the estimated properties are derived based on infinite repetition of unit cells, the homogenized properties can be stronger than properties of tailored lattice structure. Thus, it is not recommended for a lattice structure, which has limited repetition of unit cell, but use of semi-rigid joint frame elements is recommended to model the lattice structure.

APPENDIX A THREE-DIMENSIONAL SHEAR DEFORMABLE SEMI-RIGID JOINT BEAM

This section presents details of the three-dimensional shear deformable semi-rigid joint beam, which governs flexural deformation in the frame element. The elemental coordinate system is shown in Figure A - 1

A.1 Shape Functions

Displacement in the frame region along the direction 2 can be interpolated using the following shape functions:

$$N_v = \begin{bmatrix} \bar{\phi}_3 (1 - 3s^2 + 2s^3 + \phi_3 (1 - s)) \\ L\bar{\phi}_3 \left(s - 2s^2 + s^3 + \frac{\phi_3}{2} (s - s^2) \right) \\ \bar{\phi}_3 (3s^2 - 2s^3 + \phi_3 s) \\ L\bar{\phi}_3 \left(-s^2 + s^3 + \frac{\phi_3}{2} (-s + s^2) \right) \end{bmatrix}^T$$

$$\bar{\phi}_3 = \frac{1}{1 + \phi_3}, \quad \phi_3 = \frac{12EI_{33}}{k_2 GAL^2}$$

$$v(s) = \mathbf{N}_v \tilde{\mathbf{d}}^e$$

where, E and G are elastic and shear modulus of the raw material, respectively. A and L are the cross-sectional area and the length of frame element, respectively. I_{33} and k_2 are the second moment of area with respect to axis 3 and the shear correction factor with respect to axis 2, respectively. $\tilde{\mathbf{d}}^e$ is the internal nodal displacement for the frame region.

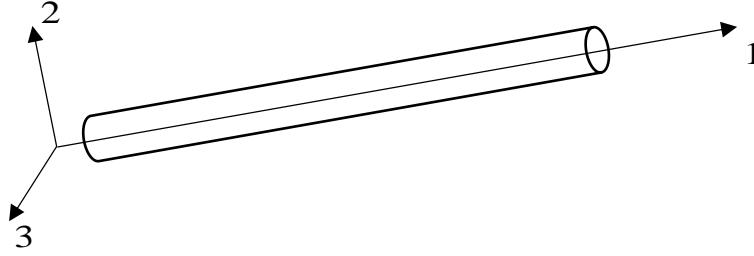


Figure A - 1 Elemental Coordinate

Displacement in the frame region along the direction 3 also can be interpolated in the same way as displacement along the direction 2 using the following shape functions:

$$N_v = \begin{bmatrix} \bar{\phi}_2 (1 - 3s^2 + 2s^3 + \phi_2 (1 - s)) \\ -L\bar{\phi}_2 \left(s - 2s^2 + s^3 + \frac{\phi_2}{2} (s - s^2) \right) \\ \bar{\phi}_2 (3s^2 - 2s^3 + \phi_2 s) \\ -L\bar{\phi}_2 \left(-s^2 + s^3 + \frac{\phi_2}{2} (-s + s^2) \right) \end{bmatrix}^T$$

$$\bar{\phi}_2 = \frac{1}{1 + \phi_2}, \quad \phi_2 = \frac{12EI_{22}}{k_3 GAL^2}$$

$$w(s) = \mathbf{N}_w \tilde{\mathbf{d}}^e$$

where, I_{22} and k_3 are the second moment of area with respect to axis 2 and the shear correction factor with respect to axis 3, respectively.

The shape functions of the shear deformable semi-rigid joint beam are derived as the following:

$$v(s) = \mathbf{N}_v (\mathbf{I} + \mathbf{E})(\mathbf{I} - \mathbf{S}) \mathbf{d}^e$$

$$w(s) = \mathbf{N}_w (\mathbf{I} + \mathbf{E})(\mathbf{I} - \mathbf{S}) \mathbf{d}^e$$

where, \mathbf{d}^e is the nodal displacement for the semi-rigid joint beam. The detailed derivation is found in the literature [95].

A.2 Stiffness Matrix

The stiffness matrix of the frame region is given as the following:

$$\tilde{\mathbf{K}}_b = \begin{bmatrix} \frac{12EI_{33}}{L^3(1+\phi_3)} & 0 & 0 & \frac{6EI_{33}}{L^2(1+\phi_3)} & \frac{-12EI_{33}}{L^3(1+\phi_3)} & 0 & 0 & \frac{6EI_{33}}{L^2(1+\phi_3)} \\ 0 & \frac{12EI_{22}}{L^3(1+\phi_2)} & \frac{-6EI_{22}}{L^2(1+\phi_2)} & 0 & 0 & \frac{-12EI_{22}}{L^3(1+\phi_2)} & \frac{-6EI_{22}}{L^2(1+\phi_2)} & 0 \\ 0 & \frac{-6EI_{22}}{L^2(1+\phi_2)} & \frac{(4+\phi_2)EI_{22}}{L(1+\phi_2)} & 0 & 0 & \frac{6EI_{22}}{L^2(1+\phi_2)} & \frac{(2-\phi_2)EI_{22}}{L(1+\phi_2)} & 0 \\ \frac{6EI_{33}}{L^2(1+\phi_3)} & 0 & 0 & \frac{(4+\phi_3)EI_{33}}{L(1+\phi_3)} & \frac{-6EI_{33}}{L^2(1+\phi_3)} & 0 & 0 & \frac{(2-\phi_3)EI_{33}}{L(1+\phi_3)} \\ \frac{-12EI_{33}}{L^3(1+\phi_3)} & 0 & 0 & \frac{-6EI_{33}}{L^2(1+\phi_3)} & \frac{12EI_{33}}{L^3(1+\phi_3)} & 0 & 0 & \frac{-6EI_{33}}{L^2(1+\phi_3)} \\ 0 & \frac{-12EI_{22}}{L^3(1+\phi_2)} & \frac{6EI_{22}}{L^2(1+\phi_2)} & 0 & 0 & \frac{12EI_{22}}{L^3(1+\phi_2)} & \frac{6EI_{22}}{L^2(1+\phi_2)} & 0 \\ 0 & \frac{-6EI_{22}}{L^2(1+\phi_2)} & \frac{(2-\phi_2)EI_{22}}{L(1+\phi_2)} & 0 & 0 & \frac{6EI_{22}}{L^2(1+\phi_2)} & \frac{(4+\phi_2)EI_{22}}{L(1+\phi_2)} & 0 \\ \frac{6EI_{33}}{L^2(1+\phi_3)} & 0 & 0 & \frac{(2-\phi_3)EI_{33}}{L(1+\phi_3)} & \frac{-6EI_{33}}{L^2(1+\phi_3)} & 0 & 0 & \frac{(4+\phi_3)EI_{33}}{L(1+\phi_3)} \end{bmatrix}$$

This stiffness matrix is used for Equation (6.18).

APPENDIX B BLOCK MATRICES FOR SELECTED UNIT CELLS

This section presents block matrices for selected unit cells. In the proposed discrete homogenization approach, the nodal displacement vector is expressed as the following:

$$\mathbf{d} = \mathbf{B}_0 \mathbf{d}_0 + \mathbf{B}_a \Delta \mathbf{a}$$

The block matrices, \mathbf{B}_0 and \mathbf{B}_a , are given in the following sections. The size of \mathbf{B}_0 is the total number of nodes \times the number of independent nodes. The size of \mathbf{B}_a is the total number of nodes \times the number of periodic vectors. In a three-dimensional unit cell, the number of periodic vectors is generally three. In the following sections, \mathbf{I} is a 6×6 identity matrix, \mathbf{I}_t is an augmented identity matrix in Equation (7.9), and $\mathbf{0}$ is a zero matrix.

B.1 Cubic Unit Cell

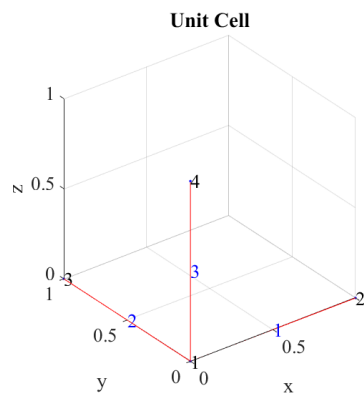


Figure B - 1 Unit cell topology: Cubic unit cell

B.4 Body Center Cubic Unit Cell

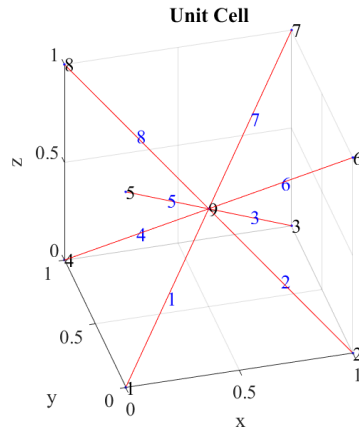


Figure B - 4 Unit cell topology: Body Centered Cubic unit cell

$$\mathbf{B}_0 = \begin{bmatrix} \mathbf{I} & \mathbf{0} \\ \mathbf{0} & \mathbf{0} \\ \mathbf{0} & \mathbf{0} \\ \mathbf{0} & \mathbf{0} \\ \mathbf{0} & \mathbf{0} \\ \mathbf{0} & \mathbf{0} \\ \mathbf{0} & \mathbf{0} \\ \mathbf{0} & \mathbf{0} \\ \mathbf{0} & \mathbf{I} \end{bmatrix}, \quad \mathbf{B}_a = \begin{bmatrix} \mathbf{0} & \mathbf{0} & \mathbf{0} \\ \mathbf{I}_t & \mathbf{0} & \mathbf{0} \\ \mathbf{I}_t & \mathbf{I}_t & \mathbf{0} \\ \mathbf{0} & \mathbf{I}_t & \mathbf{0} \\ \mathbf{0} & \mathbf{0} & \mathbf{I}_t \\ \mathbf{I}_t & \mathbf{0} & \mathbf{I}_t \\ \mathbf{I}_t & \mathbf{I}_t & \mathbf{I}_t \\ \mathbf{0} & \mathbf{I}_t & \mathbf{I}_t \\ \mathbf{0} & \mathbf{0} & \mathbf{0} \end{bmatrix}$$

B.5 Octet-Truss Unit Cell

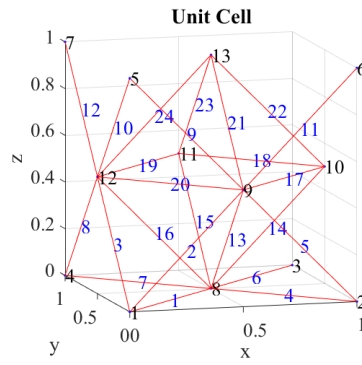


Figure B - 5 Unit cell topology: Octet-truss unit cell

$$\mathbf{B}_0 = \begin{bmatrix} \mathbf{I} & \mathbf{0} & \mathbf{0} & \mathbf{0} \\ \mathbf{0} & \mathbf{0} & \mathbf{0} & \mathbf{0} \\ \mathbf{0} & \mathbf{0} & \mathbf{0} & \mathbf{0} \\ \mathbf{0} & \mathbf{0} & \mathbf{0} & \mathbf{0} \\ \mathbf{0} & \mathbf{0} & \mathbf{0} & \mathbf{0} \\ \mathbf{0} & \mathbf{0} & \mathbf{0} & \mathbf{0} \\ \mathbf{0} & \mathbf{0} & \mathbf{0} & \mathbf{0} \\ \mathbf{0} & \mathbf{I} & \mathbf{0} & \mathbf{0} \\ \mathbf{0} & \mathbf{0} & \mathbf{I} & \mathbf{0} \\ \mathbf{0} & \mathbf{0} & \mathbf{0} & \mathbf{0} \\ \mathbf{0} & \mathbf{0} & \mathbf{0} & \mathbf{0} \\ \mathbf{0} & \mathbf{0} & \mathbf{0} & \mathbf{I} \\ \mathbf{0} & \mathbf{0} & \mathbf{0} & \mathbf{0} \end{bmatrix}, \quad \mathbf{B}_a = \begin{bmatrix} \mathbf{0} & \mathbf{0} & \mathbf{0} \\ \mathbf{I}_t & \mathbf{0} & \mathbf{0} \\ \mathbf{I}_t & \mathbf{I}_t & \mathbf{0} \\ \mathbf{0} & \mathbf{I}_t & \mathbf{0} \\ \mathbf{0} & \mathbf{0} & \mathbf{I}_t \\ \mathbf{I}_t & \mathbf{0} & \mathbf{I}_t \\ \mathbf{0} & \mathbf{I}_t & \mathbf{I}_t \\ \mathbf{0} & \mathbf{0} & \mathbf{0} \\ \mathbf{0} & \mathbf{0} & \mathbf{0} \\ \mathbf{I}_t & \mathbf{0} & \mathbf{0} \\ \mathbf{0} & \mathbf{I}_t & \mathbf{0} \\ \mathbf{0} & \mathbf{0} & \mathbf{0} \\ \mathbf{0} & \mathbf{0} & \mathbf{I}_t \end{bmatrix}$$

REFERENCES

1. Ashby, M., *Hybrid Materials to Expand the Boundaries of Material-Property Space*. Journal of the American Ceramic Society, 2011. **94**: p. s3-s14.
2. Deshpande, V.S., Fleck, N.A., and Ashby, M.F., *Effective properties of the octet-truss lattice material*. Journal of the Mechanics and Physics of Solids, 2001. **49**(8): p. 1747-1769.
3. Wadley, H.N., Fleck, N.A., and Evans, A.G., *Fabrication and structural performance of periodic cellular metal sandwich structures*. Composites Science and Technology, 2003. **63**(16): p. 2331-2343.
4. Ashby, M.F. and Medalist, R.F.M., *The mechanical properties of cellular solids*. Metallurgical Transactions A, 1983. **14**(9): p. 1755-1769.
5. Ashby, M.F., Evans, T., Fleck, N.A., Hutchinson, J., Wadley, H., and Gibson, L., *Metal foams: a design guide*. 2000: Elsevier.
6. GrantaDesign, *CES Edupack 2016*. <http://www.grantadesign.com>.
7. Banhart, J., *Manufacture, characterisation and application of cellular metals and metal foams*. Progress in Materials Science, 2001. **46**(6): p. 559-632.
8. Chiras, S., Mumm, D.R., Evans, A.G., Wicks, N., Hutchinson, J.W., Dharmasena, K., Wadley, H.N.G., and Fichter, S., *The structural performance of near-optimized truss core panels*. International Journal of Solids and Structures, 2002. **39**(15): p. 4093-4115.
9. Wadley, H.N.G., Fleck, N.A., and Evans, A.G., *Fabrication and structural performance of periodic cellular metal sandwich structures*. Composites Science and Technology, 2003. **63**(16): p. 2331-2343.
10. Gao, W., Zhang, Y., Ramanujan, D., Ramani, K., Chen, Y., Williams, C.B., Wang, C.C.L., Shin, Y.C., Zhang, S., and Zavattieri, P.D., *The status, challenges, and future of additive manufacturing in engineering*. Computer-Aided Design, 2015. **69**: p. 65-89.
11. Agarwala, M.K., Jamalabad, V.R., Langrana, N.A., Safari, A., Whalen, P.J., and Danforth, S.C., *Structural quality of parts processed by fused deposition*. Rapid Prototyping Journal, 1996. **2**(4): p. 4-19.
12. Gong, H., Rafi, K., Gu, H., Starr, T., and Stucker, B., *Analysis of defect generation in Ti-6Al-4V parts made using powder bed fusion additive manufacturing processes*. Additive Manufacturing, 2014. **1-4**: p. 87-98.
13. Crawford, R.H., *Computer aspects of solid freeform fabrication: geometry, process control, and design*. Solid Freeform Fabrication Symposium Proceedings, 1993: p. 101.
14. Crawford, D.C.T.R.H. *Optimizing Part Quality with Orientation*. in *Solid Freeform Fabrication Symposium Proceedings*. 1995. Center for Materials Science and Engineering, Mechanical Engineering Department and Chemical Engineering Department, the University of Texas at Austin.
15. Chartoff, R.P., Flach, L., and Weissman, P. *Material and process parameters that affect accuracy in stereolithography*. in *Solid Freeform Fabrication Symposium Proceedings*. 1993. DTIC Document.

16. Amon, C., Beuth, J., Kirchner, H., Merz, R., Prinz, F., Schmaltz, K., and Weiss, L., *Material issues in layered forming*. Proc. Solid Freeforming Fabrication Symposium, 1993: p. 1-10.
17. Yardimci, M.A., Güçeri, S.I., Agarwala, M., and Danforth, S.C. *Part quality prediction tools for fused deposition processing*. in *Proceedings of Solid Freeform Fabrication Symposium*. 1996.
18. Ahn, S.H., Montero, M., Odell, D., Roundy, S., and Wright, P.K., *Anisotropic material properties of fused deposition modeling ABS*. Rapid Prototyping Journal, 2002. **8**(4): p. 248-257.
19. Sood, A.K., Ohdar, R.K., and Mahapatra, S.S., *Parametric appraisal of mechanical property of fused deposition modelling processed parts*. Materials & Design, 2010. **31**(1): p. 287-295.
20. Wang, C.C., Lin, T.W., and Hu, S.S., *Optimizing the rapid prototyping process by integrating the Taguchi method with the Gray relational analysis*. Rapid Prototyping Journal, 2007. **13**(5): p. 304-315.
21. Jin, Y.-a., He, Y., Fu, J.-z., Gan, W.-f., and Lin, Z.-w., *Optimization of tool-path generation for material extrusion-based additive manufacturing technology*. Additive Manufacturing, 2014. **1-4**(0): p. 32-47.
22. Yardimci, M.A. and Güçeri, S., *Conceptual framework for the thermal process modelling of fused deposition*. Rapid Prototyping Journal, 1996. **2**(2): p. 26-31.
23. Bellini, A., *Fused Deposition of Ceramics: A Comprehensive Experimental, Analytical and Computational Study of Material Behavior, Fabrication Process and Equipment Design*. 2002, Drexel University.
24. Bellini, A. and Güçeri, S., *Mechanical characterization of parts fabricated using fused deposition modeling*. Rapid Prototyping Journal, 2003. **9**(4): p. 252-264.
25. Sun, Q., Rizvi, G.M., Bellehumeur, C.T., and Gu, P., *Effect of processing conditions on the bonding quality of FDM polymer filaments*. Rapid Prototyping Journal, 2008. **14**(2): p. 72-80.
26. Huang, B. and Singamneni, S., *Adaptive slicing and speed-and time-dependent consolidation mechanisms in fused deposition modeling*. Proceedings of the Institution of Mechanical Engineers, Part B: Journal of Engineering Manufacture, 2013: p. 0954405413497474.
27. Rodríguez, J.F., Thomas, J.P., and Renaud, J.E., *Mechanical behavior of acrylonitrile butadiene styrene (ABS) fused deposition materials. Experimental investigation*. Rapid Prototyping Journal, 2001. **7**(3): p. 148-158.
28. Rodriguez, J.F., Thomas, J.P., and Renaud, J.E., *Characterization of the mesostructure of fused-deposition acrylonitrile-butadiene-styrene materials*. Rapid Prototyping Journal, 2000. **6**(3): p. 175-186.
29. Das, S., *Physical Aspects of Process Control in Selective Laser Sintering of Metals*. Advanced Engineering Materials, 2003. **5**(10): p. 701-711.
30. Cervera, G.B.M. and Lombera, G., *Numerical prediction of temperature and density distributions in selective laser sintering processes*. Rapid Prototyping Journal, 1999. **5**(1): p. 21-26.
31. Shiomi, M., Yoshidome, A., Abe, F., and Osakada, K., *Finite element analysis of melting and solidifying processes in laser rapid prototyping of metallic powders*. International Journal of Machine Tools and Manufacture, 1999. **39**(2): p. 237-252.

32. Kolossov, S., Boillat, E., Glardon, R., Fischer, P., and Locher, M., *3D FE simulation for temperature evolution in the selective laser sintering process*. International Journal of Machine Tools and Manufacture, 2004. **44**(2-3): p. 117-123.
33. Zäh, M.F. and Lutzmann, S., *Modelling and simulation of electron beam melting*. Production Engineering, 2010. **4**(1): p. 15-23.
34. Zeng, K., Pal, D., Patil, N., and Stucker, B., *A New Dynamic Mesh Method Applied to the Simulation of Selective Laser Melting*. Proceedings of the Solid Freeform Fabrication Symposium, 2013.
35. Körner, C., Attar, E., and Heintl, P., *Mesosopic simulation of selective beam melting processes*. Journal of Materials Processing Technology, 2011. **211**(6): p. 978-987.
36. Markl, M., Ammer, R., Ljungblad, U., Rüde, U., and Körner, C., *Electron Beam Absorption Algorithms for Electron Beam Melting Processes Simulated by a Three-Dimensional Thermal Free Surface Lattice Boltzmann Method in a Distributed and Parallel Environment*. Procedia Computer Science, 2013. **18**(0): p. 2127-2136.
37. Ippolito, R., Iuliano, L., and Gatto, A., *Benchmarking of Rapid Prototyping Techniques in Terms of Dimensional Accuracy and Surface Finish*. CIRP Annals - Manufacturing Technology, 1995. **44**(1): p. 157-160.
38. Reeves, P.E. and Cobb, R.C., *Reducing the surface deviation of stereolithography using in-process techniques*. Rapid Prototyping Journal, 1997. **3**(1): p. 20-31.
39. Ahn, D., Kweon, J.-H., Kwon, S., Song, J., and Lee, S., *Representation of surface roughness in fused deposition modeling*. Journal of Materials Processing Technology, 2009. **209**(15): p. 5593-5600.
40. Gajdoš, I. and Slota, J., *Influence of printing conditions on structure in FDM prototypes*. Tehnički vjesnik-Technical Gazette, 2013. **20**(2).
41. Karamooz Ravari, M.R., Kadkhodaei, M., Badrossamay, M., and Rezaei, R., *Numerical investigation on mechanical properties of cellular lattice structures fabricated by fused deposition modeling*. International Journal of Mechanical Sciences, 2014. **88**: p. 154-161.
42. Cansizoglu, O., Harrysson, O., Cormier, D., West, H., and Mahale, T., *Properties of Ti-6Al-4V non-stochastic lattice structures fabricated via electron beam melting*. Materials Science and Engineering: A, 2008. **492**(1-2): p. 468-474.
43. Harrysson, O.L.A., Cansizoglu, O., Marcellin-Little, D.J., Cormier, D.R., and West II, H.A., *Direct metal fabrication of titanium implants with tailored materials and mechanical properties using electron beam melting technology*. Materials Science and Engineering: C, 2008. **28**(3): p. 366-373.
44. Yang, L., Harrysson, O., West, H., and Cormier, D., *Compressive properties of Ti-6Al-4V auxetic mesh structures made by electron beam melting*. Acta Materialia, 2012. **60**(8): p. 3370-3379.
45. Suard, M., Martin, G., Lhuissier, P., Dendievel, R., Vignat, F., Blandin, J.J., and Villeneuve, F., *Mechanical equivalent diameter of single struts for the stiffness prediction of lattice structures produced by Electron Beam Melting*. Additive Manufacturing, 2015. **8**: p. 124-131.

46. Mandil, G., Le, V.T., Paris, H., and Suard, M., *Building new entities from existing titanium part by electron beam melting: microstructures and mechanical properties*. The International Journal of Advanced Manufacturing Technology, 2016. **85**(5): p. 1835-1846.
47. Ravari, M.R.K., Esfahani, S.N., Andani, M.T., Kadkhodaei, M., Ghaei, A., Karaca, H., and Elahinia, M., *On the effects of geometry, defects, and material asymmetry on the mechanical response of shape memory alloy cellular lattice structures*. Smart Materials and Structures, 2016. **25**(2): p. 025008.
48. Cahill, S., Lohfeld, S., and McHugh, P.E., *Finite element predictions compared to experimental results for the effective modulus of bone tissue engineering scaffolds fabricated by selective laser sintering*. J Mater Sci Mater Med, 2009. **20**(6): p. 1255-62.
49. Luxner, M.H., Stampfl, J., and Pettermann, H.E., *Nonlinear simulations on the interaction of disorder and defects in open cell structures*. Computational Materials Science, 2009. **47**(2): p. 418-428.
50. Babaei, S., Jahromi, B.H., Ajdari, A., Nayeb-Hashemi, H., and Vaziri, A., *Mechanical properties of open-cell rhombic dodecahedron cellular structures*. Acta Materialia, 2012. **60**(6-7): p. 2873-2885.
51. Campoli, G., Borleffs, M.S., Amin Yavari, S., Wauthle, R., Weinans, H., and Zadpoor, A.A., *Mechanical properties of open-cell metallic biomaterials manufactured using additive manufacturing*. Materials & Design, 2013. **49**(0): p. 957-965.
52. Monforton, G. and Wu, T.S., *Matrix analysis of semi-rigidly connected frames*. Journal of the structural Division, ASCE, 1963. **89**(ST6): p. 13-42.
53. Simões, L.M.C., *Optimization of frames with semi-rigid connections*. Computers & Structures, 1996. **60**(4): p. 531-539.
54. Sekulovic, M. and Salatic, R., *Nonlinear analysis of frames with flexible connections*. Computers & Structures, 2001. **79**(11): p. 1097-1107.
55. Hassani, B. and Hinton, E., *A review of homogenization and topology optimization I—homogenization theory for media with periodic structure*. Computers & Structures, 1998. **69**(6): p. 707-717.
56. Hassani, B. and Hinton, E., *A review of homogenization and topology optimization II—analytical and numerical solution of homogenization equations*. Computers & Structures, 1998. **69**(6): p. 719-738.
57. Gibson, L.J. and Ashby, M.F., *The Mechanics of Three-Dimensional Cellular Materials*. Proceedings of the Royal Society of London. A. Mathematical and Physical Sciences, 1982. **382**(1782): p. 43-59.
58. Ashby, M., *Hybrid Materials to Expand the Boundaries of Material-Property Space*. Journal of the American Ceramic Society, 2011. **94**(s1): p. s3-s14.
59. Deshpande, V.S., Ashby, M.F., and Fleck, N.A., *Foam topology: bending versus stretching dominated architectures*. Acta Materialia, 2001. **49**(6): p. 1035-1040.
60. Doyoyo, M. and Hu, J.W., *Multi-axial failure of metallic strut-lattice materials composed of short and slender struts*. International Journal of Solids and Structures, 2006. **43**(20): p. 6115-6139.

61. Hu, J.W. and Park, T., *Continuum Models for the Plastic Deformation of Octet-Truss Lattice Materials Under Multiaxial Loading*. Journal of Engineering Materials and Technology, 2013. **135**(2): p. 021004-1~11.
62. Tollenaere, H. and Caillerie, D., *Continuous modeling of lattice structures by homogenization*. Advances in Engineering Software, 1998. **29**(7–9): p. 699-705.
63. Caillerie, D., Mourad, A., and Raoult, A., *Discrete Homogenization in Graphene Sheet Modeling*. Journal of Elasticity, 2006. **84**(1): p. 33-68.
64. Dos Reis, F. and Ganghoffer, J., *Discrete homogenization of architected materials: Implementation of the method in a simulation tool for the systematic prediction of their effective elastic properties*. Technische Mechanik, 2010. **30**: p. 85-109.
65. Kalamkarov, A.L., Hassan, E.M., Georgiades, A.V., and Savi, M.A., *Asymptotic homogenization model for 3D grid-reinforced composite structures with generally orthotropic reinforcements*. Composite Structures, 2009. **89**(2): p. 186-196.
66. Hassan, E.M., Georgiades, A.V., Savi, M.A., and Kalamkarov, A.L., *Analytical and numerical analysis of 3D grid-reinforced orthotropic composite structures*. International Journal of Engineering Science, 2011. **49**(7): p. 589-605.
67. Kumar, R.S. and McDowell, D.L., *Generalized continuum modeling of 2-D periodic cellular solids*. International Journal of Solids and Structures, 2004. **41**(26): p. 7399-7422.
68. Kumar, R.S. and McDowell, D.L., *Multifunctional design of two-dimensional cellular materials with tailored mesostructure*. International Journal of Solids and Structures, 2009. **46**(14–15): p. 2871-2885.
69. Dos Reis, F. and Ganghoffer, J.F., *Construction of micropolar continua from the asymptotic homogenization of beam lattices*. Computers & Structures, 2012. **112–113**(0): p. 354-363.
70. Kim, H.S. and Al-Hassani, S.T.S., *Effective elastic constants of two-dimensional cellular materials with deep and thick cell walls*. International Journal of Mechanical Sciences, 2003. **45**(12): p. 1999-2016.
71. Luxner, M.H., Stampfl, J., and Pettermann, H.E., *Numerical simulations of 3D open cell structures – influence of structural irregularities on elasto-plasticity and deformation localization*. International Journal of Solids and Structures, 2007. **44**(9): p. 2990-3003.
72. Arabnejad, S. and Pasini, D., *Mechanical properties of lattice materials via asymptotic homogenization and comparison with alternative homogenization methods*. International Journal of Mechanical Sciences, 2013. **77**(0): p. 249-262.
73. Cerardi, A., Caneri, M., Meneghello, R., Concheri, G., and Ricotta, M., *Mechanical characterization of polyamide cellular structures fabricated using selective laser sintering technologies*. Materials & Design, 2013. **46**(0): p. 910-915.
74. Vigliotti, A. and Pasini, D., *Stiffness and strength of tridimensional periodic lattices*. Computer Methods in Applied Mechanics and Engineering, 2012. **229**: p. 27-43.
75. Vigliotti, A. and Pasini, D., *Linear multiscale analysis and finite element validation of stretching and bending dominated lattice materials*. Mechanics of Materials, 2012. **46**(0): p. 57-68.

76. Vigliotti, A., Deshpande, V.S., and Pasini, D., *Non linear constitutive models for lattice materials*. Journal of the Mechanics and Physics of Solids, 2014. **64**(0): p. 44-60.
77. Chang, D.-Y. and Huang, B.-H., *Studies on profile error and extruding aperture for the RP parts using the fused deposition modeling process*. The International Journal of Advanced Manufacturing Technology, 2011. **53**(9): p. 1027-1037.
78. Lennart, B., Cindy, B., Moneer, H., Robert, T., Konrad, W., and David, D., *Understanding error generation in fused deposition modeling*. Surface Topography: Metrology and Properties, 2015. **3**(1): p. 014002.
79. Meakin, P. and Jullien, R., *Restructuring effects in the rain model for random deposition*. Journal de Physique, 1987. **48**(10): p. 1651-1662.
80. Boley, C.D., Khairallah, S.A., and Rubenchik, A.M., *Calculation of laser absorption by metal powders in additive manufacturing*. Applied Optics, 2015. **54**(9): p. 2477-2482.
81. Roberts, I.A., Wang, C.J., Esterlein, R., Stanford, M., and Mynors, D.J., *A three-dimensional finite element analysis of the temperature field during laser melting of metal powders in additive layer manufacturing*. International Journal of Machine Tools and Manufacture, 2009. **49**(12–13): p. 916-923.
82. Zeng, K., Pal, D., Gong, H.J., Patil, N., and Stucker, B., *Comparison of 3DSIM thermal modelling of selective laser melting using new dynamic meshing method to ANSYS*. Materials Science and Technology, 2015. **31**(8): p. 945-956.
83. Taylor, C.M., *Direct laser sintering of stainless steel: thermal experiments and numerical modelling*. 2004, The University of Leeds.
84. Spierings, A.B., Schneider, M., and Eggenberger, R., *Comparison of density measurement techniques for additive manufactured metallic parts*. Rapid Prototyping Journal, 2011. **17**(5): p. 380-386.
85. Yang, L., Harrysson, O., Cormier, D., West, H., Gong, H., and Stucker, B., *Additive Manufacturing of Metal Cellular Structures: Design and Fabrication*. JOM, 2015. **67**(3): p. 608-615.
86. El-Gizawy, A.S., Corl, S., and Graybill, B. *Process-induced Properties of FDM Products*. in *Proceedings of the ICMET, International Conference on Mechanical Engineerings and Technology Congress & Exposition*. 2011.
87. Thomas, J. and Rodríguez, J. *Modeling the fracture strength between fused deposition extruded roads*. in *Proceedings of the 11th Solid Freeform Fabrication Symposium*. 2000.
88. Marques Filho, S.J.P.J. and Horowitz, B., *Flexibility modeling of reinforced concrete concentric frame joints*. Revista IBRACON de Estruturas e Materiais, 2013. **6**: p. 360-374.
89. Frye, M.J. and Morris, G.A., *Analysis of Flexibly Connected Steel Frames*. Canadian Journal of Civil Engineering, 1975. **2**(3): p. 280-291.
90. Sekulovic, M., Salatic, R., and Nefovska, M., *Dynamic analysis of steel frames with flexible connections*. Computers & Structures, 2002. **80**(11): p. 935-955.
91. Kartal, M., Basaga, H., Bayraktar, A., and Muvafik, M., *Effects of semi-rigid connection on structural responses*. Electronic journal of structural Engineering, 2010. **10**(10): p. 22-35.

92. Ma, Z.-D., Kikuchi, N., Pierre, C., and Raju, B., *Multidomain Topology Optimization for Structural and Material Designs*. Journal of Applied Mechanics, 2005. **73**(4): p. 565-573.
93. Penrose, R. *On best approximate solutions of linear matrix equations*. in *Mathematical Proceedings of the Cambridge Philosophical Society*. 1956. Cambridge Univ Press.
94. Hassani, B. and Hinton, E., *Homogenization and structural topology optimization: theory, practice and software*. 2012: Springer Science & Business Media.
95. Bazoune, A., Khulief, Y.A., and Stephen, N.G., *SHAPE FUNCTIONS OF THREE-DIMENSIONAL TIMOSHENKO BEAM ELEMENT*. Journal of Sound and Vibration, 2003. **259**(2): p. 473-480.

VITA

Sang-in Park

SANG-IN PARK was born in Seoul, South Korea. He received a B.A. in Mechanical Engineering from Hanyang University in 2006 and a M.S. degree in Automotive Engineering from Hanyang University in 2008 before coming to Georgia Tech to pursue a doctorate in Mechanical Engineering. He received a Ph.D. degree in Mechanical Engineering from the Georgia Institute of Technology, Atlanta, United States in 2016. His main areas of research interest are cellular material design and manufacturing, additive manufacturing, structural design optimization, and computer aided engineering.

Estimating Mechanical Properties of Cellular Solid Materials
from Additive Manufacturing Processes

Sang-in Park

220 pages

Directed by Dr. David W. Rosen

Cellular materials have been used for engineering applications due to their favorable mechanical characteristics. However, conventional subtractive manufacturing processes are not suitable for cellular materials because of their complex geometries. Recently, additive manufacturing (AM) processes have begun to offer new opportunities to produce cellular materials. Layer-by-layer stacking process allows users to fabricate complex geometries with no additional effort. Although the AM technique can be a good solution for manufacturing issues, the mechanical properties of additively fabricated cellular materials cannot be guaranteed due to the inherent limitations of the AM process. This research aims to develop a mechanical property-estimation procedure for additively manufactured cellular materials by considering the effects of AM processes. In order to clearly understand the AM process, related parameters are categorized into four groups: (a) Design and Manufacturing process parameters (DMP), (b) Layer deposition parameters (LDP), (c) Structural element parameters (SEP), and (d) Cellular material properties (CMP). Three transformations are defined among these groups. Firstly, the functional relationship between DMPs and LDPs is established based on process-modeling simulation. The variation in LDPs due to manufacturing instabilities is quantified in the form of a stochastic distribution. Next, an as-fabricated voxel modeling approach is developed for describing the propagation of geometrical degradation from LDPs to SEPs. The effective values of SEPs are determined based on semi-rigid joint

frame element formulation. Finally, a discrete homogenization approach is implemented with the semi-rigid elements to integrate the effects of AM processes into the mechanical property estimation procedure. The estimation framework developed in this research can be applied to analyze the performance of additively manufactured cellular materials and help to design of cellular materials.